

Henrik Skogen

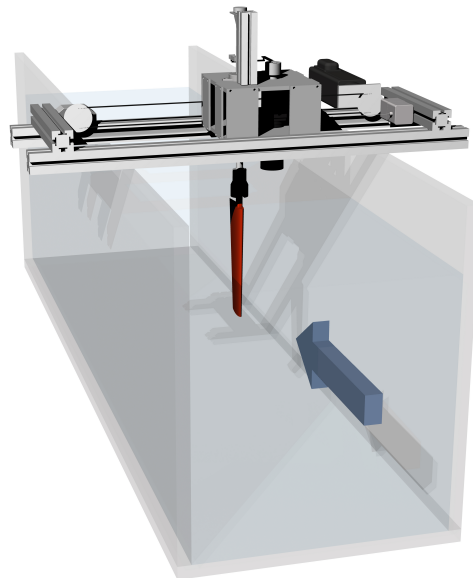
Master Thesis in Marin Technology

Design and testing of hydroelastic lifting surfaces in static and dynamic conditions

Master's thesis in Marin Technology

Supervisor: Luca Savio

June 2019



Henrik Skogen

Master Thesis in Marin Technology

Design and testing of hydroelastic lifting surfaces in static and dynamic conditions

Master's thesis in Marin Technology
Supervisor: Luca Savio
June 2019

Norwegian University of Science and Technology
Faculty of Natural Sciences
Department of Marine Technology



NTNU Trondheim
Norwegian University of Science and Technology
Department of Marine Technology

MASTER THESIS IN MARINE TECHNOLOGY

FOR

Henrik Skogen

Design and testing of hydroelastic lifting surfaces in static and dynamic conditions

The standard design of marine lifting surfaces is carried out with assumption that the structure does not deform under the action of the forces that the fluid exerts on the body; the structures of propeller blades, rudders and stabilizing fins are stiff enough that the deformations under hydrodynamic loads can be neglected. Furthermore, compared to aerodynamic wings, marine lifting surfaces have typically low aspect ratios and viscous damping in water is higher than in air, leading to fact that flutter is almost never a problem in naval architecture. For the above-mentioned reasons, hydroelasticity has always been a niche topic in naval architecture, although several attempts have been carried throughout the years to turn the hydro-elastic response of flexible structure to an advantage; these attempts had mixed results in terms of being successful. One reason for the mixed fortune of such design has been identified in the lack of good validation material, in the form of experimental data, to compare the prediction of the codes used for the design.

Flapping foils are often presented as an alternative to conventional propellers for ship propulsion. Compared to propeller blades, flapping foils have larger aspect ratios making them slenderer and hence suitable for hydroelastic tailoring. In this thesis the candidate shall develop a procedure for designing flexible foils to be produced by 3D printing. The foils shall achieve a set goal, in terms for example of bend-twist coupling. The foils shall be produced and tested to verify the presence of hydroelastic effects. The experimental campaign shall be planned by the candidate, as well as the execution of the tests, which are to be reported in the master thesis.

In the thesis the candidate shall present his personal contribution to the resolution of problem within the scope of the thesis work.

Theories and conclusions should be based on mathematical derivations and/or logic reasoning identifying the various steps in the deduction.

The candidate should utilize the existing possibilities for obtaining relevant literature, and is recommended to use the library actively.

The thesis should be organized in a rational manner to give a clear exposition of results, assessments, and conclusions. The text should be brief and to the point, with a clear language. Telegraphic language should be avoided.

The thesis shall contain the following elements: A text defining the scope, preface, list of contents, summary, main body of thesis, conclusions with recommendations for further work, list of symbols and acronyms, reference and (optional) appendices. All figures, tables and equations shall be numerated.

The original contribution of the candidate and material taken from other sources shall be clearly defined. Work from other sources shall be properly referenced using an acknowledged referencing system.



NTNU Trondheim
Norwegian University of Science and Technology
Department of Marine Technology

The thesis shall be submitted electronically in PDF. Appendices in other electronic formats can be submitted in a zip-file. The thesis shall be signed by the candidate, and it shall include this text signed by the main supervisor in facsimile.

Supervisor : Prof. Luca Savio
Co-supervisor : Prof. Sverre Steen
Deadline : 01.07.2019

Luca Savio

Abstract

A background study showed that oscillating hydrofoils has some promising results concerning thrust generation and propulsion efficiency, compared to traditional propellers. The dynamic stall has an important role in the thrust and lift generated by the oscillating hydrofoil. Aircraft wings are designed to twist to a lower angle of attack (AoA) when the lift on the wing increase, to ensure no stall on the wing. In this thesis, a NACA0012 hydrofoil with 15cm chord was designed and printed. The design aimed to make it twist to a lower AoA for higher loads. The design was printed with Stratasys 3D-printer at SINTEF Ocean. The results were compared with a reference foil with stiffer material properties.

The experiments were conducted in the circulating water tunnel (CWT) at the Norwegian University of Science and Technology (NTNU). Test on two hydrofoils oscillating in sway and yaw with harmonic sinus motion was conducted at four flow condition ($Re = 22500, 37500, 45000, 52500$).

Previous experiments by L. Bösch (2017) and Read (2003) was repeated. An agreement was found for a maximum angle of attack (α_{max}) of 22.5° .

The propulsion efficiency showed a tendency towards $\phi = 75^\circ$, phase angle between sway and yaw. Bösch concluded the same tendency in 2017. For several α_{max} the flexible hydrofoil has higher efficiency, than the stiff foil ($\eta_p \approx 50\%$). Regarding the thrust generation the flexible hydrofoil with $\phi = 90^\circ$ showed a somewhat higher C_T for $St = 0.20 - 0.40$.

η_p	<i>Stiff</i>		<i>Flexible</i>	
	$\varphi = 90$	$\varphi = 75$	$\varphi = 90$	$\varphi = 75$
15	0.4351	0.3644	0.4882	0.4484
22.5	0.4823	0.5035	0.5254	0.5610
30	0.4848	0.5064	0.5143	0.5452
41	0.4628	0.4429	0.4949	0.5173
44	0.4276	0.4901	0.4674	0.4976

(a)

C_T	<i>Stiff</i>		<i>Flexible</i>	
	$\varphi = 90$	$\varphi = 75$	$\varphi = 90$	$\varphi = 75$
15	0.0836	0.0490	0.0884	0.0585
22.5	0.3943	0.2861	0.4284	0.3068
30	0.6345	0.4995	0.6551	0.5265
41	0.9345	0.9168	0.9464	0.9724
44	0.9120	0.7245	0.9123	0.7399

(b)

Sammendrag

En bakgrunnsundersøkelse viste at oscillerende hydrofoiler har noen lovende resultater med tanke på thrust og propulsjonsvirkningsgrad, sammenlignet med tradisjonelle propellere. Dynamisk stall spiller en viktig rolle i kraften som genereres av en oscillerende hydrofoil. Flyvinger er utformet for å vri/twiste vingen til en lavere angrepsvinkel (AoA) når løftet på vingen øker. I designfasen av denne avhandlingen ble det gjort en innsats for å designe en NACA0012 hydrofoil, med 15cm kordelengde, for å få den til å twiste til lavere AoA for økt generert kraft. Designet ble skrevet ut med Stratasys 3D-skriver på SINTEF Ocean. Resultatene ble sammenlignet med en referansefoil med stivere materialegenskaper.

Forsøkene ble utført i en sirkulasjonstank (CWT) ved Norges teknisk-naturvitenskapelige universitet (NTNU). Tester på to hydrofoils som oscillerer sideveis og i rotasjon med harmonisk sinusbevegelse ble utført ved fire strømningsforhold ($Re = 22500, 37500, 45000, 52500$).

Tidligere eksperimenter av L. Bösch (2017) og Read (2003) ble repetert. Samsvar ble funnet for en maksimal angrepsvinkel (α_{max}) på $22,5^\circ$.

Propulsjonsvirkningsgraden viste en tendens til en fase mellom sideveis- og rotasjonsbevegelsen mot $\phi = 75^\circ$. Den samme tendensen konkludert Bösch med i 2017. For de fleste α_{max} hadde den fleksible hydrofoilen høyere propulsjonsvirkningsgraden ($\eta_p \approx 50\%$). Den fleksible hydrofoil med $\phi = 90^\circ$ viste seg å generer noe høyere thrust (C_T) for $St = 0.20 - 0.40$.

η_p	<i>Stiff</i>		<i>Flexible</i>	
	$\phi = 90$	$\phi = 75$	$\phi = 90$	$\phi = 75$
15	0.4351	0.3644	0.4882	0.4484
22.5	0.4823	0.5035	0.5254	0.5610
30	0.4848	0.5064	0.5143	0.5452
41	0.4628	0.4429	0.4949	0.5173
44	0.4276	0.4901	0.4674	0.4976

(c)

C_T	<i>Stiff</i>		<i>Flexible</i>	
	$\phi = 90$	$\phi = 75$	$\phi = 90$	$\phi = 75$
15	0.0836	0.0490	0.0884	0.0585
22.5	0.3943	0.2861	0.4284	0.3068
30	0.6345	0.4995	0.6551	0.5265
41	0.9345	0.9168	0.9464	0.9724
44	0.9120	0.7245	0.9123	0.7399

(d)

Preface

This thesis is written as a part of the 5-year study program, Marin Technology at the Norwegian University for Science and Technology (NTNU). The experiment was conducted in the circulating water tunnel (CWT) at Tyholt in Trondheim. The design of the foils was done in AUTODESK's CAD software, Inventor. SINTEF Ocean did 3D-printing of the flexible foils.

Several months were used in the design phase of the flexible foils. It was crucial that some deformation, preferable twist deformation along the span, was noticed. It was also the aim of the design phase to make the foils strong enough to withstand the hydrodynamics loads, regarding the flexible characteristics.

List of figures and tables is not included, as requested by the supervisor.

Several people from NTNU and SINTEF Ocean contributed to making this thesis possible. I want to thank Torgeir Wahl for setting up the experiment and guidance through the experiment. Gratitude also goes to Nils Arne Snekvik for help with the design and printing of the foils. Also, the help from Kristian Minde was crucial during the design of the foils and to integrate the foils in the already existing setup.

I want to thank the boys at the office for backup and support during the writing. It would not have been the same without social collaboration in the office.

For the weekly discussion and constructive feedback during the work on this thesis, I would like to thank my supervisor Luca Savio. He showed a lot of interest in my thesis and was always available for questions. He was also involved in the experiment.

Contents

1 Introduction	1
1.1 Background and Motivation	1
1.2 Turbulence Level and Stimulation	2
1.3 Circulating Water Tunnel and Separation Bubbles	3
1.4 Motion	4
1.5 Range of Strouhal Number	8
1.6 Objective	8
1.7 Outline	9
2 Theory	10
2.1 Average	10
2.2 Standard Deviation	10
2.3 Finite Difference	11
2.4 Non-Dimensional Units	11
2.5 Finite Element Method	15
2.6 Shear Stress	15
2.7 Shear Centre	16
2.8 Centre of Pressure	18
2.9 Angle of Attack	20
2.10 Twist Angle	22
2.11 Foil Theory	24
2.12 Force and Force Coefficients	24
2.12.1 Thrust and Power	24
2.12.2 Propulsion Efficient	26
2.12.3 Lift	26
2.12.4 Moment	27
2.13 Post Processing	28
2.13.1 Filter Noise	28
3 Experimental Setup	34
3.1 Circulation Water Tunnel	34

3.2	Equipment	35
3.3	Camera Setup	39
3.4	Measurement	43
3.4.1	Laser Doppler Velocimetry	43
3.4.2	Force Measurement	44
4	Design of Hydrofoils in Inventor	48
4.1	Mesh in Inventor	49
4.2	Design Process	51
4.2.1	Theoretical Lift on the foil	51
4.3	Initial Design	52
4.4	Second Design	53
4.5	Final Design	55
4.5.1	Finding Shear Centre of the Design	56
4.5.2	Finding Centre of Pressure	57
4.5.3	Definition of the Final Design	58
4.6	Printing	59
5	Initial Testing	66
5.1	Calibration of Equipment	66
5.2	Angle of Attack Range	67
5.2.1	Overload	68
5.3	Decay Test	68
5.3.1	Decay of stiff foil submerged in water	69
5.3.2	Decay of stiff foil in air	70
5.3.3	Decay of flexible foil submerged in water	71
5.3.4	Decay of flexible foil in air	72
5.3.5	Results of Decay Tests	74
5.4	Boundary Layer	75
5.5	Frequency Range	76
5.6	Bias errors	78
6	Results and Discussion	81

6.1	Static Lift, Drag and Moment	83
6.2	Repetition of Read's experiments	86
6.3	Result of the stiff and flexible foil	88
6.3.1	Thrust coefficient	88
6.3.2	Power Coefficient	90
6.3.3	Propulsion Efficiency	93
6.3.4	Local and Global Maximum	96
6.3.5	Lift Coefficient versus Propulsion Efficiency	100
6.3.6	Power, Thrust and Lift During One Oscillation	103
7	Conclusion	107
7.1	Recommendation for further work	108
	Appendices	II
A	Graphs with C_T, C_P, η_p, and Static Lift and Drag	II
A.1	C_T vs η_p	II
A.2	Static Lift and Drag	VI
A.3	Forces During One Oscillation	IX
A.4	C_T	XI
A.5	C_P	XVIII
A.6	η_p	XXIII
A.7	Bar plot with maximum C_T and maximum η_p	XXX
B	Stratasys and printing	XXXII
C	FASTCAM MH4 camera	XXXIV
D	MATLAB	XXXVI
D.1	Post processing of data	XXXVI
D.2	Calculate shear centre and plot	L
D.3	Plot C_p from <i>XFOil</i>	LIII

Abbreviations

AoA	=	Angle of Attack
AES	=	Average Element Size
BL	=	Boundary Layer
FDM	=	Finite Difference Method
FEA	=	Finite Element Analyze
FEM	=	Finite Element Method
GF	=	Grading Factor
LSB	=	Laminar Separation Bubbles
MES	=	Minimum Element Size
MTA	=	Minimum Turn Angle
PSD	=	Power Spectral Density

List of symbols

Name	Symbol
Fresh Water Density	ρ
Kinematic viscosity	ν
Velocity free stream	U_{inf}
Chord length	c
Span length	s
Camber	z
Angle of attack (AoA)	α
Induced angle of attack	β
Yaw angle of foil	θ
Yaw amplitude	θ_{yaw}
Sway motion	y_{sway}
Sway Amplitude	y_{sway}^{amp}
Phase	ϕ
Reynolds number	Re
Chord Reynolds number	Re_c
Froude number	F_n
Advance number	J_A
Strouhal number	St
Feathering parameter	χ
Bending moment shaft	M_z
Inline force	F_x
Cross flow force	F_y
Lift	L
Thrust	T
Drag	D
Power	P
Lift coefficient	C_L
Thrust coefficient	C_T
Drag coefficient	C_D
Power coefficient	C_P
Resultant Coefficient	C_R

Name	Symbol
Frequency	f
Natural Frequency	f_n
Frequency of motion	f_m
Propulsion efficiency	η_P
Length of beam	l
Bending moment beam	M
Uniformly distributed load	P
Young's modulus	E
Second area of inertia	I
Twist angle	Θ
Deflection	ϵ
Centre of pressure	c_p
Transition temperature	T_g
Relative distance between cameras	d
Orientation of camera i	φ_i

1 Introduction

In this section the background and motivation for oscillating hydrofoils is presented, and the scope of this thesis is defined. Literature review done in the fall in the project thesis are summarized.

This thesis is written in the spring 2019. With supervision from Luca Savio and SINTEF Ocean with the aim to test three oscillating NACA0012 foils with different material properties. The experiment is conducted in the circulating water tunnel (CWT). The experimental setup for the foil rig is all ready made by John Martin Kleven Godø [18] and was also used by Lennard Bösch on his master thesis in 2017 [7].

1.1 Background and Motivation

Aquatic animals are using a flapping mechanism to create thrust. 90% of the thrust is generated by the lift on the caudal fin, making it comparable to one oscillating hydrofoil [32]. Aquatic animals have been developed during millions of year of evolution to obtain a high propulsion efficiency. High propulsion efficient indicate low energy used to create high thrust. The high efficient for aquatic animals are developed for Strouhal number typical $0.20 < St < 0.40$ [35]. It will be advantageous to use the same range in this thesis. To see if the same efficiency can be obtain with the same mechanism and motion on a hydrofoil. Aquatic animals have a somewhat flexible fin to generate the thrust, not hard and stiff like the propellers build today.

For centuries the propeller and thrusters have been made of a hard materials with high stiffness and small local deformation due to pressure and lift forces on the propel. A propeller consist of blades, normally 2-5, attached to the propeller boss. When the propeller boss rotates the blades are rotated and this creates thrust. The thrust is created due to the lift force on each blade. If the blades is made of flexible material it will start to deform due to the hydrodynamic loads. The motivation for building flexible blades is the same as the motivation for building flexible wings to aircraft's: when the lift on the wing gets to high due to a high induced angle of attack, the wing

will start to deform at leading edge so that the induced angle of attack is reduced [8]. This can also be obtained for hydrofoils. To obtain this effect a study of the cross section and the pressure distribution on the wing needs to be investigated. If the shear centre of the cross section of the wing is closer to leading edge than the centre of pressure, the wing will start to twist, and the induced angle of attack is reduced. For the opposite case, when the centre of pressure is closer to leading edge than the shear centre the foil will twist to a higher angle of attack.

Stabilizing fins and other stabilization mechanism's is crucial to sail the hydrofoil-ship safely. If the hydrofoil that lift the ships out of the water have a self-stabilization mechanism this will make the sailing more safe and comfortable. This self-stabilization mechanism can be obtained in the same way as for the wings on the aircraft's. The mean shear centre of the cross section of the lifting hydrofoil needs to be closer to the leading edge of the hydrofoil than the centre of pressure. This has been the motivation of this master thesis, to design a flexible hydrofoil that will twist to a smaller angle of attack when the induced angle of attack gets to large.

Luca Savio investigated deflection on a propeller with increasing load in 2015. Some observation done by Savio, for a flexible propeller with inflow velocity V_A , the tip was bending backwards when the loads is close to zero, the bending was still present for higher loads. When the load was large the blade twisted so that the pitch increased from the root to the tip. The deflection was larger for higher loads, especially near the tip for the blade [31].

1.2 Turbulence Level and Stimulation

The turbulence level in the test section was measured with Laser Doppler Velocimetry (LDV) by Lennard Bösch in 2017 for the same test section. He found that the turbulence level was less than 1 % in the test section [7]. Due to time limitation in CWT the re-measurement was not conducted assuming that same turbulence level is achieved.

The low turbulence level is obtained due to series of upstream mesh grids that create close to laminar flow. Together with contraction ratio 6 to 1 this indicate close to laminar flow onto the foil in the test section. The flow condition in the test section is at Reynolds number of 150 000. Assuming free stream velocities of $U_{inf} = 1.0$ m/s, water temperature of 20 °C and with chord length = 0.15 m. At this condition it is not clear how the boundary layer will behave. To reduce the laminar effects a boundary tripwire can be placed close to the leading edge. The thickness and location of the tripwire is a large topic and will not be discussed deeply in this thesis.

The shape of the trip wire can vary. The two most common methods is a zig-zag trip wire (Hama-strip) and adhering granulated sand in a small strip on the foil [16]. Braslow defines the critical roughness Reynolds number as the value at which turbulent spots are initiated, and that the experimental values should be from 250 to 600 [6]. To get a fully turbulent boundary layer the critical roughness Reynolds number should be higher than 600, according to Braslow. Van Rooij claim that the critical roughness Reynolds number could be as low as 200 for a Hama-stripe [30]. But it was not clear how they obtained this low value. Böche used a Hama-strip in his master thesis spring 2017. He argued that the Hama-strip was better to use for low critical Reynolds numbers [7].

1.3 Circulating Water Tunnel and Separation Bubbles

When testing model sized propellers and hydrofoils the air pressure also needs to be scaled to get the correct condition for the operating propeller or hydrofoil. In this study the Circulating Water Tunnel (CWT) at NTNU Marinteknisk Senter at Tyholt is used. This is a partly closed system with water circulating and the test section not moving. This makes it possible to observe and test different objects. The velocities is controlled by changing the rotation frequency of a engine that drive the impeller inside the tube and accelerate the water from 0 up to maximum of 1.0 m/s. The test section is open to atmospheric pressure, due to this the pressure will not be scaled and need to be taking into account when discussing and comparing results. Due to size limitation in the test section the chord Reynolds number is low ($Re_c = 20\ 000$

- 200 000) compared to full size foils. The scaling effect is a large subject, and was not the aim of this study. Problems with low Re_c is the laminar effects on the surface of the foils: laminar separation, laminar boundary layer, laminar separation bubbles (LSB), separation without reattachment. According to Carmichael the separation bubble is a non linear phenomena that occur when the flow is laminar and separates from the foil and reattaches prior to the trailing edge. The range of witch this is important are $Re = 50\ 000 - 100\ 000$ [8]. This is the same range as in CWT. This effects will not occur in the full scale system, due to much higher Re_c . To make this study comparable to full scale a boundary layer trip is used to make a turbulent flow around the foil, trying to avoid the critical laminar effects.

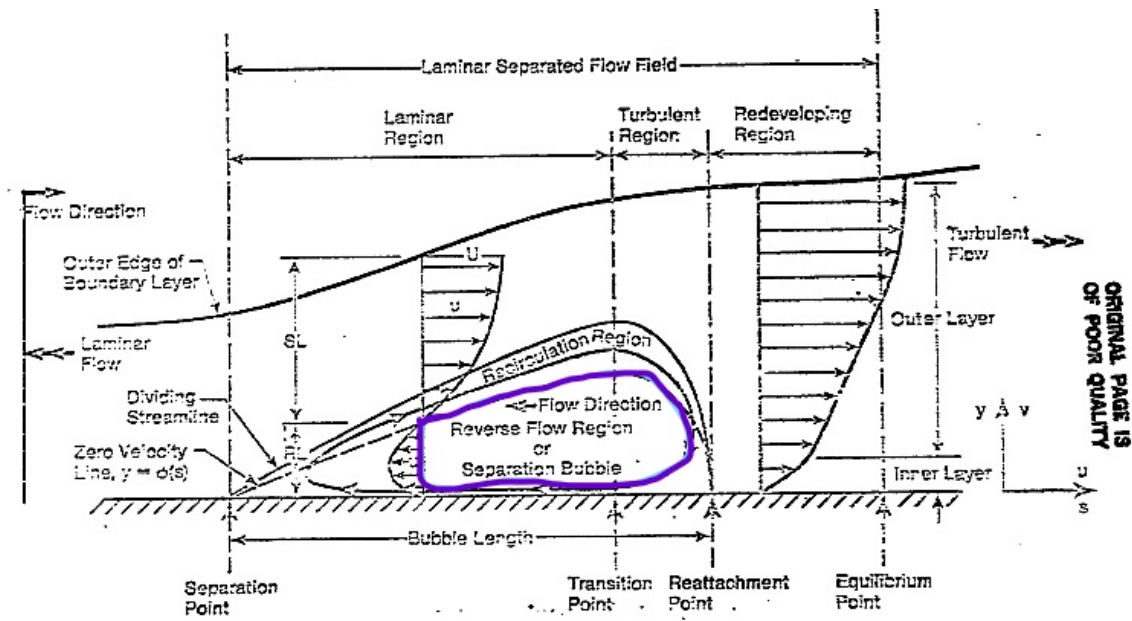


Figure 1.1: Laminar separation bubbles (purple area) due to laminar boundary layer. Modified Figure from Carmichael [8]

1.4 Motion

Earlier experiments have presented results for harmonic sinus motion in sway and yaw, with a phase delay of the yaw motion, ϕ ([3], [7], [18] and [29]). All this studies are conducted with stiff material and smaller deformation. The equation that describe

the combined harmonic motion in sway and yaw can be describe by sinus motion (Equation [1](#)). Same harmonic function which was used in earlier studies.

$$\begin{aligned} y_{sway} &= y_{sway}^{amp} \sin(\omega t) \\ \theta_{yaw} &= \theta_{yaw}^{amp} \sin(\omega t + \phi) \end{aligned} \quad (1)$$

y_{sway}^{amp} is the sway amplitude (cross flow motion), θ_{yaw}^{amp} is the yaw amplitude (rotation around z-axis), ω is the frequency of motion ($2\pi f$), y_{sway} and θ_{yaw} is the sway and yaw motion, respectively. An important parameter is the angle of attack (AoA or α). It is the angle between the chord line (centre line) of the hydrofoil and flow direction. In this thesis the flow direction is a combination of the relative motion between the hydrofoil and the water direction [\[19\]](#).

Anderson studied the harmonic sway and yaw motion at various phases. According to Anderson $\phi = 75^\circ - 90^\circ$ was noticed as the range with highest efficient. Highest propulsion efficient, η_p , was obtained at large amplitude of motion, large angle of attack ($\alpha_{max} = 15^\circ - 25^\circ$) and $\phi = 75^\circ$ [\[3\]](#). Bösch studied "What kind of motions are preferred, and are there any trends?". He noticed two peaks in η_p , $\phi = 75^\circ$ and $\phi = 90^\circ$ (Figure [1.2](#)). Tendency towards $\phi = 75^\circ$ for the highest efficiency. He also comment that η_p is very sensitive to small changes of ϕ . By changing from $\phi = 76.5^\circ$ to $\phi = 80.6^\circ$, η_p changed from 72% to 57% [\[7\]](#).

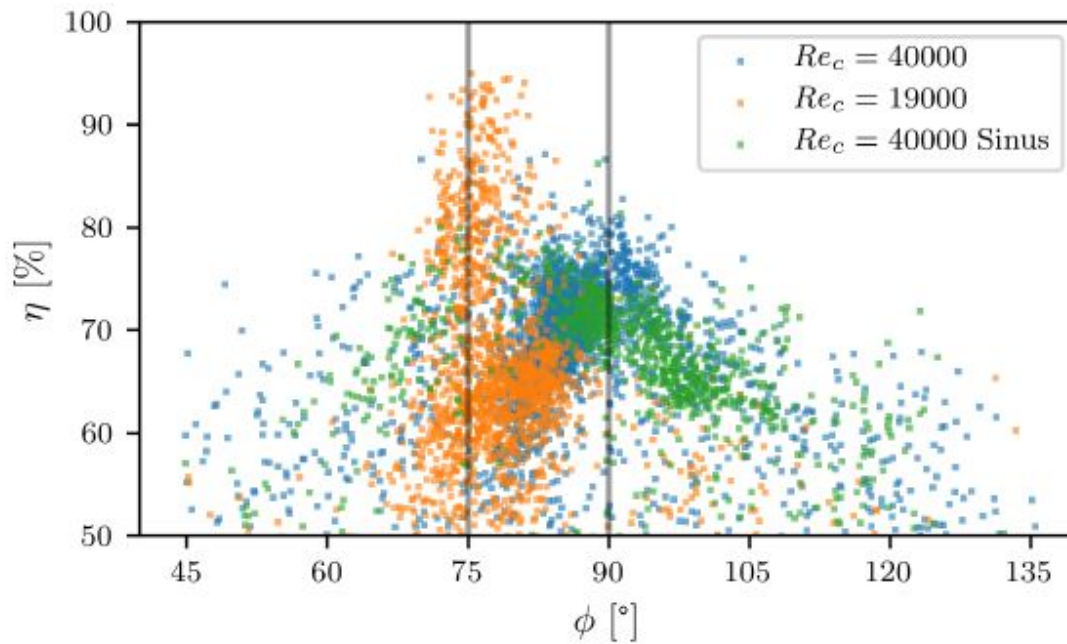


Figure 1.2: Efficiency η_p vs phase ϕ . Courtesy to Lennard Bösch [7]

Bösch argued that the drop in efficiency might be due to how the thrust and power consumption during one oscillation was changed. The biggest change with regard to the phase is when AoA crosses zero. For $\phi = 80.6^\circ$ the foil is creating negative thrust when AoA crosses zero, which could explain a reduction in η_p compared to $\phi = 76.4^\circ$ (Figure 1.3 and 1.4).

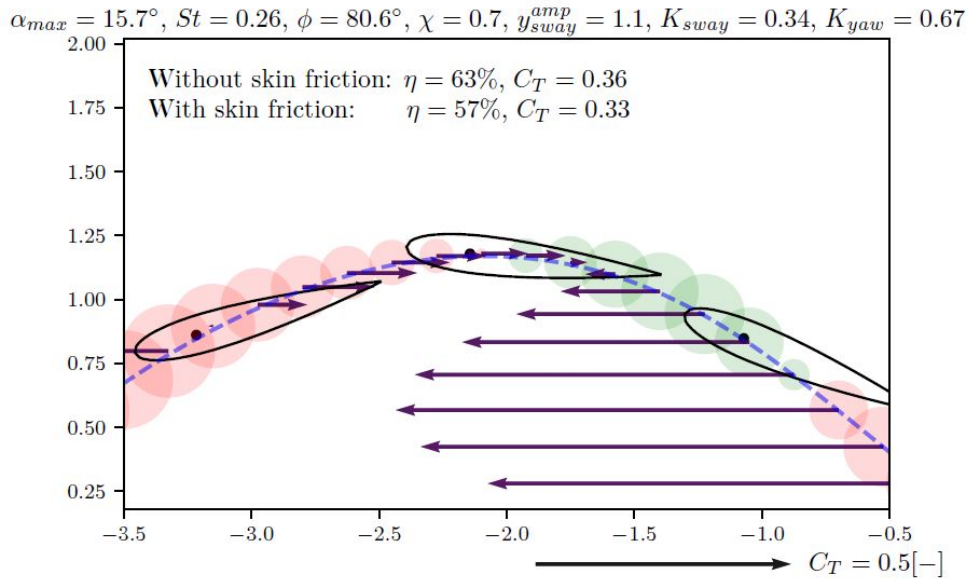


Figure 1.3: Thrust and power consumption when AoA crosses zero. $\phi = 80.6^\circ$.
 Courtesy to Lennard Bösch [7]

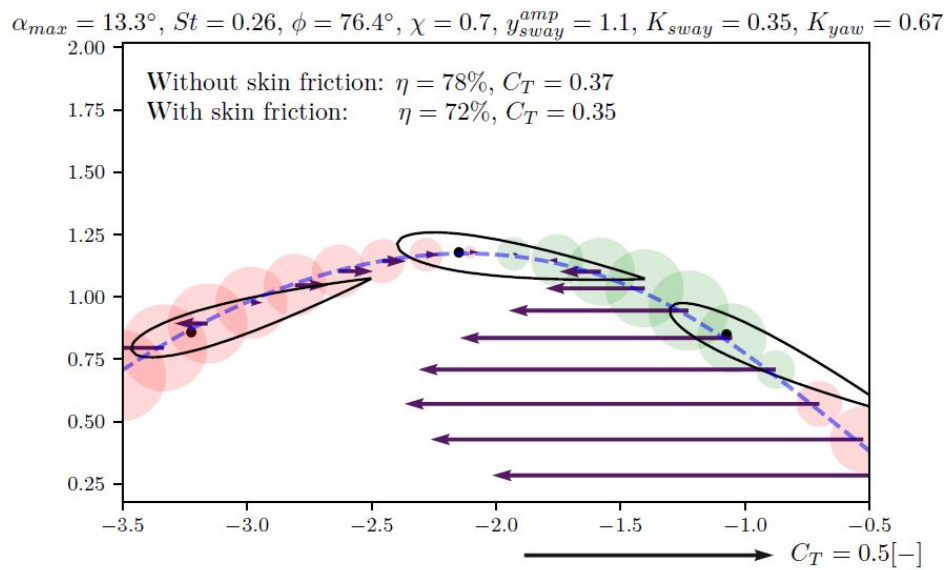


Figure 1.4: Thrust and power consumption when AoA crosses zero. $\phi = 76.5^\circ$.
 Courtesy to Lennard Bösch [7]

1.5 Range of Strouhal Number

The harmonic sinus motion in sway and yaw will produce a wake with Von Karman Street. For some range of Strouhal number the wake will be a reverse Von Karman Street. The reverse Von Karman street will create thrust on the foil, in the same way as aquatic animals create thrust. This is more described in later Sections. Triantafyllou argue that the highest efficiency occur in the range of $St = 0.25 - 0.35$, with a peak in the efficiency for 0.25 [20]. His study was conducted with a NACA0012 hydrofoil in a small towing tank, with chord Reynolds number 2000. The same foil profile will be used in this study..

A study show that 75% of the species which relay on flapping mechanism (swimming or flying) operate with a Strouhal number in the range of $0.19 < St < 0.41$ [36]. The same study argued that this range is tuned towards high efficiency due to natural selection.

1.6 Objective

The objective is to investigate three foils with the same span area, but with different cross sectional properties.

A design study was done to investigate how the foils will deform and to make sure the foils do not break during testing. Some part of the design will also considering to find out how the foils will deform in the loaded condition. Aircraft wings are design in the way that if the induced angle of attack get too large the wing will twist to a smaller angle of attack [8]. This will be a part of the aim in the design study, to investigate for what design this kind of twist will occur.

Objective summarized: Compare Lift, Drag (Thrust) and Power for a test range of $St = 0.10 - 0.65$, at four flow conditions ($Re = 22500, 37500, 45000, 52500$) and two phases ($\phi = 75^\circ, \phi = 90^\circ$). The results of the rigid and flexible foils are compared during on oscillation of harmonic sinus motion:

- Stiff hydrofoil with very small deformations.

- Flexible hydrofoil 1 with hollow cross section and spars, with notable deformation.
- Flexible hydrofoil 2 with hollow cross section and spars, with notable deformation. Preferable some other twist and deformation than flexible hydrofoil 1.

1.7 Outline

This master thesis is divided into 7 sections. Section 2 are a summarizing of the theory used before and after the experiments. Section 3 is describing the experimental setup and the circulation water tunnel at Marinteknisk Senter at NTNU. Section 4 is describing the design process of the two flexible hydrofoils that was made in Inventor and printed by a 3D-printer at SINTEF Ocean. Section 5 consist the initial testing and calibration of the equipment. The results from decay and the bias errors is also included in section 5. In Section 6 the results is presented and discussed. The results is from the experiment on the three different hydrofoils. Thrust, Lift, Power and efficiency is presented. Section 7 is the conclusion and recommendation of further work.

2 Theory

This section includes an overview of the theory relevant to this master thesis. This is theory regarding oscillating hydrofoils; dimensionless units, design phase in Inventor, deflection and twist of softer hydrofoils, standard deviation, finite difference and average.

2.1 Average

The average or mean is the central value of a set of numbers, the sum of values divided by the number of values. It is typically denoted with a "bar" (See Equation 2)

$$\bar{F} = \frac{1}{T} \int_0^T F(t) dt \quad (2)$$

\bar{F} is the average over the time T of the force F .

2.2 Standard Deviation

For the data oscillating around 0, the mean will be close or equal to zero and does not tell us much about the data. A better way to understand the data was to see how much the data varies within the time series. The standard deviation, σ (Equation 3), of the data series is used. Standard deviation will quantify the amount of variation of the data 5. In this way, the different times series could be compared in a better way.

$$\sigma = \sqrt{\frac{1}{N-1} \sum_{i=1}^N (x_i - \bar{x})^2} \quad (3)$$

σ is the standard deviation of the time series, x_i are the data samples, \bar{x} is the mean of all the data samples, N is the number of samples used in the time series. It is noticed that the standard deviation does not change the unit of the data.

2.3 Finite Difference

The finite difference is an approximation of the derivative in a given point. By looking at the points closest to the point of interest the derivative is found with Equation 4. A finite difference can be forward, central or backward. The method used in this thesis is central finite difference with equidistant grid Δh (Equation 5). Only on the first and the last measurement points the forward- and the backward finite difference is used. The algorithm to find the approximation of the derivative of order M with the number of grid points N at x -coordinate $(\alpha_0, \dots, \alpha_N)$ is as follows:

$$\left. \frac{d^m f}{dx^m} \right|_{x_0} \approx \frac{\sum_{v=0}^n \delta_{n,v}^m f(\alpha_v)}{(\Delta h)^m}, m = 0, 1, \dots, M, n = m, m + 1, \dots, N \quad (4)$$

$\delta_{n,v}^m$ are the finite difference coefficient's (FDC) from Table 1 in [17]. FDC depends on the order of the derivative and the order of accuracy. The order of derivative in this thesis is of order 1. The order of accuracy is 2. According to B. Fornberg a accuracy of 2 would be sufficient for the calculations done on a sinus curve with a small Δh [17]. With this assumptions and the corresponding FDC, Equation 4 can be rewritten:

$$f'(x_0) \approx \frac{-\frac{1}{2}f(x_{-1}) + \frac{1}{2}f(x_{+1})}{\Delta h} = \frac{-\frac{1}{2}u(y_{-1}) + \frac{1}{2}u(y_{+1})}{\Delta y} \approx \frac{du}{dy}(x_0) \quad (5)$$

Equation 5 was used to estimate the yaw and sway velocity (\dot{y}_{sway} and $\dot{\theta}_{yaw}$) for the power consumption during one oscillation. It was also used to find the velocity gradient du/dy from inside the boundary layer of the wall in CWT.

2.4 Non-Dimensional Units

According to Graham dimensionless numbers is: "important in biomechanics because their constancy can imply a dynamic similarity between systems, despite possible differences in medium or scale" [35]

To describe the characteristics of oscillating hydrofoils, several non-dimensional units are typically used. The units make it easier to compare results from various hydrofoil

experiments. The definition of the units used in this thesis is presented in this section.

Strouhal number St (Equation 6) is a dimensionless parameter that describes oscillating flow mechanisms [9]. Most aquatic animals, fish and whales, propel themselves with a flapping mechanism. The same concept is described in this thesis with oscillating hydrofoils. An oscillating hydrofoil, flapping mechanism for fish and birds, create a reverse Von Karman vortex street in the wake (Figure 2.1). St describes the peak-to-peak amplitude of the trailing edge motion, A , the oscillating frequency of the hydrofoil, f , and the incoming free stream velocity, U_{inf} (swimming speed of the fish).

$$St = \frac{Af}{U_{inf}} \quad (6)$$

A is two times the wake amplitude y_{sway} . A modification of Equation 6 has been used in other studies, by Anderson in 1998 [3], where A is two times the wake amplitude y_{sway} . This definition by Anderson will be used in this thesis:

$$St = \frac{2y_{sway}f}{U_{inf}} \quad (7)$$

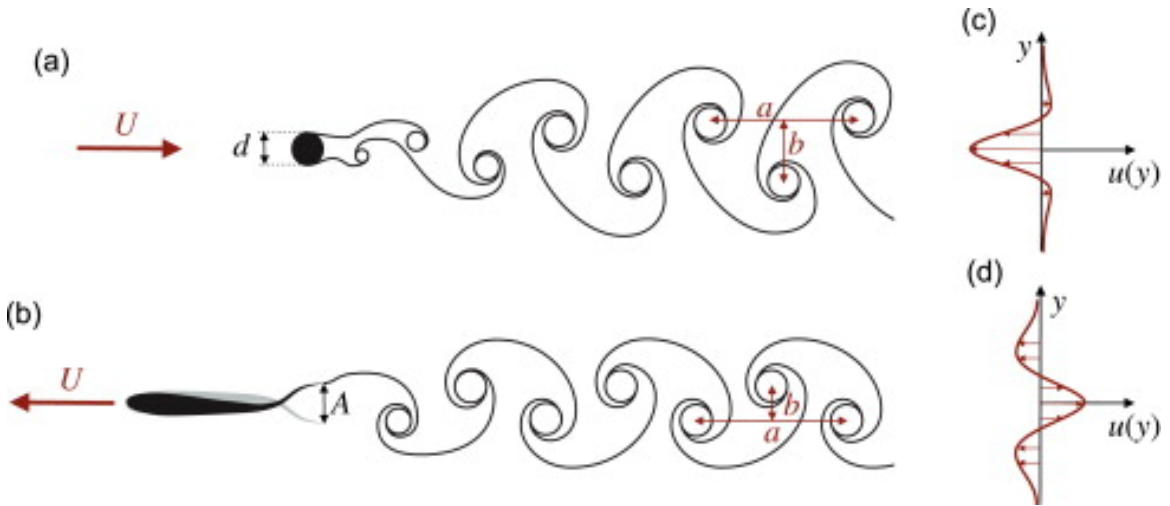


Figure 2.1: Wake with flow velocity and direction of the vortices. a) Circular cylinder creating vortex street. Extracting energy from the flow. b) Oscillating foil create reverse von Karman street, and generate thrust. Illustration from Eloy [15]

The **Feathering parameter** χ was defined by Lighthill [23] and describes the relation between the maximum yaw angle, θ , and the maximum induced angle of attack, β (Equation 8). β is the angle described by the relation between the sway motion y_{sway} and the inflow velocity U_{inf} (Figure 2.2). Figure 2.3 illustrates the plot of χ versus St for yaw angle of 10° and the frequency of motion in the test range ($f_m = 0.20 - 0.80$). For low St the feathering parameter approach 1, but will never reach 1. For high St $\chi \rightarrow 0$.

$$\chi = \frac{\theta}{\beta} = \frac{\theta}{\arctan\left(\frac{y_{sway}\omega}{U_{inf}}\right)} \quad (8)$$

ω is the angular frequency in rad/s, $\omega = 2\pi f$.

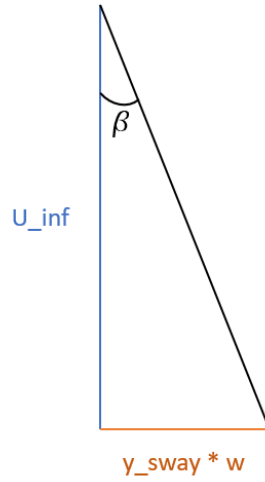


Figure 2.2: β is the relationship between the sway motion velocity $y_{sway}\omega$ and the inflow velocity U_{inf} .

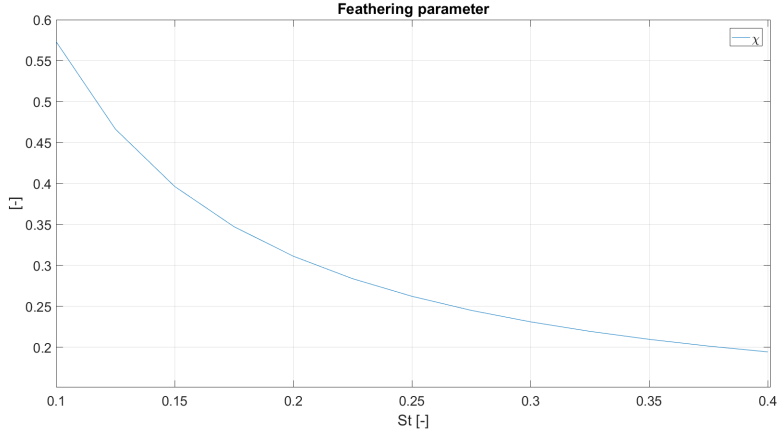


Figure 2.3: Feathering parameter χ with $\theta = 10^\circ$ and $f = 0.2 - 0.8$ Hz.

Reynolds number, Re , is the non-dimensional unit related to the turbulence level of the flow. For low Re the flow is laminar and for high the flow is stated to be turbulent [9]. In general, Re is defined as the velocity of the flow times a characteristic length L , divided by the kinematic viscosity μ :

$$Re = \frac{UL}{\mu} \quad (9)$$

In this thesis, it was more convenient to use the modified Chord Reynolds number Re_c with the chord length of the foil as the characteristic length and the free stream velocity U_{inf} (Equation 10). In this thesis the Chord Reynolds number will be referred to as Re :

$$Re_c = Re = \frac{U_{inf}c}{\mu} \quad (10)$$

2.5 Finite Element Method

This section gives a short explanation of the Finite element method (FEM) used to analyze the stress and deformation of the foil designs. The design was done in Inventor. Inventor is a CAD software developed by AUTODESK.

FEM is a numerical method to solve problems, typically structural analysis. The method divides the structure into a collection of smaller domains. Each domain represents a set of element equations. These equations are related to the original problem but are represented for each domain. All the sub-equations are systematically recombined into a global system of equations, typically describes by matrix's (Equation [11](#)). This combined system now describes the whole problem. The global system is solved by the use of known solutions, boundary condition, and initial values [26](#).

$$F = UM \tag{11}$$

Where F is the global external load matrix, U is the deformations matrix and M is the stiffness matrix. Finite Element Analysis (FEA) is the practical use of FEM. FEA includes the mesh generator which divides the structure into a mesh. The mesh is used as the sub-domains when analyzing the problem.

2.6 Shear Stress

The shear stress τ_S can be described as the stress in the material when frictional forces inside the body experience a force parallel to the cross-sectional area. Assuming that the body is longitudinally divided into several individual cross-section areas with a small thickness of Δt . The individual areas are "sliding" with respect to each other when a load parallel to the cross-section is applied. If they start to slide a friction force between the areas will work against the movement. If there were no force working against the applied load, the cross-section areas would slide to infinity. In physical materials, the sliding will be limited, depending on inter-molecule forces in the material. This inter-molecule force is the restoring force, working against the applied load on the body. The shear force is the restoring force inside the material.

The shear stress τ_S is the restoring force F_R divided by the cross-sectional area $A_{Section}$

$$\tau_S = \frac{F_R}{2A_{Section}} \quad (12)$$

A fluid has the same inter-molecule friction forces (shear forces). The wall of the test section in CWT is fixed and will not move, while the water (fluid) will move with a velocity relative to the wall. Because of the friction in the water, the water molecules closest to the wall will have the same velocity as the wall, in this case, zero velocity. This condition is known as the no-slip condition [9]. The no-slip condition creates a region where the fluid goes from zero velocity on the wall to free stream velocity further out in the fluid. This region is called the boundary layer (BL) [27]. Inside BL the change in velocity is described by the velocity gradient du/dy . The shear stress in the fluid can be estimated by the use of du/dy . The shear stress is linearly depended on du/dy (Equation [13]).

$$\tau_w = \mu \frac{du}{dy} \quad (13)$$

μ is the dynamic viscosity of the fluid. Velocity gradient, du/dy , are found by use of finite difference (Section [2.3]).

2.7 Shear Centre

This section describes the method used to find the shear centre. The shear centre is the point on the cross-section where the applied external load gives zero twist (torsion) of the section [14]. This point was found on various cross-sections, regarding the foil design. The foil design is describes in a Section [4]. The calculation was done in MATLAB (Algorithm in APPENDIX [D.2]). The cross-section was divided into four different sections, $i = A, B, C$ and D (Figure [2.4]).

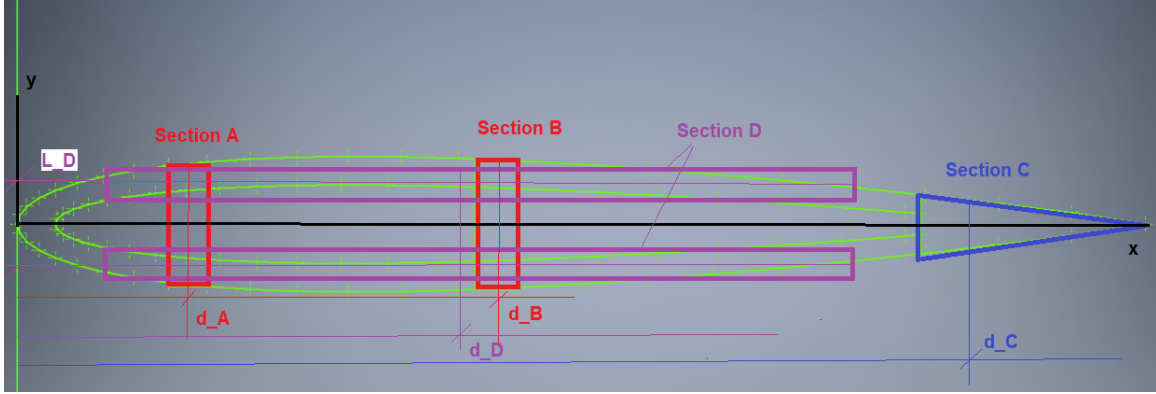


Figure 2.4: Illustrates the cross-section of the foil and how the cross-section was divided into four sections (A, B, C and D). This was done to simplify the calculation of the shear centre. The red squares are the two spars. The blue area is the solid cross-section at trailing edge. The purple area is a simplification of the thickness of the foil. Black lines is the coordinate system used in the calculations in MATLAB. d_A , d_B , d_C and d_D are distances from the centre of each respective section to the y-axis (Black line). L_D is the distance from centre of section D to x-axis.

The second moment of inertia I_{xx} (Equation 14) and the area moment Q (Equation 15) was found for each section i .

$$I_{xxi} = \frac{h_i^3 t_i}{12} + h_i t_i L_i^2 \quad (14)$$

h_i and t_i are the height and thickness of section i , respectively. For section D the Steiner's theorem ($h_i t_i L_i^2$) was used to find the moment of inertia about the parallel axis through section D. L_i are the distance from x-axis to the centre of section i (Figure 2.4)

$$Q_i = A_i d_i \quad (15)$$

$A_i = h_i t_i$ is the area of section i . d_i is the distance from origin (leading edge) to the centre of the area, for section i . With the moment of inertia and the area moment established, the shear stress, τ_i , in section i can be found by use of Equation 16:

$$\tau_i = \frac{Q_i V}{I_{xx} t_i} \quad (16)$$

V is the applied external load on the cross-section. In this thesis the external load

is assumed to be only the lift force, L . The shear force F_i in section i is found by rewriting Equation [12](#):

$$F_i = \frac{\tau_i A_i}{2} \quad (17)$$

The shear centre is found by solving the summation of moments from the shear forces F_i and the distance from origin to the shear force d_i . e is the location of the shear centre:

$$e = \frac{\sum_{i=1}^{i=4} F_i d_i}{V} \quad (18)$$

2.8 Centre of Pressure

The pressure distribution of the NACA0012 foil was obtained with *XFOIL*. *XFOIL* is a program used for design and analysis of subsonic isolated airfoils [13](#), developed by Mark Drela at MIT in the 1980's [11](#). In this thesis the use of *XFOIL* was minimal. The program has many useful functions and is easy to use, and could be used to investigate many other aspects regarding the NACA foil. However, this was not the aim of this thesis. *XFOIL* was used to obtain the pressure distribution of NACA0012 with an angle of attack in a range of $\alpha = 1 - 10$ degrees. The pressure distribution is illustrated in Figure [2.5](#)

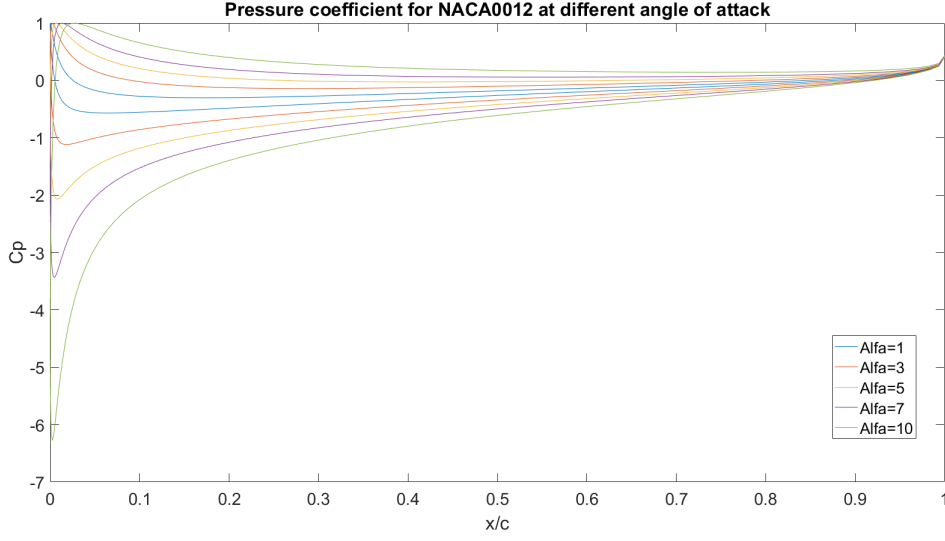


Figure 2.5: Pressure coefficient along the chord for $\alpha = 1, 3, 5, 7$ and 10 degrees. x/c are the non dimensional chord length where 0 are at leading edge and 1 are at $c = 150\text{mm}$, trailing edge

The centre of pressure for each α was obtained by numerical integration of the pressure distribution. This was done in MATLAB by use of Equation [19](#):

$$c_p = \frac{\sum_{i=2}^{i=80} (y^+(161 - i) - y^-(i))x(i)dx(i)}{\sum_{i=2}^{i=80} (y^+(161 - i) - y^-(i))dx(i)} \quad (19)$$

$y^+(i)$ is the upper side of the graph at point i for C_P and $y^-(i)$ is the corresponding lower point. $x(i)$ is the distance from the area i to the leading edge $x/c = 0$. In *XFOIL* the foil is divided into 160 point, 80 on each side (top and bottom of foil). The numerical integration starts at trailing edge. This was easiest to do since the data that comes from the *XFOIL* starts at trailing edge. With this approach the last area to calculation will be between point 79 and 80, at leading edge. The integration step $dx(i)$ is the distance between two corresponding points (Equation [20](#)). According to Equation [20](#) either the first or last area in the graph was not included. This is because in MATLAB subscript i must be real positive integer (1, 2, 3.. etc.) It was decided that the area between the two first points at trailing edge was not included in the calculations. Lower limit $i = 2$ to avoid incomplete area at trailing edge. From

Figure 2.5 the area at trailing edge $x/c = 1$ is small compared to the area at leading edge. By not including the small pressure area at trailing edge, this will not have significant effect on the results for finding the centre of pressure.

$$dx(i) = x(i) - x(i - 1) \quad (20)$$

$x(i)$ is the x-coordinate at point i and $x(i - 1)$ is the x-coordinate of the point before. The integration method is illustrated in Figure 2.6

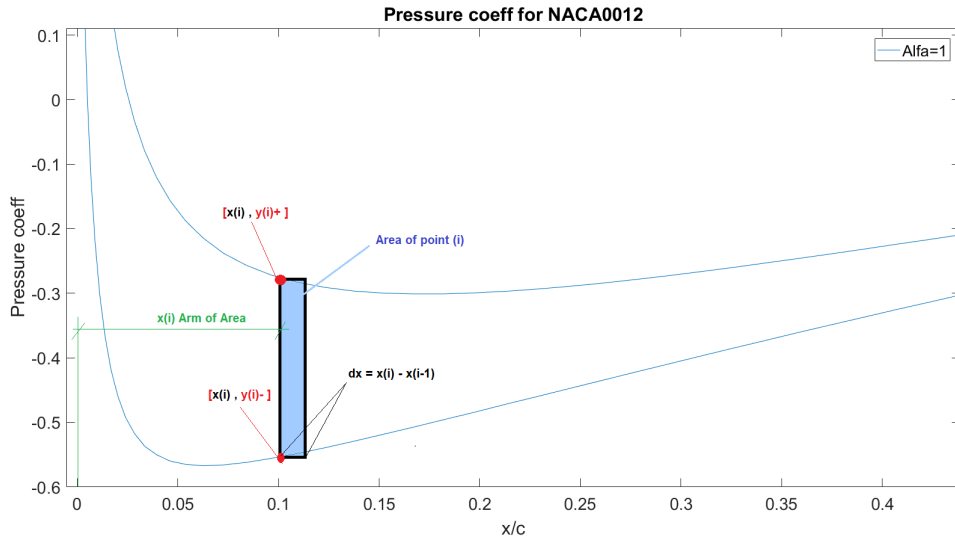


Figure 2.6: Illustration of how the numerical integration was made in MATLAB to find the centre of pressure for the pressure distribution obtained from *XFOil*

2.9 Angle of Attack

Angle of attack (AoA or α) is an important parameter and is obtained by the use of Hover's equation [22] for an oscillating foil (Equation 21). The foil has two components that effect the motion the most: motion in sway direction y_{sway} and rotation in yaw direction θ .

$$\alpha(t) = \theta(t) + \beta(t) = \theta(t) - \arctan\left(\frac{\dot{y}_{sway}(t)}{U_{inf}}\right) \quad (21)$$

U_{inf} is the free stream velocity. $\theta(t) = \theta_{yaw} \sin(\omega t + \phi)$ is the yaw position in radians, with phase ϕ and yaw amplitude θ_{yaw} . Sway motion $y_{sway}(t) = y_{sway}^{amp} \sin(\omega t)$, with sway amplitude y_{sway}^{amp} . The foil rig can move 0.16 m in sway, 0.08 m from the centre line. To make sure the tests is within the limit of the rig, the sway amplitude is $y_{sway}^{amp} = 0.075$ m. To avoid large measurement error a large AoA is used in the experiments to get larger lift on the foil. Bösch had some trouble with the result for small AoA and the smaller forces. He was not sure what the reason for the strange results with low AoA was. He argued that for low forces the strain gauges bridge does not produce enough output to be distinguished from the noise in the electrical system of the amplifier. This leads to large measurement errors [7]. To avoid this larger AoA is used, and $\theta \geq 10^\circ$. Anderson used a slightly different equation to find the numerical value of the maximum AoA, α_{max} . Anderson's equation will be used in this thesis (Equation 22). In Figure 2.7 α_{max} versus St is plotted for $\theta = 10^\circ$.

$$\alpha_{max} = \beta - \theta = \arctan\left(\frac{2y_{sway}^{amp}\omega}{U_{inf}}\right) - \theta \quad (22)$$

$\omega = 2\pi f$ is the frequency of the foil motion. In Figure 2.7 α_{max} is plotted as a function of St .

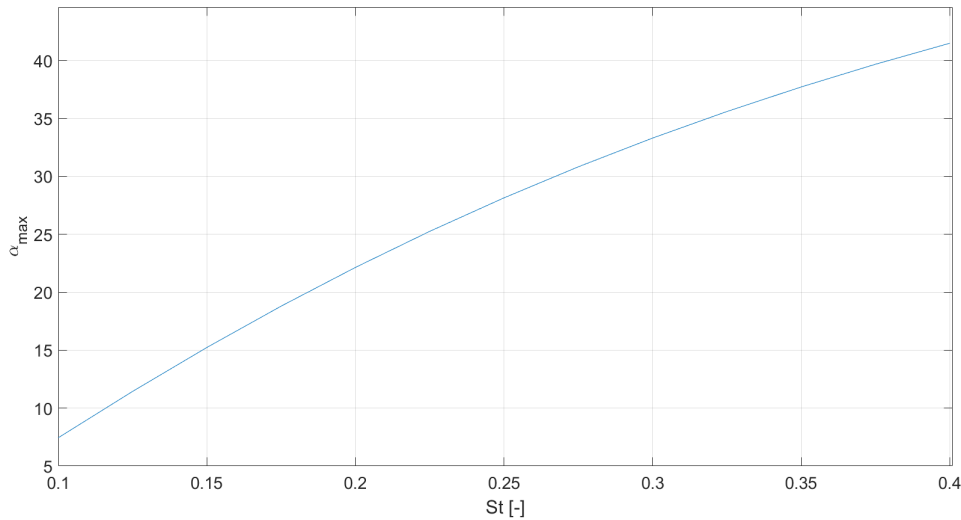


Figure 2.7: Maximum AoA for the test range of $St = 0.1 - 0.4$, $\theta = 10^\circ$.

2.10 Twist Angle

If the loads on the foil get large enough and the foil does not have sufficient stiffness, the foil will start to deform. This deformation can create a twist angle relative to the water onto the foil. If the NACA0012 foil is made by a softer material, the foil will deform if the load on the foil is large enough. This deformation might make the profile to twisted around the z-axis. If the foil twists around z-axis the nose-tail line will rotate (Figure 2.8) and affect the lift on the foil. This effect is to be measured and investigate. The results from the softer foils will be compared with a stiff foil that will have negligible twist and deformation. The twist angle Θ is important to check whether the loaded foil will twist to a higher or lower angle of attack. The twist angle is defined according to Figure 2.8.

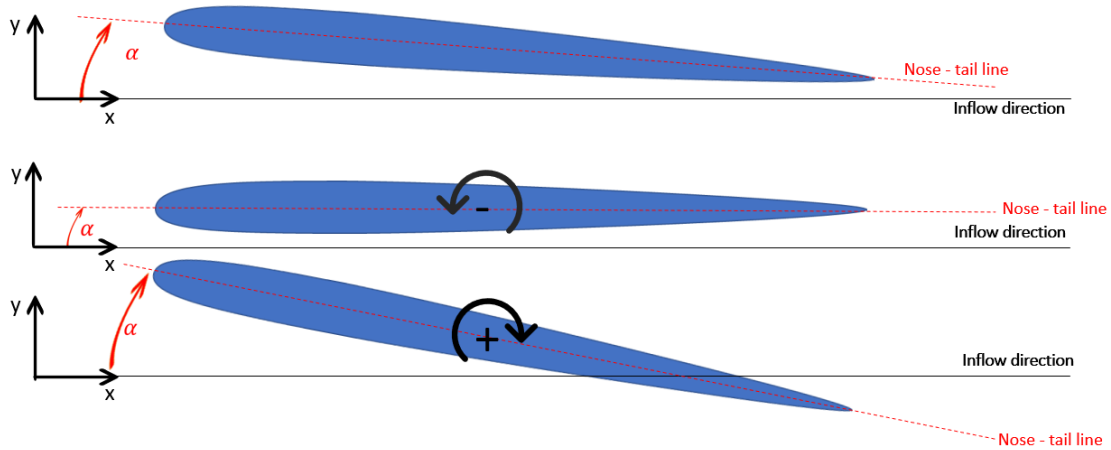


Figure 2.8: Definition of the twist angle Θ , camber line and nose-tail line

For a symmetrical and infinity stiff NACA0012 foil the camber line (mean line) will be the same as the nose-tail line. The nose-tail line is the straight line between leading- and trailing edge [24]. According to linear theory, the lift on the foil will only occur due to an angle of attack of the foil relative to the inflow.

The twist of the foil in Inventor was found by taking the absolute value of the difference in displacement between leading and trailing edge (Equation 23). The twist was

measured at the free end of the foil. The other end was assumed fix when analyzed in Inventor. When testing the foils in CWT, the upper part of the foils will be fixed at the upper part. The foils will be fixed at the end. This end is connected to the rig that creates the movement of the foils. The definition of the displacement at leading and trailing edge is illustrated in Figure 2.9. The displacement of the free end was found by use of "probes" in Inventor.

$$\Delta\delta = |\delta_{trailing} - \delta_{leading}| \quad (23)$$

$\delta_{trailing}$ and $\delta_{leading}$ is the displacement for the free end of the foil in Inventor (Figure 2.9)

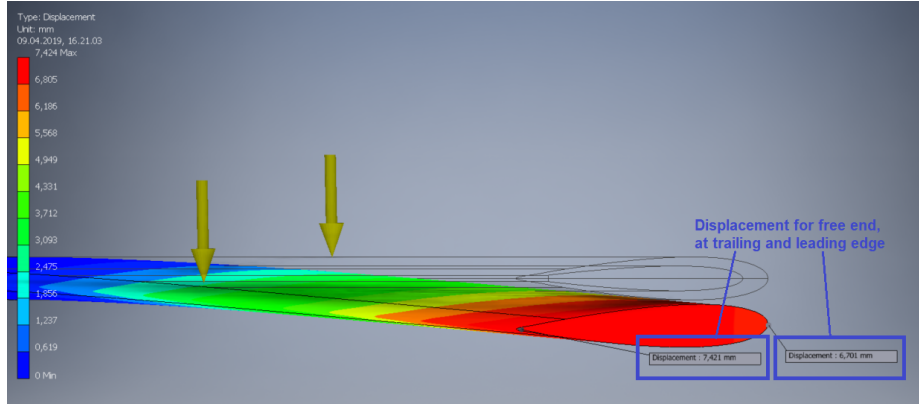


Figure 2.9: The free end displacement found by applying probes at leading and trailing edge in Inventor. The displacement of leading and trailing edge was used to calculate the twist $\Delta\delta$ and the twist angle Θ

When the twist of the foil $\Delta\delta$ was known the twist angle Θ was found by use of trigonometry (Equation 24). The calculation for all the different designs was done in Excel.

$$\Theta = \arctan\left(\frac{\Delta\delta}{c}\right) * \frac{180}{\pi} \quad (24)$$

c is the chord length. $\frac{180}{\pi}$ was used to get the answer in degrees and not radians.

2.11 Foil Theory

In the calculation for the initial design phase, linear foil theory was used to estimate the lift on the foil. Linear foil theory is commonly used in the initial design of hydrofoils and propellers. The assumptions for linear foil theory is a thin foil, small AoA and small camber [24] :

- Thin foil: The maximum thickness of the foil t_{max} is much smaller than the chord length c , in other words $t_{max} \ll c$. In general, the thickness ratio of t_{max}/c is assumed to be smaller than 0.1 for linear foil theory [2]. In this thesis, a NACA0012 foil profile is used. As the name implies, the NACA0012 foil has a maximum thickness, t_{max} , of 12 % of the chord length. This implies $t_{max}/c = 0.12$, which is greater than 0.1.
- Small angle of attack. In general $\alpha < 10$ degrees [2]. *XFoil* does not use thin foil theory, but *XFoil* was used to obtain the lift coefficient to be used in the estimation of the lift force on the NACA0012 profile. The maximum lifting coefficient $C_{L_{max}}$ found in *XFoil* was 1.6. This was for $\alpha = 16$ degrees. The large α and C_L was used to get a conservative result concerning the initial calculations to get an estimate on the deformation of the foil. It is also assumed that C_L is linear for $\alpha \leq 16$ degrees [2]. As the C_L is linear for $\alpha \leq 16$ degrees, the lift force L is assumed to be linear as well. The linear theory is valid.
- Small camber on the foil. In general camber to chord ration smaller than 0.1 [2]. In other words $z_{max}/c < 0.1$. The stiff and flexible there is no camber, $z_{max}/c = 0$.

2.12 Force and Force Coefficients

This section gives a short description of how the measured forces are taken care of in the post-processing and the definition of the non-dimensional force coefficient's.

2.12.1 Thrust and Power

The thrust force, T , and the power consumption, P , was oscillating as the foils moved. To get a specific value for T and P the mean value over one period was used. The

mean value of the thrust, \bar{T} , was obtained by integrating the drag force over several periods and divide on the number of periods used in the integration. To get more data 18 periods were used. This is described by Equation 25 and 27.

$$\bar{T} = \frac{1}{18T} \int_0^{18T} F_D(t) dt \quad (25)$$

$F_D(t)$ is the drag force at time t from the time series. The non-dimensional thrust coefficient, C_T , was found with Equation 26.

$$C_T = \frac{\bar{T}}{\frac{1}{2} \rho c s U_{inf}^2} \quad (26)$$

ρ is the fresh water density, c is the chord length, s is the span length and U_{inf} is the free stream velocity onto the foil. The shaft is the point where the foil is fixed to the foil rig. The energy through the shaft to the foil is due to the lift force, $F_L(t)$, and the sway velocity. Another contribution is the moment around the z-axis, $M_z(t)$, and the yaw velocity. The contribution of these four components represents the energy through the shaft. In other words, the power used to move the foil with the given motion in sway and yaw. The mean power, \bar{P} was obtained in the same way as \bar{L} , by integration over 18 periods:

$$\bar{P} = \frac{1}{18T} \left[\int_0^{18T} F_L(t) \frac{dy_{sway}(t)}{dt} dt + \int_0^{18T} M_z(t) \frac{d\theta_{yaw}}{dt} dt \right] \quad (27)$$

t is the time variable from the time series, $\frac{dy_{sway}(t)}{dt}$ is the sway velocity and $\frac{d\theta_{yaw}}{dt}$ is the yaw velocity. The non-dimensional power coefficient, C_P , is \bar{P} divide by the fresh water density, ρ , chord length, c , span length, s and third power of the free stream velocity, U_{inf}^3 :

$$C_P = \frac{\bar{P}}{\frac{1}{2} \rho c s U_{inf}^3} \quad (28)$$

2.12.2 Propulsion Efficient

The propulsion efficient, η_p , is defined as the energy used by the foil to create thrust. For high η_p a large thrust is generated with relative low use of energy (power). η_p is the ratio between \bar{T} and \bar{P} . η_p is a non-dimensional parameter. To accomplish this we take U_{inf} times \bar{T} . Another way of presenting η_p is to use the two non-dimensional coefficients C_T and C_P :

$$\eta = \frac{\bar{T}U_{inf}}{\bar{P}} = \frac{C_T}{C_P} \quad (29)$$

2.12.3 Lift

Lift, L , is generated due to the induced AoA when the foil is moving in sway and yaw. For this type of motion, L is oscillation around 0, and AoA was present in both sway directions. Indicating that lift was oscillating with a frequency two times the motion frequency. The direction of L is defined with respect to the coordinate system. Positive L in positive y-direction (Figure 3.11). A convenient way to present data oscillating around 0 is to use the Standard deviation, σ , of the times series. Standard deviation was used for L as described in Equation 30.

$$\sigma(L) = \sqrt{\frac{1}{N-1} \sum_{i=1}^N (L_i - \bar{L})^2} \quad (30)$$

$\sigma(L)$ is the standard deviation of the lift, \bar{L} is the mean lift, N is the number of data samples in the time series and L_i is the lift at data sample i . $\sigma(L)$ was used to find the lift coefficient, C_L , with the same constants as for C_T :

$$C_L = \frac{\sigma(L)}{\frac{1}{2}\rho c_s U_{inf}^2} \quad (31)$$

2.12.4 Moment

The standard deviation (σ) is also used to present data from the moment around z-axis, M_z (torque on the foil). M_z is the torque the shaft experience when the foils is rotating in yaw.

$$\sigma(Mz) = \sqrt{\frac{1}{N-1} \sum_{i=1}^N (Mz_i - \overline{Mz})^2} \quad (32)$$

$\sigma(Mz)$ is the standard deviation of Mz , \overline{Mz} is the mean torque, N is the number of data samples in the time series and Mz_i is the torque at data sample i . $\sigma(Mz)$ was used to find the moment coefficient, C_M :

$$C_M = \frac{\sigma(Mz)}{p_d A l} \quad (33)$$

The reference area, A , is the chord length, c , times the span of the foil, s . The reference length, l , can be either c or s . In this thesis the reference length is the chord length of the foil, c . p_d is the dynamic pressure. Rewriting Equation [33](#) the moment coefficient is found by:

$$C_M = \frac{\sigma(Mz)}{\frac{1}{2} \rho c^2 s U_{inf}^2} \quad (34)$$

2.13 Post Processing

Data sampling was done at a rate of 200 Hz for all the measurement channels. They were connected to the same data acquisition system, DAQ. Inside the DAQ a Butterworth low pass hardware filter of 20 Hz was applied to all channels used in CWT. It is an analogue filter and was applied before digitizing. The data on the bin-files still needed to be analyzed. In the data series vibration and other disturbance can occur from the equipment. These disturbances can affect the results. This was handled in the post-processing. The build-in `filtfilt` function in MATLAB was used to filter out the nonphysical frequencies (noise) in the time series (Section [2.13.1](#)).

2.13.1 Filter Noise

Noise is a quite broad definition, and there are many sources of noise. One type of noise is undesirable frequencies in the measurement. In general, the noise can be divided into measurements noise and process noise [\[10\]](#). Measurements noise is typically white noise, which is frequency independent. Another type of measurements noise is nonphysical frequencies specified to the sensors, strain gauges and accelerometer. These are removed by use of low pass filter (Figure [2.10](#)). A high-pass filter is filtering out the lowest frequencies and is only keeping the highest frequencies. A low-pass filter does the opposite by removing the high frequency and keeping the low frequencies in the time series. Process noise is typically undesired dynamics in the system, such as structural vibrations and transient motion. Transient motion is, for example, motion in the x-direction for a decay test in the y-direction. This lead to undesired motion in a degree of freedom that was not to measure. This is typically low-frequency motion and is removed by a high-pass filter. Structural vibration can be excitation of eigenfrequencies of the system. Eigenfrequencies is high-frequency motion and is removed by a low-pass filter (or bandpass filter).

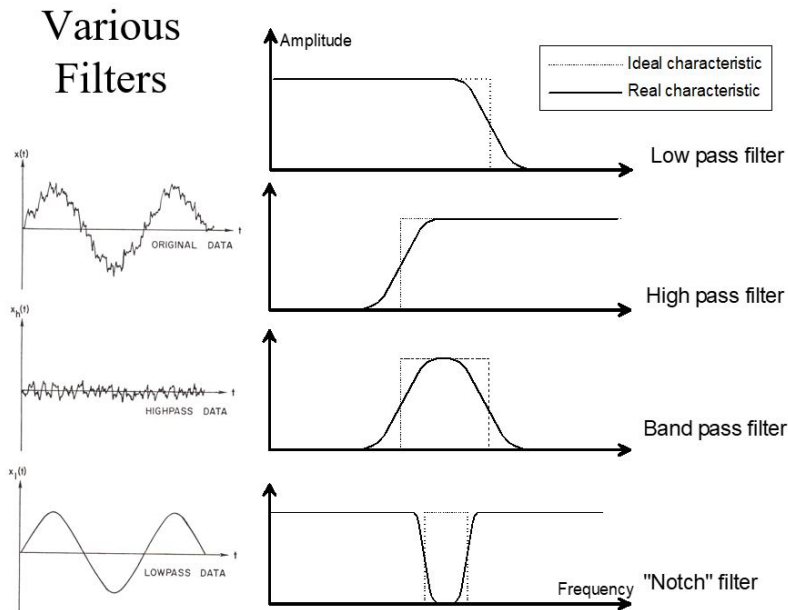


Figure 2.10: Graphical description of low pass and high pass filter used in the build-in MATLAB function "filtfilt". Low pass removes the highest frequencies, and high pass filter removed the lowest frequencies. Image from Lecture Notes [\[10\]](#)

For the filtering of the force measurements, a low pass filter was used. To know where to set the filter limits the Power Spectral Density (PSD) was used to find on which frequency the largest amount of energy was coming from and to filter out energy from nonphysical frequencies (noise). The filter limit also depends on the shape of the PSD. If the PSD is decreasing over a large range of frequencies, the filter limit needs to be moved further away from the peak in PSD. This is to ensure that the energy from physical frequency is included.

In Figure [2.11](#) the PSD of M_Z is illustrated. In this case the low pass filter limit was set to 0.6 Hz to get rid of the energy at 1.2 Hz. The PSD was obtained for all the measurement data to ensure that energy from nonphysical frequencies was excluded from the data and further calculations (Figure [2.12](#)).

It was noticed that the number of periods used in the calculations effected the integrated value and the standard deviation of the force measurement. To include

more data in the calculation 18 of the 20 periods of oscillation was used. One period was excluded at both the start and end of the time series to ensure that only "clean periods" was used. The understanding of "clean periods" is illustrated in Figure 2.13.

When the foil started to move in yaw and sway, the induced AoA was large, and the lift force got large. This large value in the start and end of the time series is in the transition period and was taken out of the measurement by only including the 18 periods in the middle (Figure 2.14). This was also done for all the other measurements, not only the lift force.

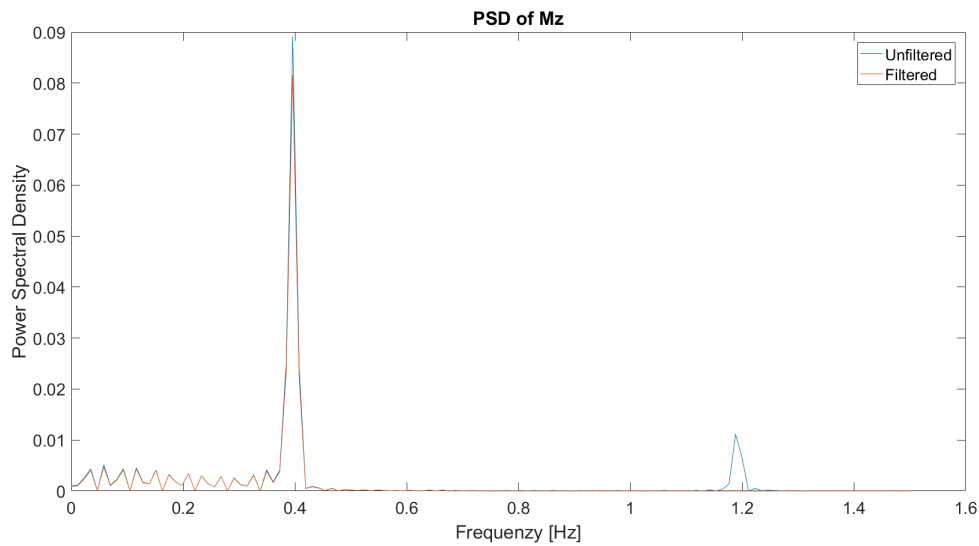


Figure 2.11: Power Spectral Density for M_Z at motion frequency of 0.4 Hz.

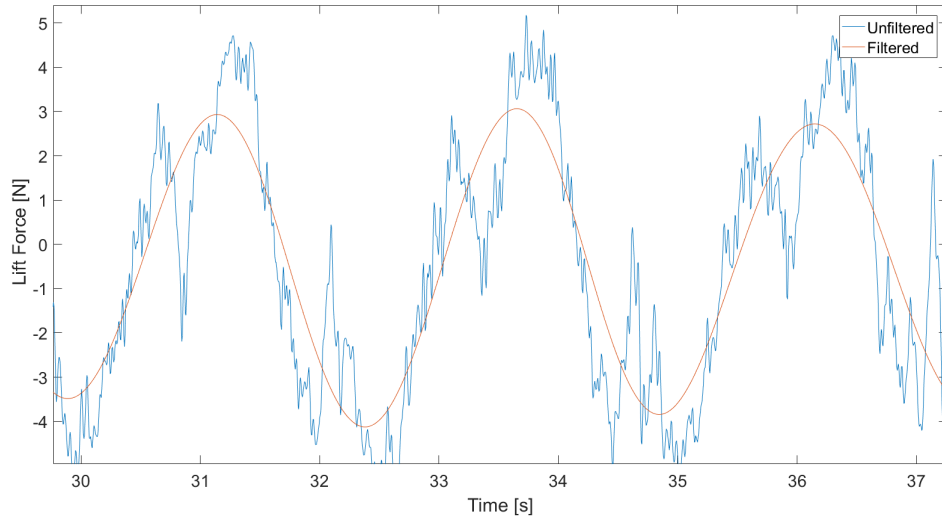


Figure 2.12: L during 3 periods of motion, with and without filter. The oscillation of the foil was $f = 0.4$ Hz. Low pass filter of 0.8 Hz was used.

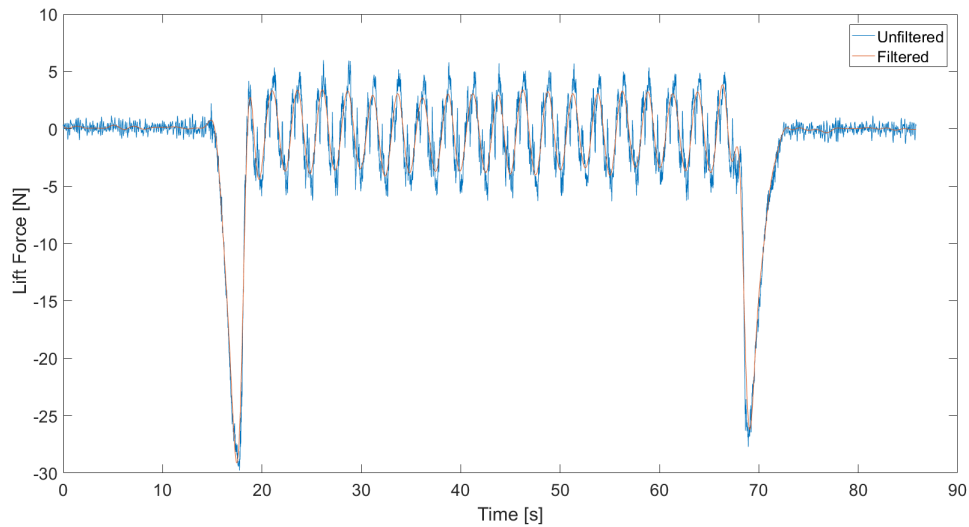


Figure 2.13: Time series of L with and without a filter. The first and last period is the transition and is excluded. The oscillation of the foil was with $f = 0.4$ Hz. Low pass filter of 0.8 Hz was used.

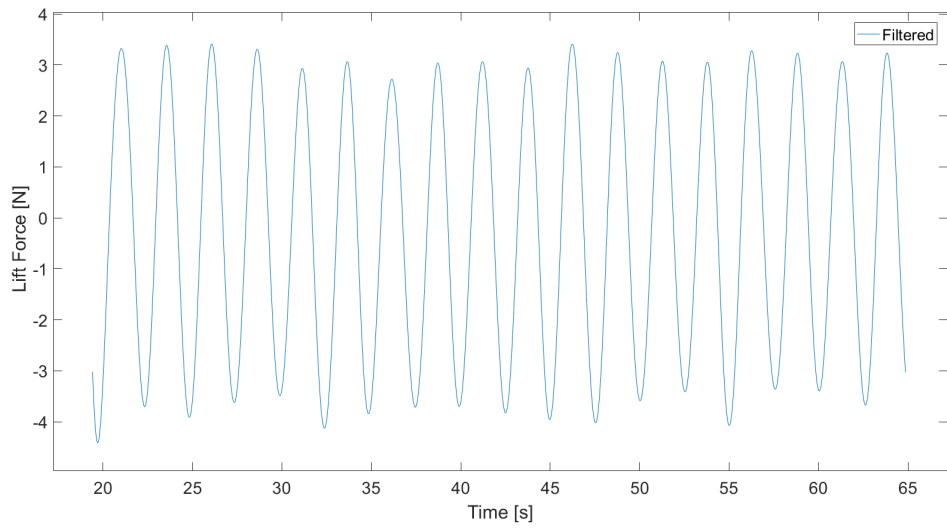


Figure 2.14: The filtered L for the 18 periods used in the calculation. Motion frequency of 0.4 Hz and low pass filter of 0.8 Hz

3 Experimental Setup

This section describes the experimental setup regarding the motion of the foils, the measurement techniques and the camera configuration that was used in the experiment.

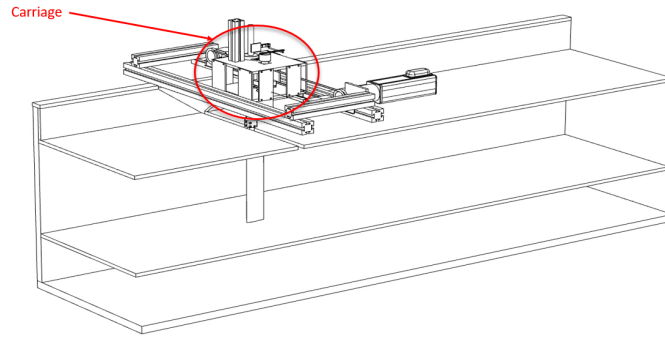


Figure 3.1: Side view of the test section with the foil rig, and the carriage.

3.1 Circulation Water Tunnel

For the experiment conducted in this master thesis, the Circulating Water Tunnel (CWT) at NTNU in Trondheim was used. CWT is a partly closed test facility where the water is circulating and the test section not moving. This makes it possible to observe the model in the test section, while the water has a velocity relative to the model and the test section. The tank can operate with water velocities from 0.0 m/s up to 1.0 m/s. Depending on the size of the geometry to test, it is possible to test laminar, transition and turbulent flow. The main dimension of the test section is $0.61 * 0.61 * 2.44 \text{ m}^3$. The test section is made of transparent plexiglass, which makes it possible to do optical experiments. A pump accelerates the water at the lowest point of the tank.

This thesis aimed to test a 2D-foil and to avoid 3D effects such as tip vortexes at the free end of the foil. This was obtained by placing an extra bottom in the test section. The new bottom was placed 209 mm from the tank bottom in the test section. The total height of the test section is 609 mm. The foil being tested has a span of 400 mm. This makes the height of the inflow stream the same length as the span of the

vertically placed foil. By doing this, it was assumed that the 3D effects most likely was avoided. The flow is free to go under the extra bottom, and will therefore not accelerate due to a change in the cross-section area. The top of the tank is made of Plexiglas to avoid free surface effects and ventilation of the foil (Figure 3.2).

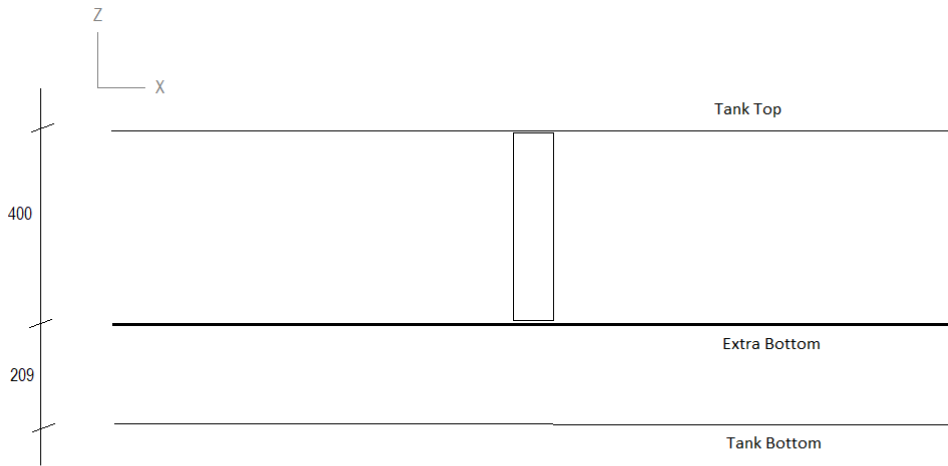


Figure 3.2: Side view of the test section, with the foil, extra bottom and the tank top.

3.2 Equipment

This section describes the equipment used in the experiment and the experimental setup. It was used two high-speed cameras, three different NACA0012 foils, a foil rig, force transducers and two electrical engines during the experiment. The result and the discussion of the results from the experiment are presented in a later section

The test rig was made by John Martin Godø for his doctoral thesis, and also used by Lennard Bösch for his master thesis. The rig can make periodic sinus motion in sway and yaw by use of two electrical engines. The rig consists of a "carriage" that runs on a belt. The belt is moving the carriage in sway direction. The motion of the belt is

made by a "Rexroth motor" (Figure 3.3). Underneath the carriage is the electric JWL engine placed vertically to rotate the foil in yaw (Figure 3.4). The foil is connected to a shaft. The arm rotates the shaft. This arm is the connection between the shaft and JWL engine. The arm consists of two joints to rotate the shaft smoothly and accurately (Figure 3.4). Both the engines are servo engines, position controlled servo. Strain gauges are located inside the silver paper at the shaft to measure forces. The rig has accelerometer at different locations on the carriage to measure accelerations in sway and yaw. The position of the carriage, relative to the rig, is also measured.

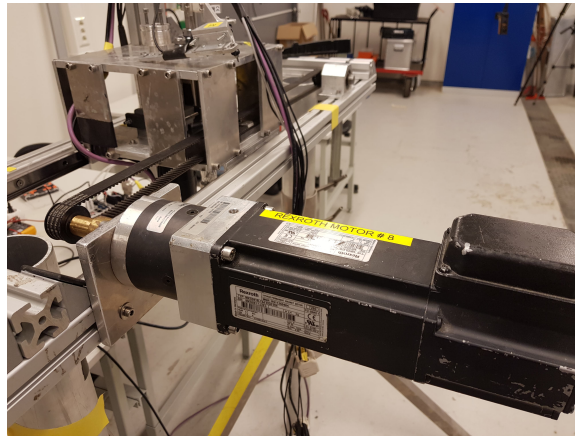


Figure 3.3: Rexroth engine connected to the belt that make the sway motion of the system. The belt is going through the "cubic geometry" on top of the rig. This cubic is the carriage.

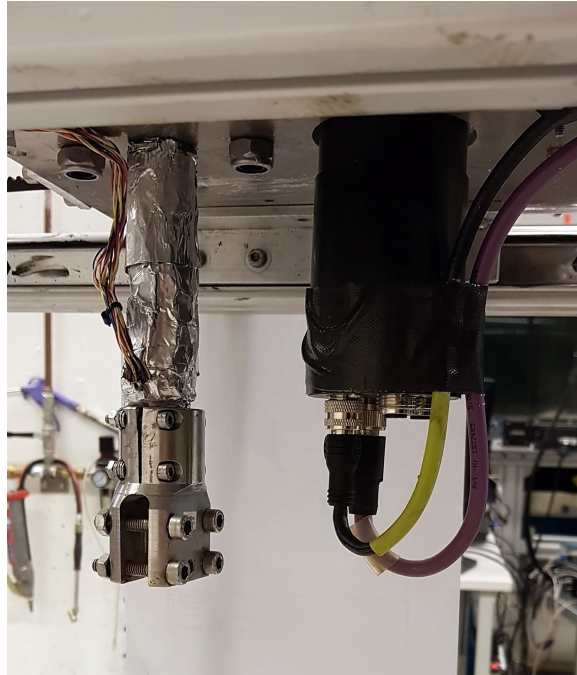


Figure 3.4: Picture taken underneath the carriage of the rig. The shaft at the left that is used to connect the foil. Inside the shaft (behind the silver paper) are the strain gauges. On the right is the JWL engine that creates the yaw motion.

Amplitude in sway and yaw and the frequency of the sinus motion is defined in the program "Foilrig". Foilrig is made by Torgeir Wahl and gives an analogue signal to the Controller to generate the sinus motion of interest. To get the correct voltage to the two engines, they need one power supply each. "Motor drive" is the power supply to the Rexroth engine. "Powersupplier" is the power supply to the JWL engine (yaw motion). Powersupplier is transforming 220 voltage alternative current to 48 voltage direct current. The signal from the Controller to the Motor drive is, and the signal from the Controller to Powersupplier is digital. An Amplifier was used to amplify the signal from the strain gauges. The Amplifier was necessary because of the low voltage from strain gauges. All the equipment are presented in Table [1](#) and an overview of the flow of information is in Figure [3.5](#).

3.3 Camera Setup

This section describes the setup of the two cameras used to measure the deflection of the two softer foils and some of the theory used to decide the configuration of the two cameras.

To measure the shape and strains of an object undergoing some 3D mechanical stress minimum of two cameras is needed, stereovision. The geometry of the stereo rig is critical to get good pictures of the displacement of the foil in this study. According to Garcia [12], the offline camera calibration procedure solves the relative distance, d , and the orientation φ of the two cameras. d is defined as the distance between the lens of the two cameras. The orientation of the cameras is defined as the angle relative to the x-axis. φ_1 for camera 1 and φ_2 for camera 2.

Relative distance is important to capture a large enough area. Due to space limitation in CWT d can be maximum 3.0 m. Another important aspect is the orientation of the two cameras, φ_1 and φ_2 . They need to be oriented in such a way that they capture a large area of the movement of the foil. The foil will oscillate in sway with an amplitude of 0.075 m. The area in which the cameras can capture is the red area in Figure 3.6. To capture a larger area, the cameras can be moved further away from the test section, in the negative y-direction. This will give a larger capture-area for a given d , but this might affect the focus and the quality of the pictures. The maximum resolution of the cameras is 512x512. It is important to get the correct focus on the foil to get an accurate measurement of the deflection in the foil [12].

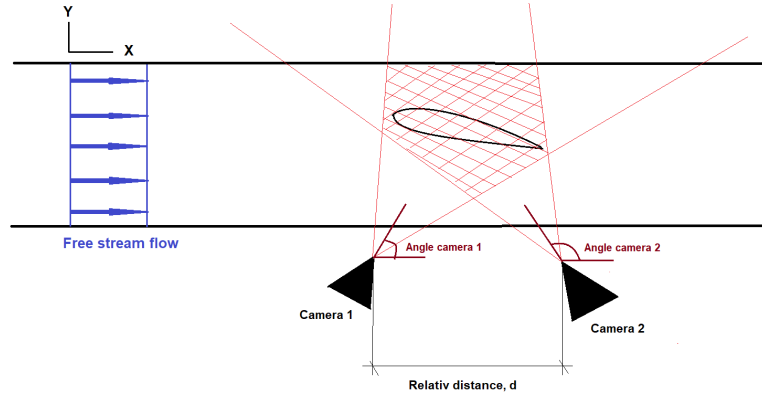


Figure 3.6: Camera setup with relative distance d and the orientation of the two cameras (φ_1 and φ_2) used to find the capture (red area)

The two cameras were connected to a synchronizer that triggered both cameras at the same time. Photron FASTCAM MH4 does the camera triggering. FASTCAM is a multi-head high-speed video system that triggers the cameras simultaneously and uploads the pictures to the computer. It can be used with up to four cameras. In this study, only two cameras were used. FASTCAM is built up by a Phase lock that enables cameras to be synchronized and a shutter that have shutter time in the range 20 ms to 6 μ s [28]. The FASTCAM is very suited for experiments on the deflection of the oscillating foil due to the low shutter time. With this low shutter time, the light is an issue. The light from a normal lamp has a much higher frequency. If the shutter time is low, only a small amount of the light from the lamp will reach the object the camera is focusing on, and the pictures will get quite dark. To compensate for a small amount of light, two powerfull lamps was used (Figure 3.8). The size of the FASTCAM and two cameras are relatively small. This makes it easy to place them and to adjust the φ and d for better pictures and large captures area (Figure 3.6). This is just a summary of the FASTCAM MH4. More information about the FASTCAM MH4 in APPENDIX C.



Figure 3.7: FASTCAM MH4 with four miniature cameras. Picture from Photron homepage [28]

A picture of the setup in the CWT-tank is illustrated in Figure 3.8. It was used two FASTCAM Photron cameras placed vertically to each other. The configuration of the cameras was chosen because of the equipment available in CWT. The mean distance between the foil and the cameras was $d = 0.53$ m. The foil was oscillating with an amplitude of 0.075 m. The maximum and minimum distance from the foil to the cameras was 0.605 m and 0.455 m, respectively.

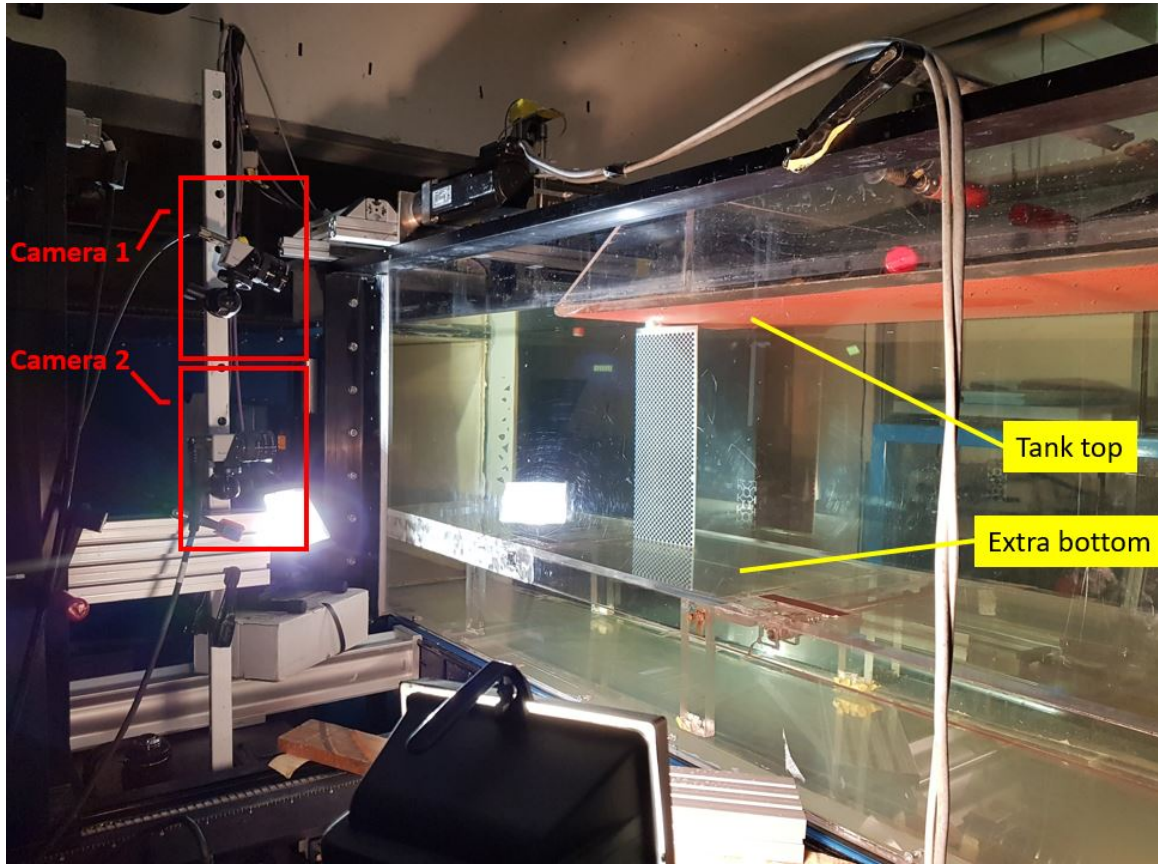


Figure 3.8: Picture of the experimental setup in CWT with the soft foil connected to the shaft on the rig. The cameras is placed on top of each other, as illustrated in the left of the picture.

3.4 Measurement

This section describe the measurement techniques used before and during the experiment.

3.4.1 Laser Doppler Velocimetry

Inflow velocity was measured with a Laser Doppler Velocimetry (LDV) device. This device measures the velocities of hollow glass particles that are seeded into the water. LDV is a type of interferometer that splits a laser source into two "beams". The two beams cross each other in the flow and create at probe volume. Because the two beams are coming from the same source and cross inside the probe volume, they create an interference pattern with light and dark stripes "fringes" inside the probe volume (Figure [3.9](#)). When the particle travels through the probe volume, it reflects light into the receiver only when it crosses a region of constructive interference. The frequency of reflection is used to measure the speed of the particle. This is done by use of the spacing of the fringes, d_f (known distance between the fringes) times the frequency of reflection, f_r :

$$U_{particle} = f_r * d_f \quad (35)$$

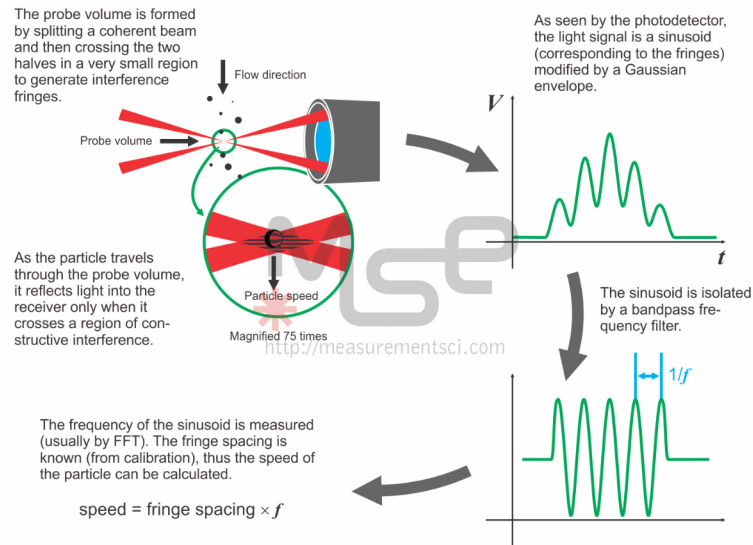


Figure 3.9: How LDV measure the velocity of the particle. Picture from MSE’s home web page [25].

The two beams must be focused at the probe volume to

- Create the smallest possible intersection zone (increasing the “brightness” of the light reflected by the particles)
- To ensure that the spacing between the fringes does not change much inside the probe volume.

3.4.2 Force Measurement

The forces on the foil were measured with several force transducers that are fixed to the foil shaft. They will measure the horizontal force F_x , cross-flow force F_y and the bending moment M_z . The force transducer measures the forces as the change in voltage through the strain gauges. This is done by sending a small voltage through the strain gauges (Figure 3.10). Inside the strain gauges, it is a resistance. The resistance will change when strain gauges are stretched or pressed together as the foil is deformed due to hydrodynamic loads. The change in resistance linearly depends on the deformation of the strain gauges. The difference in voltage before and after the strain gauge is measured and is used to measure the forces on the shaft. The

voltage is very low for small strain gauges. To get a larger signal, the signal will go through an amplifier to increase the signal, before going back to the computer (Figure 3.5). To find the amount of force for a given signal, the force transducer is calibrated to find the calibration factor. Calibration factor will be used to transform the analogue signal in voltage to Newton (N) for F_x and F_y , and Newton meter (Nm) for M_z . The calibration factor is found by load the transducer with a known load and plot the known load with respect to the analogue signal in voltage. This will give a calibration factor of N/volt and Nm/volt. It is more convenient to read the data with the unit of N and Nm instead of voltage.

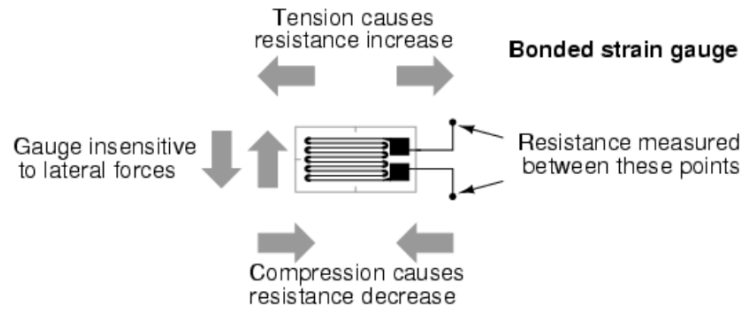


Figure 3.10: Strain gauges used as force transducers to measure the forces on the foil. Picture from [1])

When the foil is oscillating the force direction will change during one oscillation. Drag and lift force will be a function of the yaw angle θ . To find the drag and lift it is used trigonometry as described in Equation 36. The water flow is coming into the foil at $\theta = 0$. The positive directions is described in Figure 3.11.

$$\begin{aligned} F_D(\theta) &= F_x \cos\theta + F_y \sin\theta \\ F_L(\theta) &= F_y \cos\theta - F_x \sin\theta \end{aligned} \tag{36}$$

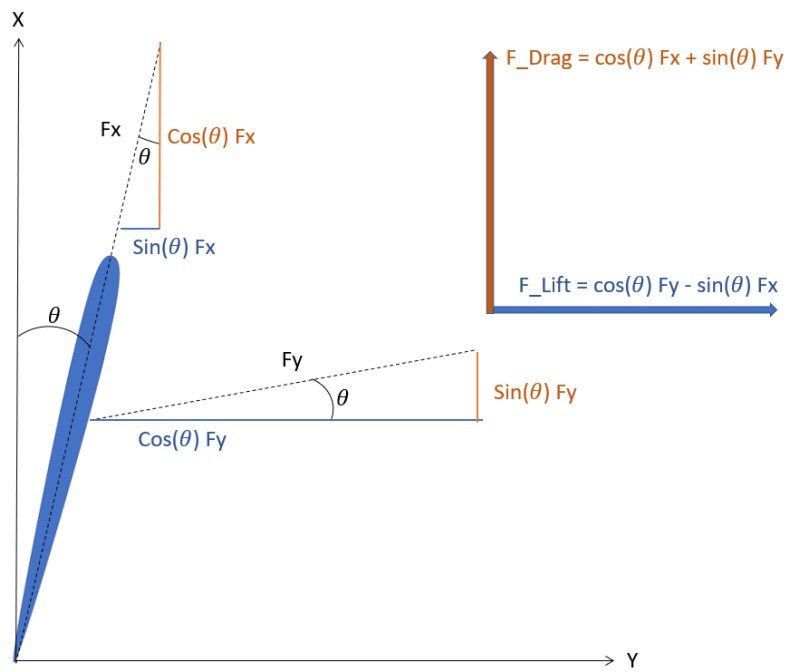


Figure 3.11: Positive directions for the force measured. Inflow onto foil is at zero yaw angle $\theta = 0$.

4 Design of Hydrofoils in Inventor

This section describes the design phase of the two soft hydrofoils used in the experiment. It also includes an overview of the work done on the hydrofoils, from early design phase in CAD to the 3D printing, to the glueing of the finished printed foils. The design of the hydrofoils was done by use of AUTODESK's CAD tool, Inventor. The printing of the hydrofoils was done by help from Nils Arne Snekvik. Snekvik also contributed to the design phase to make sure the design would not break during printing. Kristian Minde made the connection part that connects the printed hydrofoil to the shaft of the foil rig. Both Snekvik and Minde are working at SINTEF Ocean, and the help from them was crucial to complete the design. In this section, the hydrofoils are mention as foils more than hydrofoils. The final design are presented in the last subsection (Section [4.5](#)).

Inventor was used to sketching the foil. The static FEM analyze for the stress and displacement, was also done with Inventor. The displacement needed to be controlled to check whether the load was too large or too small for the 3D-printed foil with Vero Gray material from Stratasys [\[34\]](#). If the displacement were too large, the foil would deform or brake during the testing in the circulating water tunnel (CWT). If the foil were too stiff, the deformation would be too small for the cameras to detect the deformation. In the project thesis, it was found that a deformation between 1 mm and 20 mm would be sufficient for the cameras, and small enough for the foil not to break.

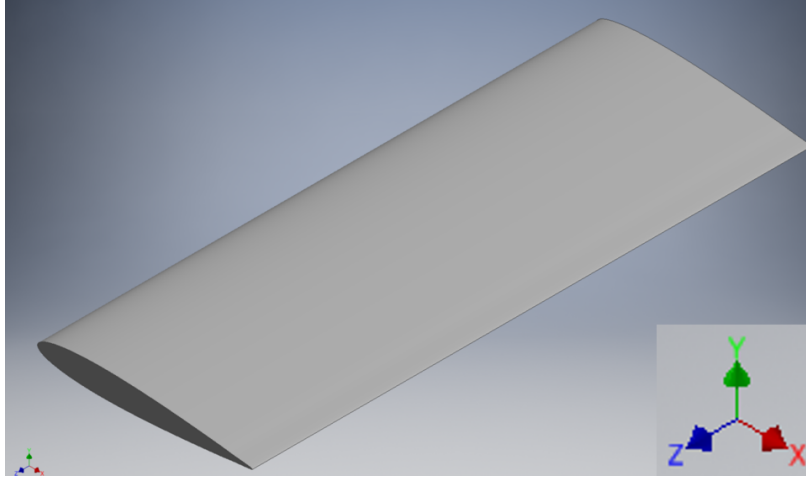


Figure 4.1: Design 1: Solid NACA0012 foil designed in Inventor made of Vero Gray material (Table 8 in APPENDIX B)

4.1 Mesh in Inventor

The average element size, minimum element size, grading factor, maximum turn angle and create curved mesh element defines the mesh in Inventor [4]:

Average element size, AES, specify the average distance between nodes on the element. Decreasing the average element size will increase the number of element and number of nodes on the body. Default AES is 0.100, but AUTODESK.help recommend 0.050 - 0.100. AES = 0.080 was used to save computational time.

Minimum element size, MES, is the minimum distance between element nodes. Default is 0.200. By decreasing this parameter, the mesh gets smaller, and the result gets better, compared to an increase in MES. It was noticed that this was a very sensitive parameter. By only decreasing AES from 0.200 to 0.150, the number of nodes and elements increased significantly. To save computational time and still get a good mesh, the MES was 0.100. MES = 0.100 is the lower limit of the recommendation from AUTODESK.

Grading factor, GF, specify the maximum grading between elements. Low GF

will give a more homogeneous mesh. By lowering the GF, better local mesh is obtained, but the number of elements increased. Default is 1.500. The smallest GF is 1.000. It seemed unnecessary to go further down. $GF = 1.500$ was used.

Maximum turn angle, MTA, specify the maximum angle arcs. By decreasing MTA, the element size decrease and the number of nodes and element increases. Default is 60 degrees. The foil does not have that many corners, and the default option is used to save computational time.

Create curved mesh element. The options are "yes" or "no". Default is "yes", and this was also used in the analyze. By not using curved elements, it produces a mesh with only straight elements. This might lead to less accuracy.

With the choice of mesh parameter, the solution converged, as illustrated in Figure [4.2](#):

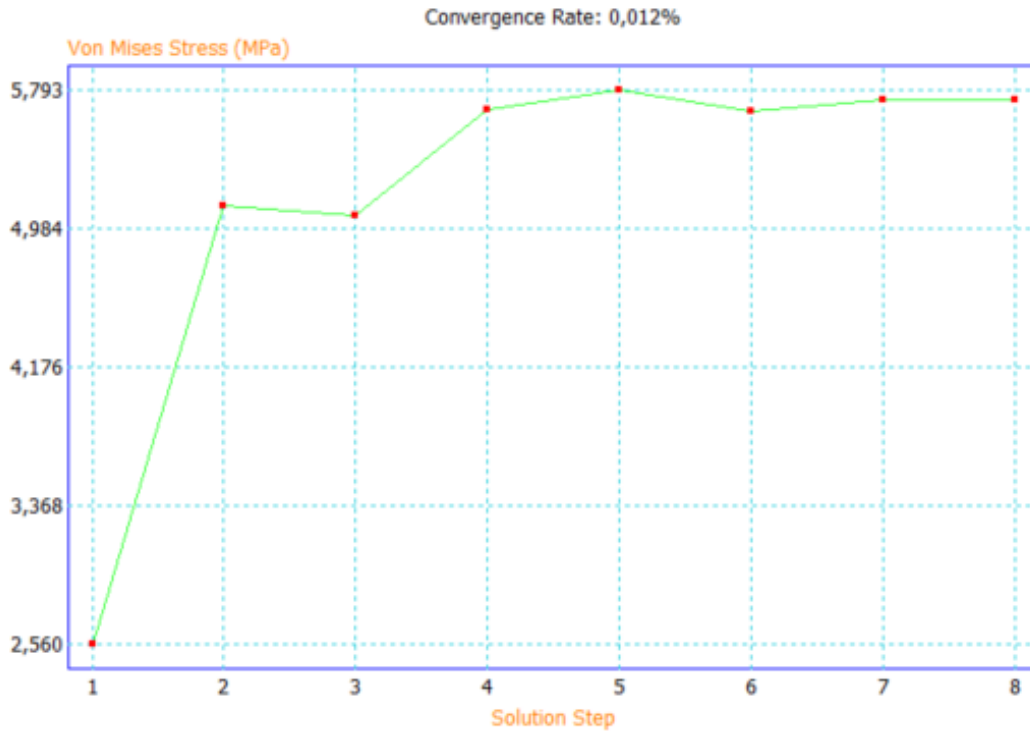


Figure 4.2: The convergence test done for the stress analyze in Inventor.

4.2 Design Process

The foil needed to be designed before the printing took place and several different attempts were made to make the foil softer for it to twist around the z-axis (See coordinate system in down right corner of Figure 4.1). The aim of the design phase was to check the displacement, stress and twist of the foil. The lift induced by the foil was found by the use of linear foil theory (Section 2.11) and the pressure distribution obtained from *XFoil*.

4.2.1 Theoretical Lift on the foil

Assuming linear foil theory Equation 37 can be used 33.

$$L = \frac{1}{2} \rho c_s C_L U_{inf}^2 \quad (37)$$

By use of the known parameters for the lifting condition: L was found with linear lifting line theory assuming a maximum lift coefficient $C_L = 1.6$ (from *XFOIL*), max free stream velocity onto the foil $U_{max} = 1.0 \text{ m/s}$, fresh water density $\rho = 1000 \text{ kg/m}^3$, span $s = 0.4 \text{ m}$ and chord length $c = 0.15 \text{ m}$. The lift force on the foil becomes $L = 48 \text{ N}$. This theoretical lift force was used in the design phase to estimate the deflection and twist, to make sure the softer foils would not break.

4.3 Initial Design

The initial design was a solid cross-section with NACA0012 foil profile, with cord $c = 150\text{mm}$ and span $s = 400\text{mm}$ (Design 1, Figure 4.1). Assuming constant and homogeneously lift force on the foil $L = 48 \text{ N}$, found with linear lifting theory (Section 4.2.1) The maximum Von Mises stress, displacement and twist angle was found with FEM analyze in Inventor. For the NACA0012 profile with solid cross-section the maximum displacement and maximum Von Mises stress was $\delta_{max} = 5.4 \text{ mm}$ and $\sigma_{max} = 4.3 \text{ MPa}$, respectively. This was enough displacement for the cameras to notice the deflection, and there was a sufficient amount of stress. The foil will not break under these conditions. The twist angle $\Theta = 0.1^\circ$ was not a sufficient twist on the foil. This design made the foil too stiff. A second design was done by making a hollow foil. This was done by making the same solid NACA0012 cross-section. To make the foil hollow a NACA0008 profile was used with the build-in extrude function in Inventor to remove volume inside the NACA0012 profile. (Figure 4.3)

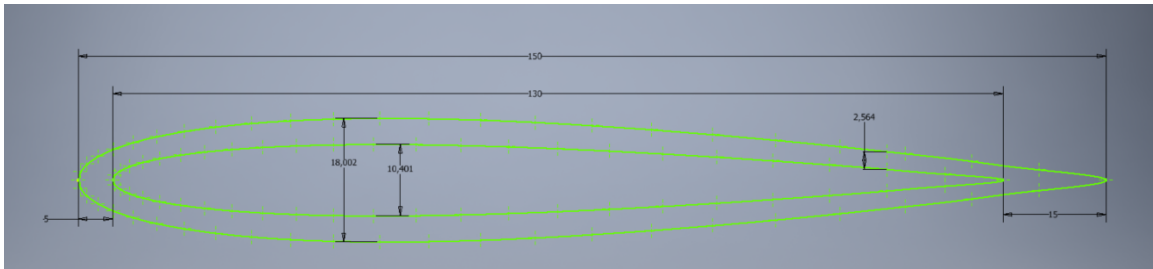


Figure 4.3: Design 2: 150 mm long NACA0012 foil profile with 130 mm long NACA0008 foil profile inside. NACA0008 starts 5 mm "to the right" and ends 15 mm before NACA0012.

The cross-section in cord direction are illustrated in Figure 4.3. It has a 150 mm long

NACA0012 foil profile with 130 mm long NACA0008 foil profile inside. NACA0008 starts 5 mm inside and ends 15 mm before NACA0012. This design was done to make sure there was enough thickness at leading and trailing edge of the foil. A large amount of work was done in the design phase to make sure the foil not to break under printing and when tested in the tank with applied lift and drag caused by the foil.

Max values	Design 2
Von Mises Stress σ	3.53 MPa
Displacement	7.42 mm
Twist $\Delta\delta$	1.06 mm
Twist angle Θ	0.27°

Table 2: Results from FEM analyze for design 2 done in Inventor with an average element size of 0.08, grading factor on 1.5 and minimum element size of 0.1. For the build in convergence test in Inventor the stop criteria was 1% and refinement threshold on 0.95.

4.4 Second Design

The new contribution to the design was spars inside the hollow part of the foil. The spars was placed with an angle relative to the inflow. The spar angle was 0°, 45° and 135° relative to the inflow. Five spars with spacing was placed inside the foil. The thickness of each spar was 10mm (Figure 4.4 and 4.5). The three designs was analyzed in Inventor and compared to see how the new design effected the stress, displacement and twist of the loaded foil (Table 3)

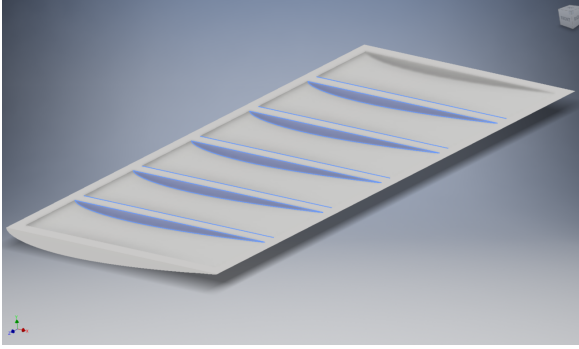


Figure 4.4: Design 3: Five spars (blue area) with thickness of 10mm and spacing of 65mm. spar angle of 0° relative to U_{inf} .

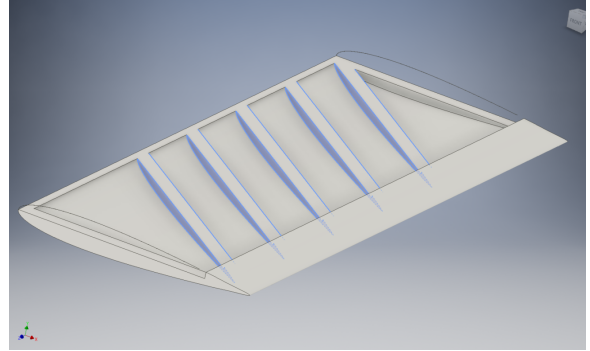


Figure 4.5: Design 4 and 5: Five spars (blue area) with thickness of 10mm and spacing of 65mm. spar angle 45° and 135° relative to U_{inf} .

	Design 3	Design 4	Design 5
spar angle	0°	45°	135°
Von Mises Stress	5.76 MPa	3.43 MPa	3.83 MPa
Displacement	7.09 mm	6.76 mm	6.57 mm
Twist	0.55 mm	0.36 mm	0.43 mm
Twist angle	0.21°	0.14°	0.16°

Table 3: Results from FEM analyze on design 3, 4, and 5 done in Inventor with an average element size of 0.08, grading factor on 1.5 and minimum element size of 0.1. For the build in convergence test in Inventor the stop criteria was 1% and refinement threshold on 0.95.

It was noticed that design 3, 4 and 5 did not give a larger twist on the foil. The foil was intended to be stiffer than earlier design with the appearance of the spars. Design 4 and 5 gave a smaller twist than design 2, with only a maximum twist of 0.36 mm and 0.43 mm, respectively. A final attempt was done on the spar design to make the foil twist and deform. The design was made softer by removing some of the volume in the middle of the spars (Figure 4.6). The foil was still too stiff to get a significant twist in the foil. The twisting was also the same for all the three foils, non-regarding the spar angle.

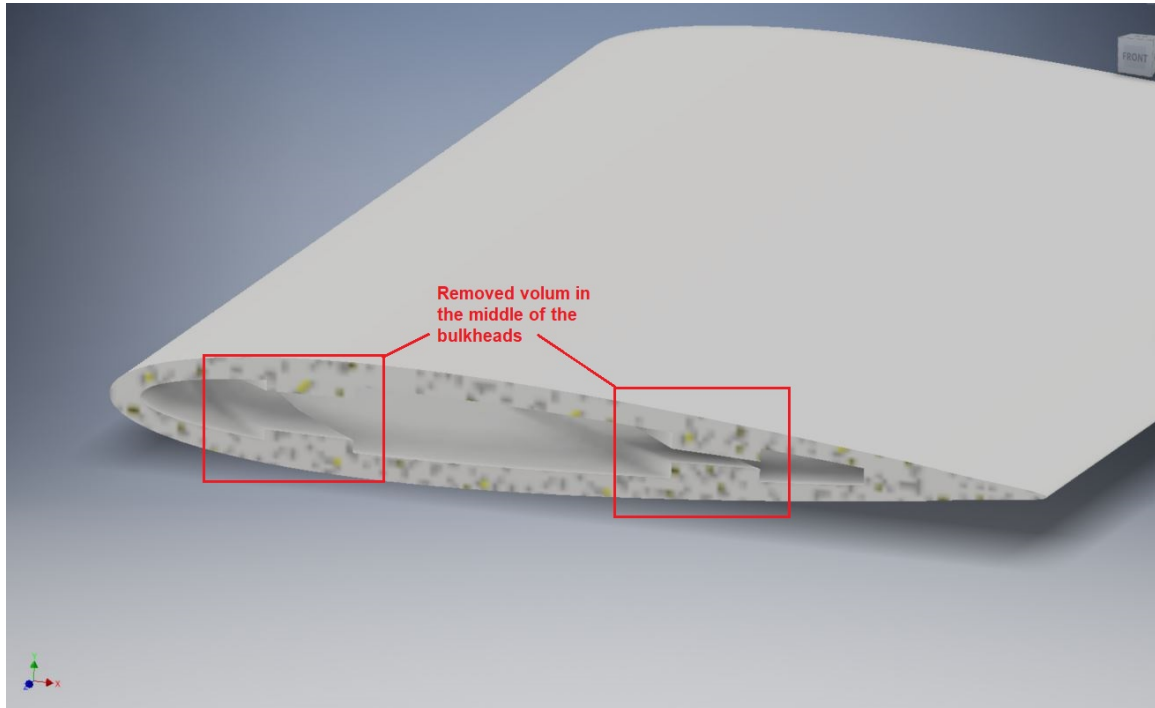


Figure 4.6: Cross section cut of Design 6. This design are the same as design 4 but volume in the spars are removed (Red box)

4.5 Final Design

The first five designs gave too little twist of the foil. So, another approach was used. The shear centre of the cross-section of the foil was calculated using beam theory (Section 2.7). Zero twist is obtained if the shear force goes through the shear centre of the cross-section [14]. The shear force on the foil will be the lift force L . The pressure distribution describes the lift force distribution. By ensuring twist, the shear centre should be outside the centre of pressure. The calculation of the shear centre was done in MATLAB (APPENDIX D), for different cross-section designs. The different shear centre was compared with the centre of pressure c_p . The pressure distribution was obtained with *XFOIL* and plotted with MATLAB. Numerical integration was used to find c_p (Section 4.5.1).

4.5.1 Finding Shear Centre of the Design

In the calculation of the shear centre done in MATLAB, the spars were placed relative to the leading edge. The design consists of two spars, placed along the span (normal to the water inflow). Snekvik suggested that the trailing edge could be printed as a solid cross-section so that the trailing edge might not break at the tip during printing, and also when glueing the two parts together (Figure 4.6). The solid cross-section at trailing edge was printed so that the last 20 mm of the foil was solid (From $x = 130$ mm to $x = 150$ mm). The first spar was placed close to the leading edge. The second spar was placed as close as possible to trailing edge. If the second spar was placed too close to the solid trailing edge, it was assumed that this would have a large effect on the stiffness of the foil. A large stiffness at the trailing edge is not preferable. The last spar was placed 50 mm in front of the solid cross-section at trailing edge, at 80 mm from the leading edge. In the calculations the first spar vary from $x = 20$ mm - 60 mm. The second spar at $x = 80$ mm. Thickness of both spars vary from $t = 3$ mm - 21 mm

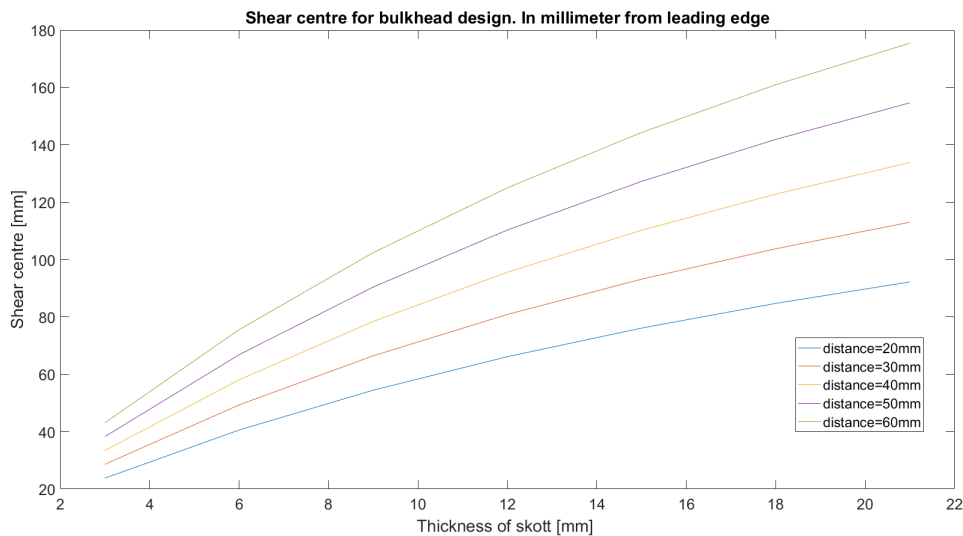


Figure 4.7: (Theoretically shear centre calculated and plotted in MATLAB for various spar designs.

Noticed in the graph; the shear centre is moved further back if the first spar is placed

further back. The graph corresponds with theory; the more cross-section area is placed further back, the more shear forces are supported by the large area in the back of the cross-section. Also, the shear centre was moved further back due to a larger thickness of the spars.

4.5.2 Finding Centre of Pressure

It is common to assume that the centre of pressure, c_p , is located close to one-quarter of the cord length. One quarter of the chord length is at $150 \cdot 0.25 = 37.5$ mm. To find c_p the pressure distribution was obtained from *XFOIL* and plotted in Figure 4.8. The pressure distribution was integrated by use of Equation 19 to find c_p for each AoA. This is presented in Table 4. The results is presented as non-dimensional length from leading edge, x/c . If $x/c = 0.1$ then x is located at a distance from leading edge equal to 10% of the chord length c . According to Table 4 the "one quarter rule of thumb" seems to be a reasonable assumption, and will be used in further calculations.

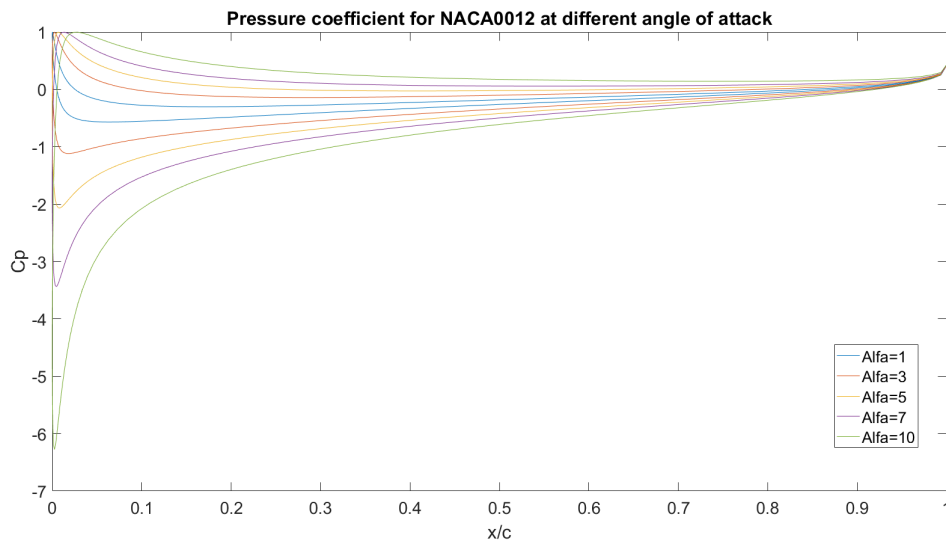


Figure 4.8: Pressure distribution from *XFOIL* for AoA = 1 - 10°

NACA0012	
α degrees	c_p x/c
1	0.2519
3	0.2790
5	0.2660
7	0.2598
10	0.2543

Table 4: Centre of pressure for different angle of attack. Obtained with numerical integration in MATLAB (Equation [19](#))

4.5.3 Definition of the Final Design

The definition of the final design for the two flexible foils was decided by use of the shear centre and c_p . The shear centre needs to be outside the centre of pressure to make the foil twist. If c_p are closer to the leading edge for the shear centre, the foil is assumed to twist to a lower AoA, and opposite with c_p behind the shear centre the foil will twist to a larger AoA.

c_p are compared with shear centre found in Figure [4.7](#). Two designs were made based on this comparison, design 6 and 7. The lowest spar thickness of 3.0 mm was decided on both the spars to get a softer cross-section. Design 6 with a theoretical shear centre in front of c_p (shear centre at 23.81mm) to aim for a twist towards smaller AoA. Design 7 with shear centre close to c_p (shear centre at 33.47mm), aims for smaller twist than design 6. Design 6 have the spars at 20 mm and 80 mm from the leading edge. Design 7 have the spars at 40 mm and 80 mm from the leading edge.

It was noticed that for all the designs analyzed in Inventor with FEA, the largest deformation occurred at the trailing edge. Indicating that all the designs have a twist to a higher AoA. In the analyze in Inventor, the force is uniformly distributed. This will not be the case for the pressure distribution when testing the foils in CWT. It is assumed that the deformation will be according to the calculations of the shears

centre and the pressure distribution. The flexible foils will twist to a lower AoA, as discussed in earlier sections. The stiffness of the foil is lowest at the trailing edge due to the small thickness. In Inventor the foil deforms the most at this point. Only static FEA was done in Inventor. The static condition will not be the case when testing the printed foils in CWT. The foils will be in a dynamic condition, oscillating both in sway and yaw.

4.6 Printing

SINTEF Ocean's Stratasys 3D-printer did the printing with Vero Gray printing material. The Stratasys printer would fill the inside of the foil with soft "support material". The support material has to be removed after printing. To avoid opening the 3D-printed foil, it was decided that the foil was divided into two parts (part 1 and part 2) and printed separately, for later to be glued together. With this printing technique, the support material would be on the outside of the foil and can easily be removed by hand. The thickness of the spars is 3 mm. The cut of the foils was made on the upper side of the foil, above the spars. The cut was made to avoid glueing two spars with thickness 3 mm together. A shelf was made, to make easier glueing (Figure 4.11). Sharp corners and edges in a structure might lead to significant large stresses at this location. An effort was made to avoid sharp edges in the design. The foils was smoothed out with the built-in fillet function in Inventor (Figure 4.9).

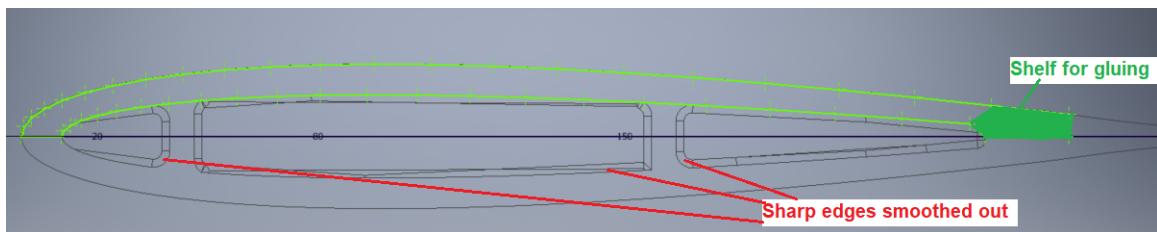


Figure 4.9: Cross section of design 6. It illustrates the separation of the foil into part 1 (Green line) and part 2 (The rest of the foil). At the end of part 1, it was made a shelf to make the glueing of the two parts easier. The red lines show wherein the cross-section the sharp edges were smoothed out with til built-in fillet function in Inventor

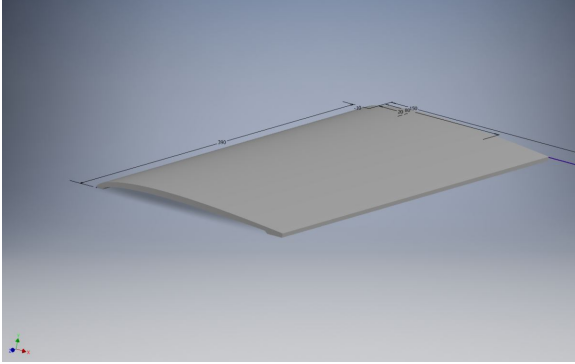


Figure 4.10: Illustrates the upper part of the foil, part 1.

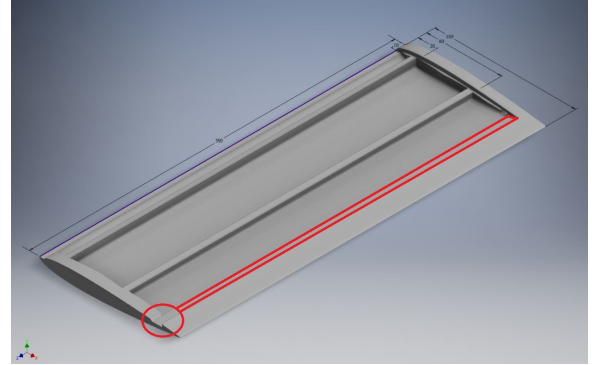


Figure 4.11: Illustrates the lower part of the foil, part 2. Part 2 consist of the two spars at 20 mm and 40 mm from leading edge. The red marked area indicate the shelf made for gluing the two parts together

Max values	Design 6 B1 = 20mm, B2 = 80mm	Design 7 B1 = 40mm, B2 = 80mm	Stiff Foil Solid
Von Mises Stress	5.68 MPa	5.32 MPa	4.31 MPa
Displacement	13.68 mm	13.44 mm	5.41 mm
Twist	1.54 mm	1.52 mm	0.27 mm
ϕ	0.59°	0.58°	0.10°

Table 5: Results from FEA done in Inventor on the final design solutions and the stiff foil. It was used an average element size of 0.08, grading factor on 1.5 and minimum element size of 0.1. For the build-in convergence test in Inventor, the stop criteria were 1% and refinement threshold on 0.95. B1 and B2 are the placement of spar 1 and 2 in mm from the leading edge of the foil. The spars are normal to the incoming flow U_{inf}

The setup for the foil rig that gives the foils motion in yaw and sway was made by John Martin Godø and Torgeir Wahl in 2015. The printed foils were also to be fixed to the same rig. This was done by glueing a stiff shaft on one side of the foils. The stiff shaft was made by steel and was cut out with the same cross-section as a NACA0012 on one side, to fit the printed foils. On the other side, the shaft was cut to fit inside

the rig setup. Kristian Minde conducted the cutting. Two shafts were made, one for each of the flexible foils (Figure 4.12).



Figure 4.12: Picture of the shaft that was designed and was attached on the top of the printed foils. The cutting was conducted at SINTEF.



Figure 4.13: The two foils that was printed with Stratasys 3D printer at SINTEF Ocean. They were printed in two parts and glued together as on Figure [4.14](#)

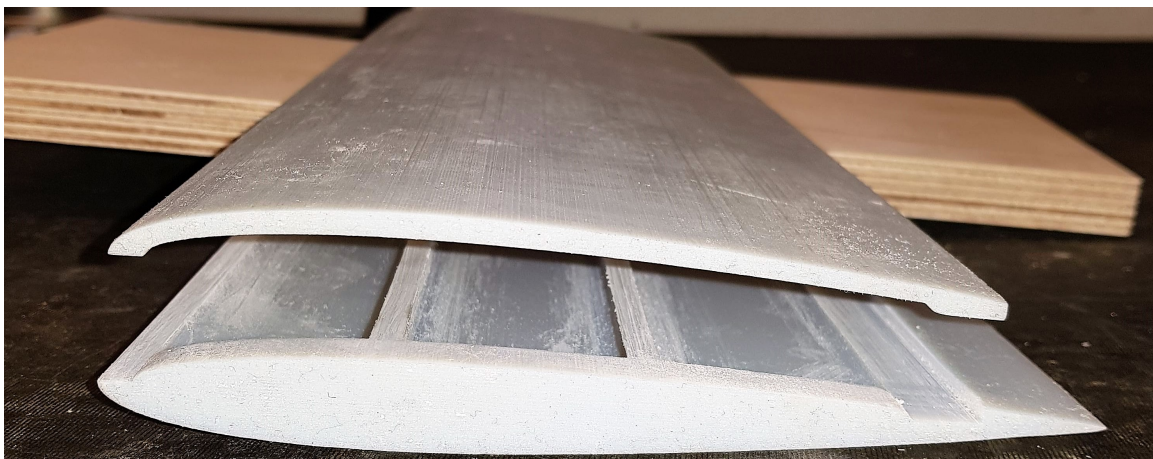


Figure 4.14: How the two parts of the foil with spars at 40 mm and 80 mm was glued together.

After the foils were glued together, and the shaft was attached to one side of the foils.

It was glued and screwed with 4.5 mm screws. It was also attached a grid pattern along the span of the foils. The grid pattern will work as a calibration pattern and also measure the deflection of the foils.

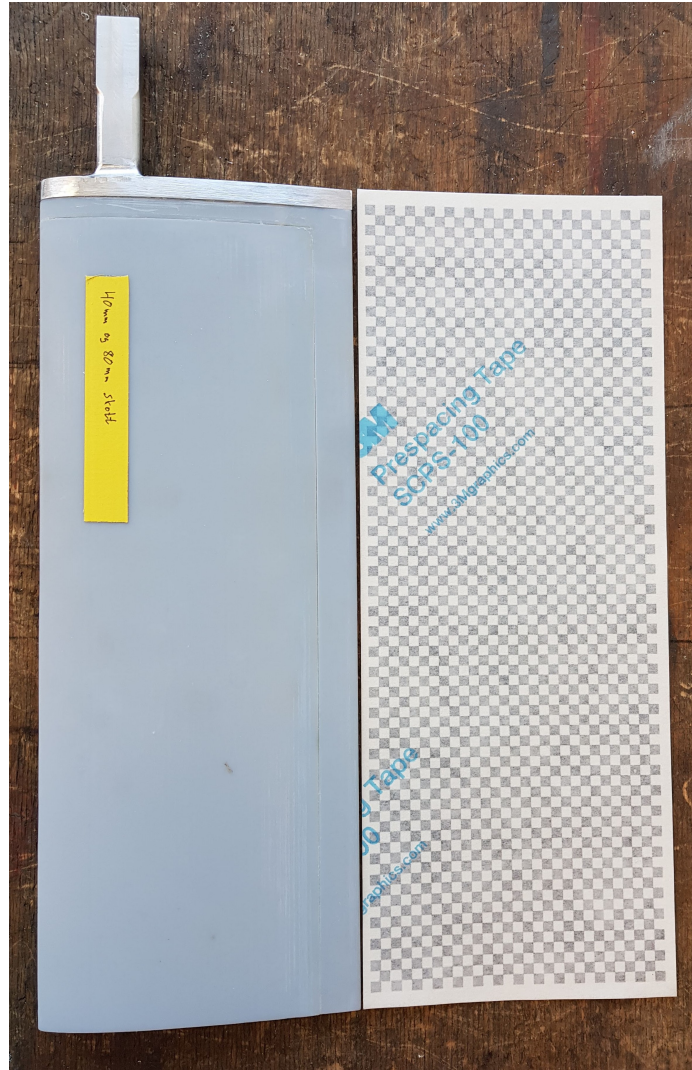


Figure 4.15: Left side is the soft foil with the shaft attached on the top side of the foil. On the right side the grid pattern before it was glued on the foil

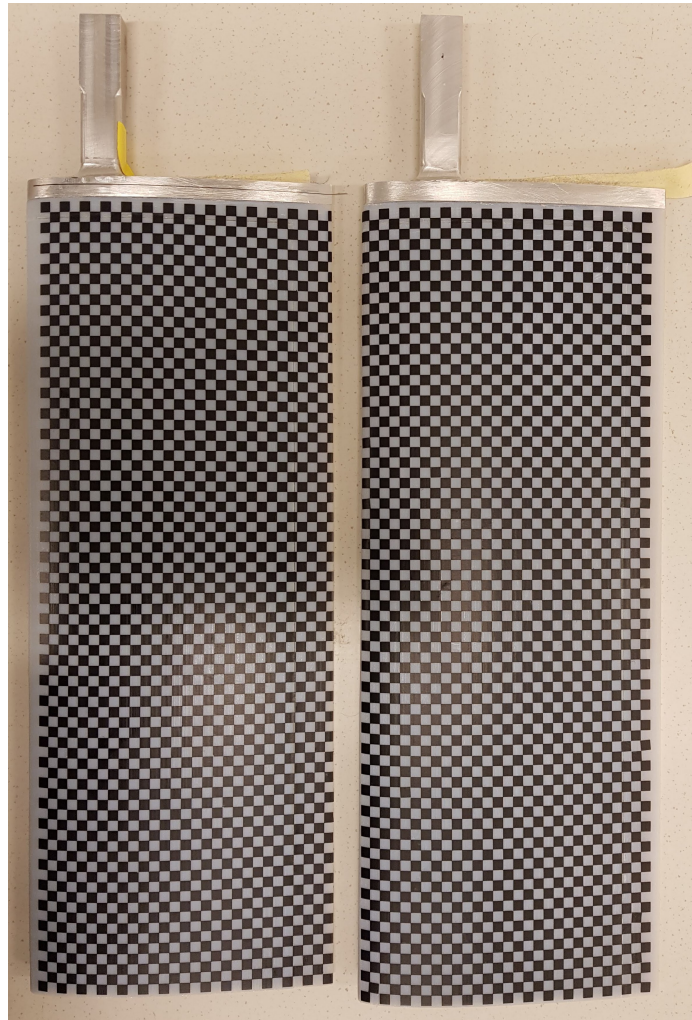


Figure 4.16: Both of the printed foils with grid pattern along the span and the shaft attached on the top of the foils.

5 Initial Testing

Calibration and boundary layer analyze was to be executed before the experiment on the foils could start. This section describes the process and the results obtained from the initial testing and calibration.

5.1 Calibration of Equipment

A calibration test on the force transducers was done before installing the rig in the test section. The calibration was done by tilting the rig and foil shaft horizontal and attach a calibration cross to the shaft. The cross was used to attach load (Figure 5.1). The calibration was done to ensure that it was not any damage to the force transducers. It was found that the calibration factor matrix that was used by John Martin Godø summer 2017, still could be used. The calibration was done for F_x , F_y and M_z . The calibration was done with four different weights, 1.0 N, 2.0 N, 5.0 N and 10.0 N for F_x and F_y . The weight was suspended at the middle of the cross to avoid torque in the shaft when measuring F_x and F_y . When measuring M_z the same calibration weight, as for F_x and F_y , was suspended at a distance of 0.1 m from the middle of the cross. The applied torque was then 0.1 Nm, 0.2 Nm, 0.5 Nm and 1 Nm.

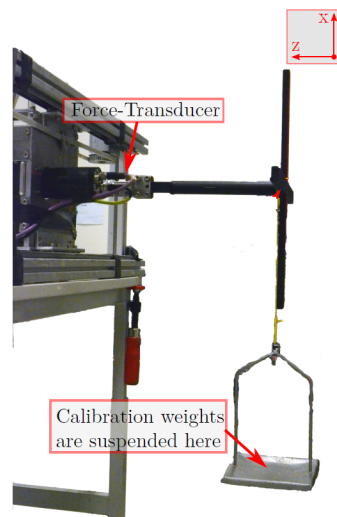


Figure 5.1: Calibration weights suspended on the calibration cross to test the force transducers. Courtesy of Lennard Bösch.

The forces measured corresponded with the applied load, with only an offset of 0.1 N for the largest load. Indication that the calibration factors obtained by John Martin Godø summer 2017 still are the same. With only an offset of 0.1 N, it was decided that the same calibration factors are used in this thesis.

5.2 Angle of Attack Range

This section presents the calculations done to find the maximum induced angle of attack (AoA) to use in the experiment and the corresponding frequencies. The frequency of motion affects the AoA, according to Hoover's Equation (Equation 21). By use of Hoover's Equation, the AoA is presented versus the frequency of motion f_m . Maximum AoA tested by Bosch and Anderson was $\alpha_{max} \approx 45$ degrees. According to Hoover's equation and the plot in Figure 5.2, this implies a maximum frequency of motion of ≈ 1.6 Hz. Due to the limitation in the rig setup, the maximum frequency possible is 0.95 Hz. In Figure 5.2 the yaw amplitude is 10° . To obtain lower α_{max} the yaw amplitude is increased for some of the runs ($\theta = 10^\circ, 20^\circ, 25^\circ, 26^\circ$). The inflow velocity, U_{inf} , is also tuned to modify the α_{max} . The water velocity will affect the range of the Strouhal number, St , according to Equation 7.

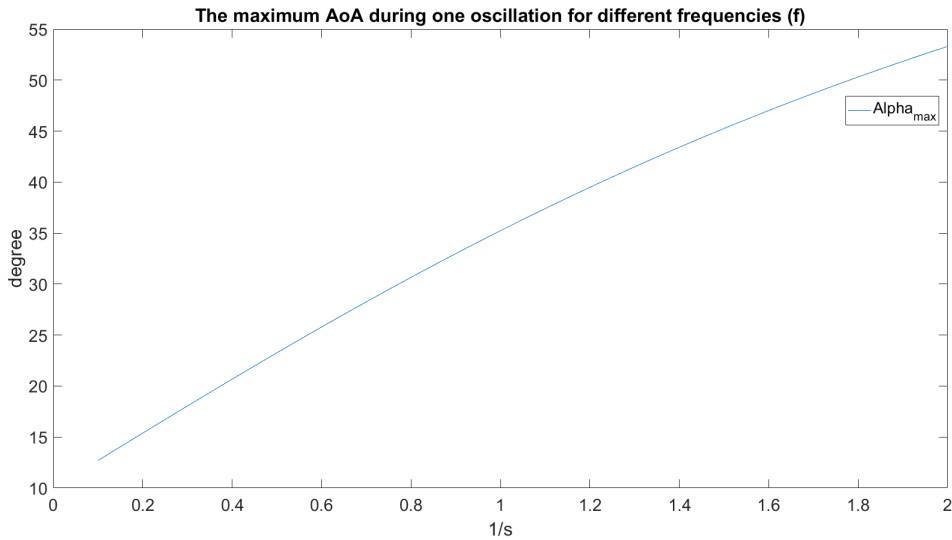


Figure 5.2: Maximum AoA, α_{max} , versus the frequency of motion, f_m , in the "foil rig". $\theta = 10^\circ$.

5.2.1 Overload

During a test on one of the flexible foils, the foil broke as a consequence of the large lift force, L , and mending moment, M_z . The foil was running at the maximum frequency of motion ($f_m = 0.95$ Hz), and it was noticed that the harmonic sinus motion was out of phase. This might lead to larger loads and contribute to the breaking of the foil. Due to time limitation, the foil was not repaired. Results from two foils will be presented, the stiff foil and one flexible foil.



Figure 5.3: Picture of the foil that broke during testing at $f_m = 0.95$ Hz. It broke at the glued part. It is possible that the glue was not strong enough to sustain the bending moment close to the fixed end

5.3 Decay Test

This section presents the results of the decay test. The decay test was conducted on both the stiff and flexible foil, in water and air. The plot of the decay test is presented as a time series. Power spectral density (PSD) was used to find the natural frequency, f_n , from the decay tests.

During the testing of the equipment in the test section, some vibration was observed in the measurements. This vibration can come from vibration in the test rig and vibration of the foil. The vibration in the test rig must be filtered out in the post-processing. The vibration on the foil can come from eigenmode load due to loads with a frequency close to the natural frequencies. The natural frequency was found by conducting a decay test in still water. In the decay test, the foil was hit with a soft hammer in both x- and y-direction. The respective forces F_x and F_y was measured as a time series. The power spectrum of the time series was created with Fast Fourier transformation. The peak in the power spectrum indicates the natural frequency, f_n .

5.3.1 Decay of stiff foil submerged in water

The time series from the response of the decay hammer test for the stiff foil submerged in water is given in Figure 5.4 and 5.5. The same time series was used to find the natural frequency of foils. Natural frequency was obtained by taking the PSD of the time series in Figure 5.4 and 5.5. It was noticed that the largest energy for the stiff foil in water is for a frequency of 22.60 Hz and 16.67 Hz. Indicating that the natural frequency for x- and y-direction are $f_{nx} = 22.60$ Hz and $f_{ny} = 16.67$ Hz, respectively. The PSD from the time series was started 0.1 s before the hammer hit the foil and was stopped when the response of the forces got close to zero.

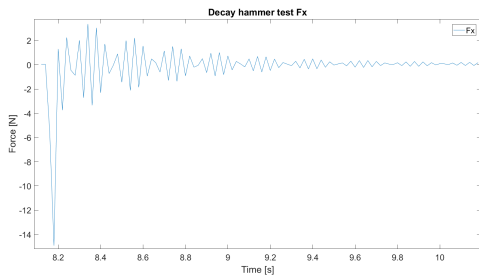


Figure 5.4: Decay hammer test in x-direction. Plot of the force F_x and the decay of the force for the stiff foil in water.

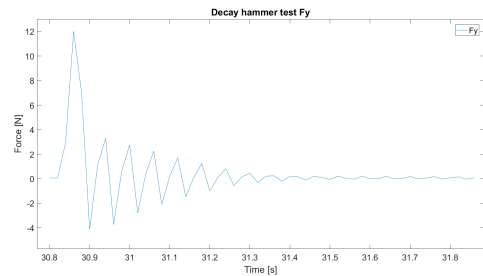


Figure 5.5: Decay hammer test in y-direction. Plot of the force F_y and the decay of the force for the stiff foil in water.

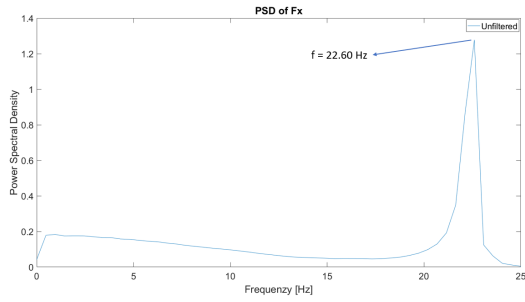


Figure 5.6: PSD of the decay hammer test in x-direction. Natural frequency in x-direction for stiff foil is $f_n = 22.60$ Hz.

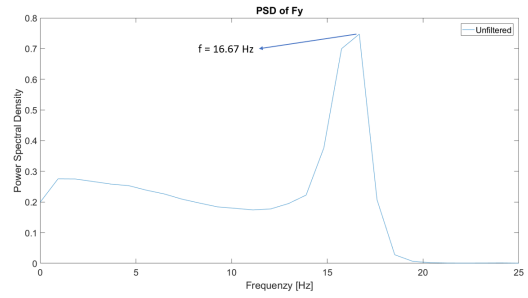


Figure 5.7: PSD of the decay hammer test in y-direction. Natural frequency in y-direction for stiff foil is $f_n = 16.67$ Hz.

5.3.2 Decay of stiff foil in air

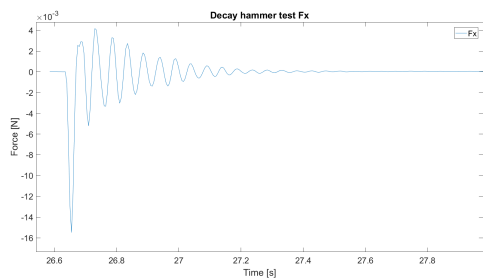


Figure 5.8: Decay hammer test in x-direction. Plot of the force F_x and the decay of the force for the stiff foil in air.

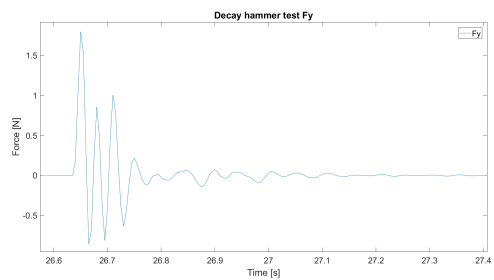


Figure 5.9: Decay hammer test in y-direction. Plot of the force F_y and the decay of the force for the stiff foil in air.

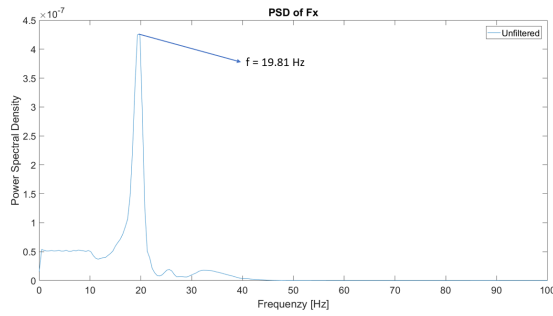


Figure 5.10: PSD of the decay hammer test with stiff foil in air for x-direction. Natural frequency in x-direction for stiff foil is $f_n = 19.81$ Hz.

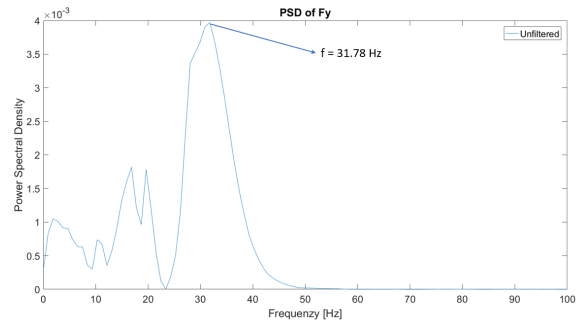


Figure 5.11: PSD of the decay hammer test with stiff foil in air for y-direction. Natural frequency in y-direction for stiff foil is $f_n = 31.78$ Hz.

5.3.3 Decay of flexible foil submerged in water

The same decay tests were conducted for the flexible foil. The decay test was done both in air and submerged in water. The time series of the response for the decay of the flexible foil in water is presented in Figure 5.12 and 5.13. At the decay test for F_y , it is noticed that the plot of the decay not only consist of one dominating decay frequency but two decay frequencies. This is also noticed in the PSD from the same time series (Figure 5.15). The PSD for the y-direction the power spectrum do not have the same clear peak as the power spectrum in the x-direction. Indicating that energy is absorbed in more than one frequency. The largest peak is at $f = 4.90$ Hz, but also a large peak at $f = 35.29$. The natural frequency is assumed to be at the largest peak, $f_n = 4.90$ Hz. This is a significant difference from the natural frequency of the stiff foil ($f_n = 16.67$ Hz).

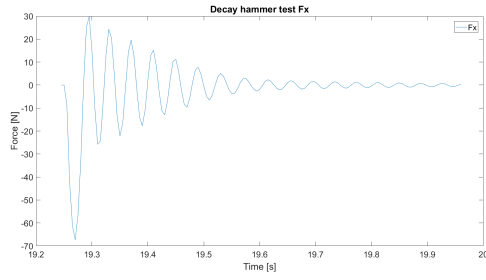


Figure 5.12: Decay hammer test in x-direction. Plot of the force F_x and the decay of the force for the flexible foil in water.

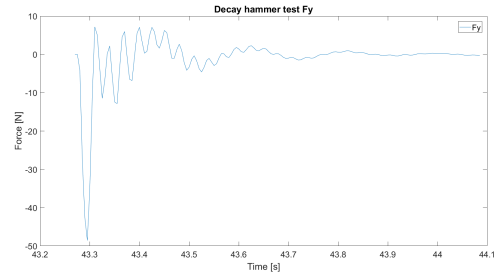


Figure 5.13: Decay hammer test in y-direction. Plot of the force F_y and the decay of the force for the flexible foil in water.

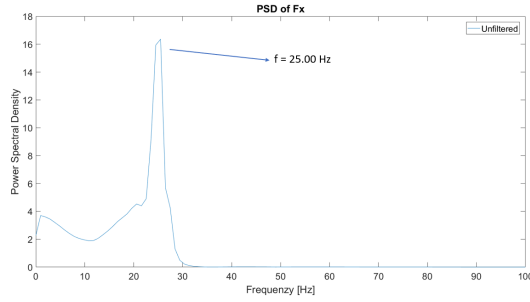


Figure 5.14: PSD of the decay hammer test with flexible foil submerged in water for x-direction. Natural frequency in x-direction for flexible foil is $f_n = 25.00$ Hz.

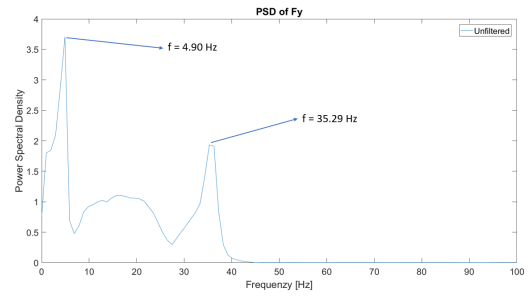


Figure 5.15: PSD of the decay hammer test with flexible foil submerged in water for y-direction. Natural frequency in y-direction for flexible foil is $f_n = 4.90$ Hz.

5.3.4 Decay of flexible foil in air

The last decay was done for the flexible foils in air. The foil was attached to the rig in the same way as the decay test in water, but the foil was "dry" (not submerged in water). The f_n of the flexible foil in the air is close to the f_n of the stiff foil in water. This is understood by the added mass. Natural frequency for the flexible foil in the air is 27.78 Hz and 18.29 Hz in the x- and y-direction, respectively. The stiff foil has f_n of 22.60 Hz and 16.67 Hz in x- and y-direction, respectively.

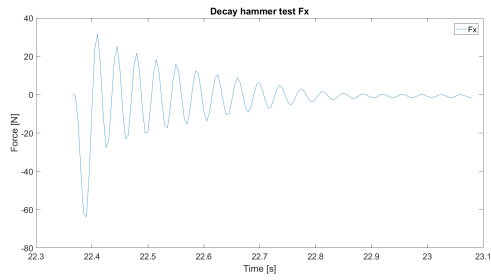


Figure 5.16: Decay hammer test in x-direction. Plot of the force F_x and the decay of the force for the flexible foil in air.

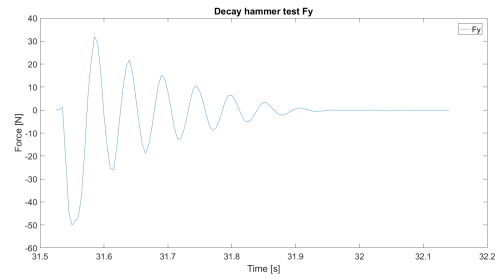


Figure 5.17: Decay hammer test in y-direction. Plot of the force F_y and the decay of the force for the flexible foil in air.

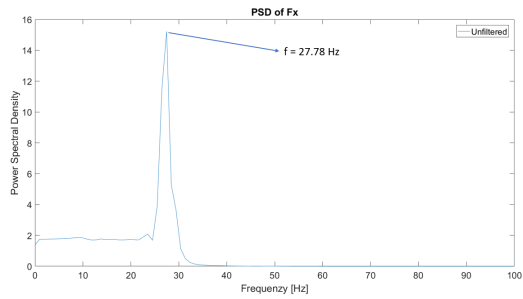


Figure 5.18: Power Spectral density of the decay hammer test with flexible foil submerged in air for x-direction. Natural frequency in x-direction for flexible foil is $f_n = 25.00$ Hz.

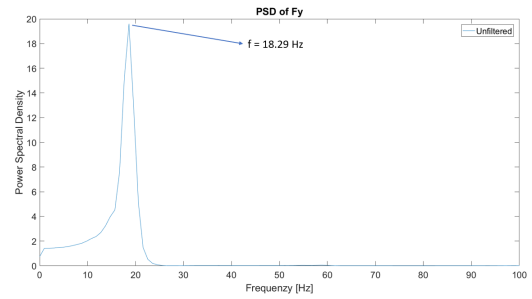


Figure 5.19: Power Spectral density of the decay hammer test with flexible foil submerged in air for y-direction. Natural frequency in y-direction for flexible foil is $f_n = 4.90$ Hz.

5.3.5 Results of Decay Tests

The natural frequency's is summarized in Table 6:

	f_{n_x} [Hz]	f_{n_y} [Hz]
Submerged		
Flexible	25.00	4.90
Stiff	22.60	16.67
Air		
Flexible	27.78	18.29
Stiff	19.81	31.78

Table 6: Natural frequency f_n from the decay test conducted both in air and submerged in water for the stiff and flexible foil.

5.4 Boundary Layer

This section presents the results regarding the boundary layer (BL) measurement done in the test section of CWT.

Measurement of the BL was done with a Laser Doppler Velocimetry (LDV) for the cross-section (y-z-plane) in the test section of CWT. The measurement was done with 29 and 20 points in y- and z-direction, respectively. The BL at the left side of the test section is illustrated in Figure 5.20. The coordinates in the graph are the coordinates of the LDV laser. The extra bottom (Figure 3.2) is at $z = 50$ mm and the tank top is at $z = 450$ mm. The left side of the wall in the test section (closer to the laser) starts at $y = 20$. The graph is only on the left side due to some problems in the measurements on the right side of the tank. The BL is assumed to be the same for both sides. The foil is placed in the middle of the test section. Relative to the coordinate system of the LDV, the foil has a mean sway position at 305 mm (zero sway). The largest sway amplitude is $y_{sway} = 75$ mm. With this amplitude, the foil will move to a minimum of $y = 230$ mm. BL on the left side ends at $y = 60$ mm. The foil will never come in contact with the BL. The same BL is assumed on the right side of the test section, and BL-effects are assumed to be minimum.

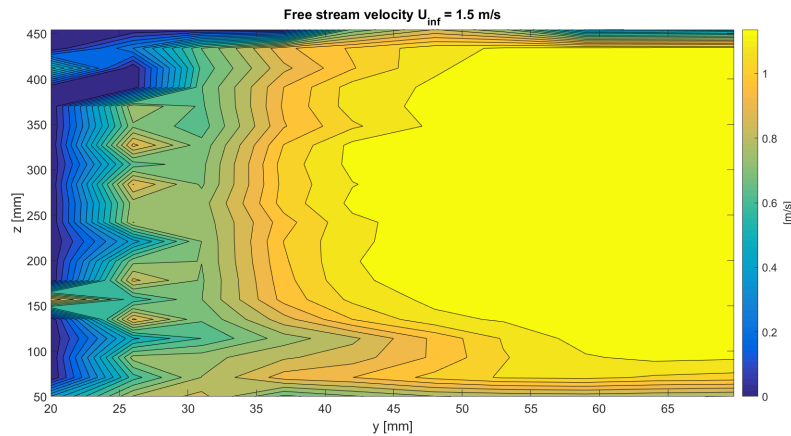


Figure 5.20: Plot of the boundary layer of the left side in the test section, with free stream velocity $U_{inf} = 1.0$ m/s. The measurements were done with LDV. All measurements were done 5.0 mm before the leading edge of the foil.

5.5 Frequency Range

This section discusses the limitation in the experimental setup regarding the frequency of motion.

Initially, it was decided that the foils were to be tested in the frequency range from 0.3 Hz to 0.95 Hz. The maximum frequency possible in the foil rig program made by Torgeir Wahl is 0.95 Hz. It was noticed that when the frequency increased above a certain frequency the engines on the rig were not able to keep large enough sway or yaw velocity, and the phase delay of 90 degrees was not maintained. As illustrated in Figure [5.21](#), the rig did not manage to keep large enough sway velocity for a motion of frequency of 0.95 Hz. For this frequency of motion, the maximum sway amplitude was smaller than 0.075 m. This might be due to large lift forces on the foil at this condition. The electrical engines are not strong enough to overcome the load. Another reason can be that the sway velocity needed to maintain a motion frequency of 0.95 Hz was too high for the sway engine. At 0.95 Hz the motion of the foil stabilized itself with 180° phase delay of the yaw angle, θ_{yaw} . With a phase delay on 180° and the maximum sway amplitude of ≈ 0.050 m, the results from motion frequency above 0.8 Hz was not comparable with the lower frequencies and is not presented in the result section. The same problem was noticed with the yaw velocity for a large yaw angle ($\theta > 15^\circ$). For $\theta > 15^\circ$ maximum $f_m = 0.8$ Hz, at $\theta > 25^\circ$ the maximum $f_m < 0.60$ Hz. If f_m is larger, the harmonic sinus motion will be out of phase. The limitation in the experimental setup will affect the St range possible to test (Equation [7](#))

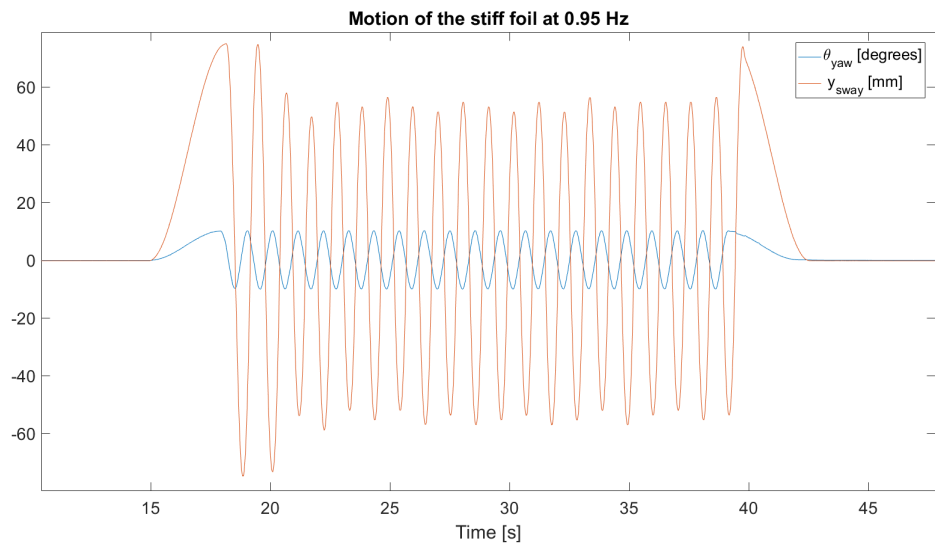


Figure 5.21: Plot of the motion for the stiff foil at motion of frequency of 0.95 Hz.

5.6 Bias errors

Bias errors are systematic errors when performing experiments with and without repeated runs. They can be difficult to quantify, because the information about the errors can be hard to find. It was noticed some bias errors when performing experiment in CWT. They are listed below:

- The water temperature was measured during testing. The tests were conducted within some weeks. The temperature in the room was not constant during this time. The water temperature is somewhat the same as the air temperature in the room. The temperature oscillated between 19 and 23 degrees. The kinematic viscosity ν is highly dependent on the temperature. For water temperature of 19 and 23 degrees ν varies from $\nu_{19} = 1.027 * 10^{-6} m^2/s$ to $\nu_{23} = 0.933 * 10^{-6} m^2/s$ [9]. The change in ν will affect Re_c and can also affect the flow around the foil.
- When performing decay test a calibration hammer was used to create vibration in the foil by slamming the calibration hammer on the foil in x- and y-direction (inline and cross flow direction). The slamming was done by hand and some lack of directional precision must be assumed. A result of this is interaction between the eigenmodes in x- and y-direction, creating a 8-shaped oscillation pattern during decay test. This might affect the result of the decay test.
- Wall effects during the circulation of water in the tank might affect the flow in the test section. In CWT the water goes through filter before entering the test section. The purpose of the filters is to keep the turbulence level of the flow in the test section low. However, some turbulence in the test section must be assumed.
- The boundary layer in the test section might affect the flow around the foil. The maximum BL from Figure 5.20 is 25 mm. This is not inside the sway amplitude of the foil. Never or less this might have some effect on the foil.

Other errors that were noticed were the offset of forces in the calibration of the force transducers. Calibration was conducted before installing the rig in the test section. The calibration was done on F_x , F_y and M_z . The calibration was done with four

different weights. The force transducers measured a load, with only an offset of 0.1 N for the largest load tested. This is only 2 % offset and indicate that the matrix calibration done by John Martin Godø summer 2017 still was sufficient. The same calibration matrix was used in this thesis, but with an offset of 2 %.

Some lag in the movement of the foil was noticed. Not a perfectly harmonic motion in sway and yaw

6 Results and Discussion

This section present and discuss the results obtained during the experiments on three different hydrofoils in the CWT laboratory in spring 2019. An effort is made to evaluate and compared C_L , C_T , C_M , C_P and η_p for the two foils tested. A repetition of Read's experiments from 2003 was done to calibrate the experimental setup and to verify the calculation in the post-processing. Some of the results are compared with the study conducted by Anderson in 1998 [3], Read in 2003 [29] and the master thesis of Bösch in 2015 [7].

The different runs are referred to as the maximum AoA obtained during a run (α_{max}). Test was done for $\alpha_{max} = 15^\circ, 22.5^\circ, 30^\circ, 41^\circ$ and 44° . The flapping frequency is presented as the non-dimensional Strouhal number, St , and is in the range of $St = 0.20 - 0.65$. The minimum and maximum inflow velocity, U_{inf} , is 0.15 m/s and 0.35 m/s. This give Reynolds number in the range of $Re = 22500 - 52500$.

Larger versions of the graph used in this section and other graphs that are not included in this section are found in APPENDIX A.

Some trouble occurred in the calibration and post-processing of the picture, regarding the optical measurement. Due to time limitation in the test facilities, and the damage on one of the flexible foils, the experiment could not be redone with the optical measurement. Because of this, the result from the optical measurement is not included in this section.

Benchmark for the comparison of the results with earlier experiments:

The choice of some of the parameters used by Anderson, Read and Bösch is different from this thesis. Figure 6.1 summarize the different parameters. The experiments done by Bosch were done with a thicker foil, which had a thickness of 15% of the cord length NACA0015. In this thesis, the thickness is 12% of the cord, NACA0012. Same used by Anderson and Read. In this thesis, the axis of yaw rotation is placed at $0.25c$, same as Bosch, but different from Anderson and Read. Anderson and Read

placed the yaw axis at $0.30c$. In this thesis the yaw angle θ is $10^\circ, 20^\circ, 25^\circ$ and 26° . Read used $\theta = 0^\circ, 7^\circ, 15^\circ$, and 30° . This makes the numerical α_{max} deviate some in the results. When comparing the thrust and thrust efficient $\theta = 15^\circ$ is used from Read's results.

Translation motion in heave was denoted h_0 by Anderson and Read [3] [29]. They referred to the amplitude of motion as the fraction between h_0 and c : $\frac{h_0}{c} = 0.75$. In this thesis, the sway motion is used in translation, y_{sway}^{amp} . The motion correspond to $\frac{y_{sway}^{amp}}{c} = 0.5$. The amplitude of motion is larger relative to the chord for Anderson's and Read's study. The choice of parameters in this study was due to space limitation in the test facilities, and the advice from Snekvik concerning the printing of the flexible foils.

	Anderson (1998)		
	Read (2003)	Bösch (2017)	Skogen (2019)
t_{max}	NACA0012	NACA0015	NACA0012
Yaw rot axis	0.30c	0.25c	0.25c
θ_{yaw}	$\theta = 30^\circ$	$\theta = 30^\circ$	$\theta = 10^\circ, 20^\circ, 25^\circ, 26^\circ$
$\frac{h_0}{c} = \frac{y_{sway}}{c}$	0.75	0.75	0.50

Figure 6.1: Comparison between the different parameters used in the experiment by Anderson [3], Read [29], Bösch [7] and this thesis (Skogen).

6.1 Static Lift, Drag and Moment

This section describes the lift- and drag coefficient for the static test.

The static analyze was conducted by stepping from zero AoA to a maximum of 30° AoA, and it was also done for negative AoA. This method will step the foils in and out of the stall. The foil is held at a steady yaw angle for 15 s where the mean lift and drag is measured. This was done from 0° up to a maximum of 20° and 30°, for the flexible and stiff foil respectively. Because of the risk of breaking the flexible foil, 20° was used. In the sequence, an increment of 1° close to the stall angle and 5° increment outside stall was used. Both the stiff and flexible foil was tested at two different Re .

In Figure [6.2](#) the lift is linear inside $-10^\circ < \alpha < 10^\circ$ for $Re = 45\ 000$. For the same range of α at $Re = 150\ 000$ C_L is not perfectly linear for negative AoA. For the stiff foil stall occur at -10° for negative lift and 13° for the positive lift at $Re = 45\ 000$, indicating some asymmetry in the lift curve for the stiff foil. The same stall angles are not noticed for the stiff foil at $Re = 150\ 000$. For $Re = 150\ 000$ stall occur at -12° and 15° for the negative and positive lift, respectively.

At $Re = 45\ 000$, some delay in the stall is noticed for the flexible foil, relative to the stiff foil. Stall at the positive lift for the flexible foil occurs at 14° . Compared to 13° for stiff foil. This delay in the stall is not present for a lower Re . This might be due to the lower lift force at a lower Re . At $Re = 45000$ the forces on the flexible foil is not large enough to deform the foil. At $Re = 150000$ the forces are still not large enough to deform the flexible foil, making it twist to a lower AoA. In other words, the static lift for the flexible foil is not smaller than the static lift of the stiff foil. This was the aim of the design and the placement of the spars inside the cross-section, to make the flexible foil twist to a lower AoA when the loads got higher. At negative lift both the flexible and stiff foil stall at 10° . Some asymmetry is also noticed for the flexible foil. The asymmetry might indicate an offset of the angle in the experimental setup. At $Re = 150\ 000$ stall occur at higher α than for $Re = 45\ 000$. For positive lift stall occur at the same AoA ($\alpha = 15^\circ$). For negative lift stall occur later for stiff

foil, $\alpha = 13^\circ$ and $\alpha = 10^\circ$ for stiff and flexible foil, respectively. It is noticed that stall, in general, occur at a higher α for higher Re

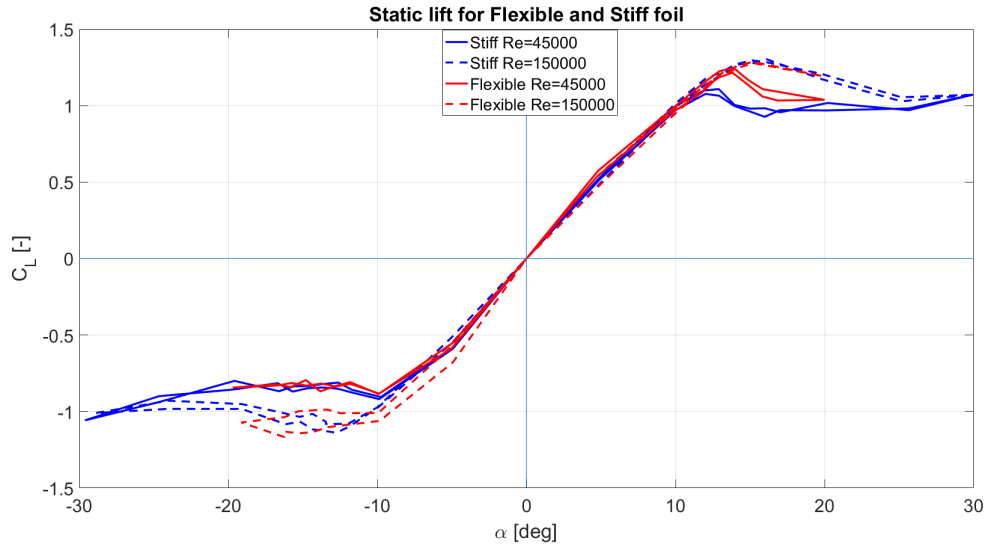


Figure 6.2: Lift coefficient C_L for the static test versus the angle of attack α . $\alpha_{max} = 30^\circ$ for the stiff foil and $\alpha_{max} = 20^\circ$ for the flexible foil

In Figure 6.3 some asymmetry for the stiff foil is noticed, and the deviation between stiff and flexible foil is small. At $\alpha_{max} = 20^\circ$ and for $Re = 150000$ the drag coefficient for stiff foil at positive and negative α is 0.45 and 0.40, respectively. For the flexible foil C_D is the same for both sides ($C_D = 0.41$). The rapid increase in drag is noticed for same α as for the stall of the lift. At $Re = 45000$ the drag is more symmetric with the same extreme values.

In Figure 6.4 the moment coefficient, C_M , is illustrated. Before stall C_M is negative for $\alpha_{max} > 0$. When stall occur ($\alpha_{max} \approx 14^\circ$) the moment change sign and a increase in absolute value is noticed. At $\alpha_{max} > 0$ the stall seems to occur for higher α_{max} , compared to negative angles. At higher Re the stall occur for higher α_{max} as discussed for C_L .

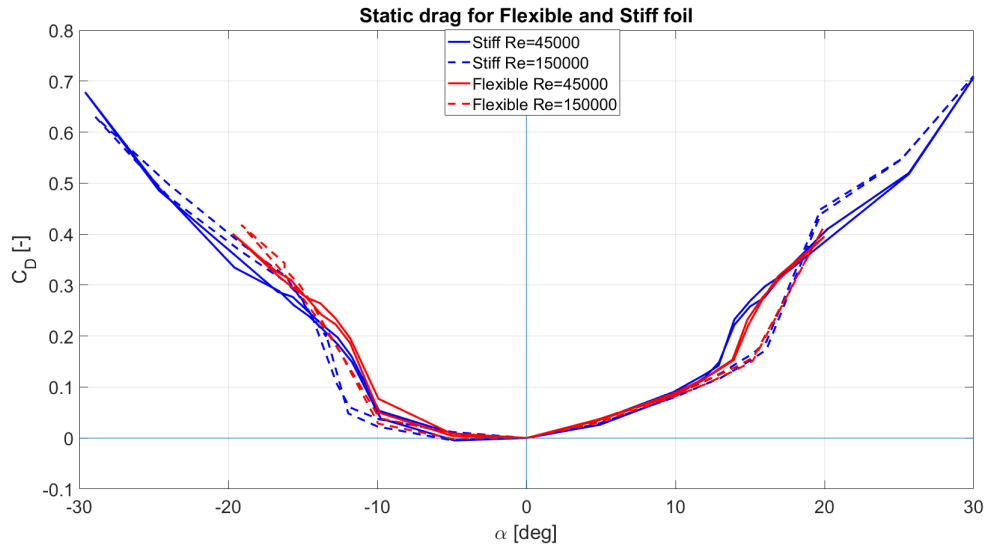


Figure 6.3: Drag coefficient C_D for the static test versus the angle of attack α . $\alpha_{max} = 30^\circ$ for the stiff foil and $\alpha_{max} = 20^\circ$ for the flexible foil

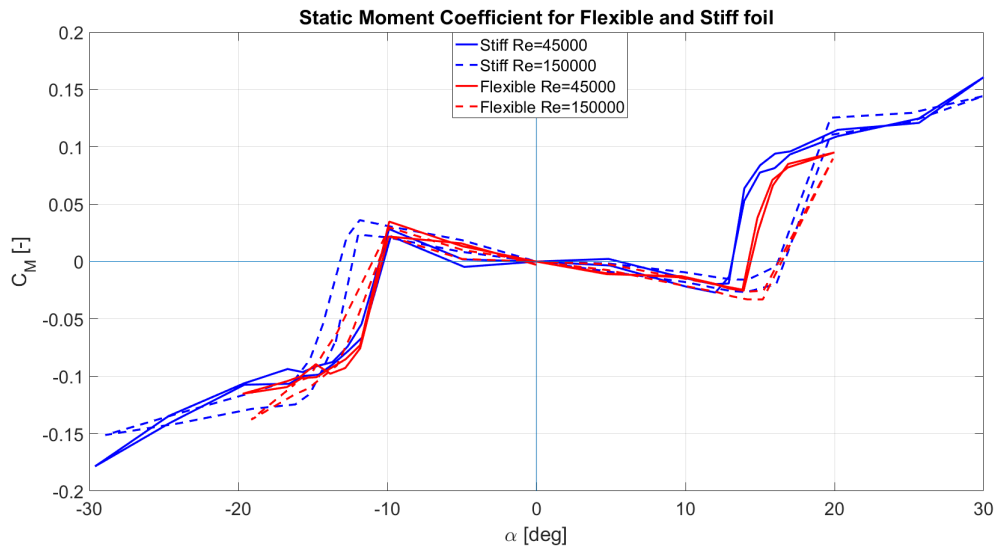


Figure 6.4: Moment coefficient C_M for the static test versus the angle of attack α . $\alpha_{max} = 30^\circ$ for the stiff foil and $\alpha_{max} = 20^\circ$ for the flexible foil

6.2 Repetition of Read's experiments

In this section the repetition of Read's experiments is presented. The repetition of Read's experiments was done to calibrate the setup and the post processing. Read used a 90° phase angle, ϕ . He did not comment on any deflection of the foil during hydrodynamic loading, it is assumed he used a stiff foil. The repetition of Read's study was done with $\alpha_{max} = 22.5^\circ$. In Figure 6.5 good agreement for the propulsion efficiency, η_p , was noticed for the flexible foil with $\phi = 90^\circ$ with the range: $St = 0.23 - 0.35$. At $\phi = 90^\circ$ the stiff foil has lower efficiency than both Read and the flexible foil. It is noticed that the highest efficiency ($\eta_p = 0.52$) is obtained with the flexible foil. The highest efficiency obtained by Read is $\eta_p = 0.51$ [29]. In general the flexible foil has higher η_p for $\alpha_{max} = 22.5^\circ$, compared to the stiff foil in the range of $St = 0.2 - 0.35$.

It is noticed a drop in the efficiency for both foils when $St \approx 0.35$. In Figure 6.6 this effect can also be seen in the thrust coefficient (C_T) when approaching $St = 0.35$. It is noticed a stagnation of C_T at $St > 0.30$ for both foils. The drop in η_p can be explained by the decrease in C_T . It is assumed an increase in C_T when St is increased. This assumption is strengthened by Read's results. The stagnation might be due to large velocity in sway and yaw. For some frequency of motion ($f > 0.55\text{Hz}$) it was noticed that the engines on the "foil rig" had trouble with large velocities and was not able to keep up the harmonic sinus motion ($St = 0.35 \rightarrow f = 0.58\text{ Hz}$). The velocity limit in the foil rig might be the reason of the stagnation.

Read obtained a larger C_T , regardless the phase. He argued that large motion-to-chord ratio, h/c , gave high C_T . In this thesis the motion-ratio is $y_{sway}/c = 0.5$. Read used $h/c = 0.75$. In general C_T is higher for the flexible foil, relative to the stiff foil. It is also noticed that $\phi = 90^\circ$ gives higher C_T than $\phi = 75^\circ$.

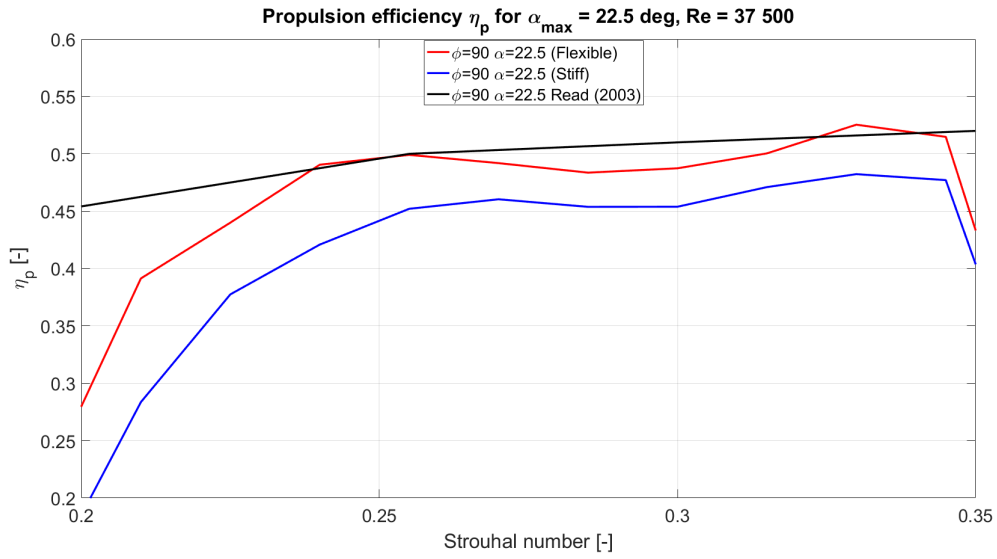


Figure 6.5: Propulsion efficient, η_p , for the same range of St and the same maximum AoA (α_{max}) as Read used in his study in 2003. The flexible and stiff foil was tested.

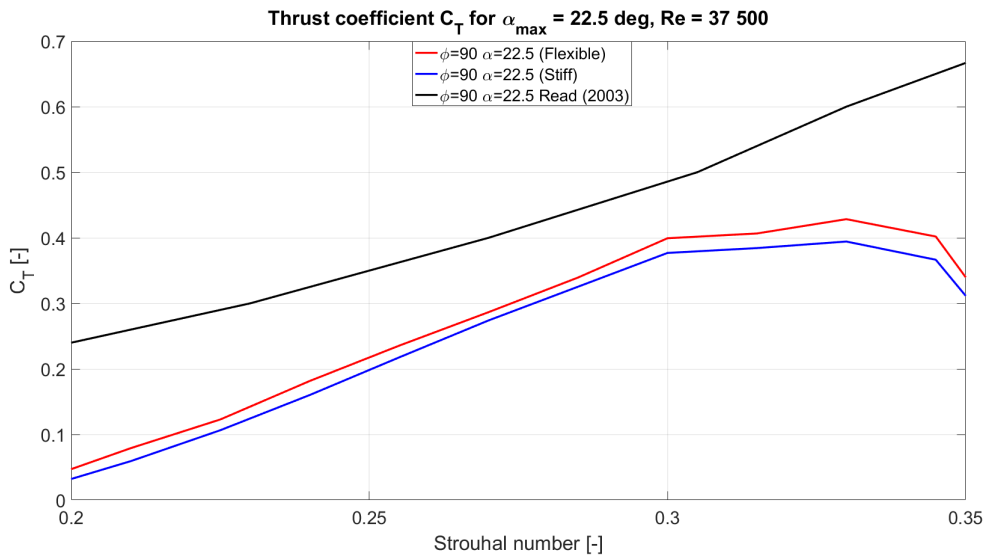


Figure 6.6: Thrust coefficient, C_T , for the same range of St and the same maximum AoA (α_{max}) as Read used in his study in 2003. The flexible and stiff foil was tested.

6.3 Result of the stiff and flexible foil

This section describes the results from the stiff and flexible foil tested in CWT at two different phases ($\phi = 90^\circ$ and $\phi = 75^\circ$). The result of C_T , C_P and η_p is presented and discussed. The forces during one oscillations is included and comment in the end of this section.

The parameters used in the different runs is listed in Table 7. For $\alpha_{max} = 15^\circ, 22.5^\circ, 30^\circ, 44^\circ$ the yaw angle, θ , is 20° . For $\alpha_{max} = 41^\circ$ θ is 10° . To describe the effect of θ , the feathering parameter (χ) is used. At maximum inflow velocity (U_{inf}) and maximum frequency of motion (f_m) χ is found by use of Equation 8 for all θ . It noticed that the lowest feathering parameter is for $\alpha_{max} = 41^\circ$.

α_{max}	15	22.5	30	41	44
θ	26	26	21	10	20
U_{inf}	0.35	0.25	0.25	0.30	0.15
Re	52500	37500	37500	45000	22500
y_{sway}	0.075	0.075	0.075	0.075	0.075
f_m	0.40	0.40	0.40	0.40	0.40
χ	0.92	0.70	0.57	0.31	0.39

Table 7: Table of the parameters used in the experiment

6.3.1 Thrust coefficient

This section is presenting the thrust coefficient, C_T , with respect to St . For $St < 0.2$ energy is absorbed by the system, thus result in this range is not included. The plots contain the two phases $\phi = 75^\circ$ and $\phi = 90^\circ$, and the two foils with different stiffness.

In Figure 6.7 some deviation in thrust between $\phi = 90^\circ$ and $\phi = 75^\circ$ is observed. The phase of $\phi = 90^\circ$ tends to produce more thrust than $\phi = 75^\circ$ for the same α_{max} in the range of $St = 0.20 - 0.32$. In Figure 6.8 the runs with the flexible foil is illustrated with two phases ($\phi = 75^\circ, \phi = 90^\circ$). The same tendency is observed. For some α_{max} the thrust coefficient (C_T) is larger for phase of 90° than for $\phi = 75^\circ$. Only

$\alpha_{max} = 41^\circ$ creates larger C_T for $\phi = 75^\circ$. Another aspect with the plot in Figure 6.8 is the increase in C_T for higher AoA. The highest recorded C_T is for $\alpha_{max} = 41^\circ$ and $\phi = 75^\circ$.

In Figure 6.9 the flexible and stiff foil is illustrated with the same phase ($\phi = 75^\circ$). Except for the case with $\alpha_{max} = 41^\circ$, the same tendency of higher C_T for higher α_{max} is observed. For all α_{max} the flexible foil (red) produce more thrust than the stiff foil (blue). The flexible foil with phase 90 is the case with highest C_T . The lowest recorded C_T is with stiff foil at $\phi = 75^\circ$. Higher thrust for flexible foil indicate somewhat higher lift force on the foil. The flexible and stiff foil has the same profile (NACA 0012) and the increase in thrust might be due to some increase in AoA for the flexible foil. The aim of the flexible foil was to twist to a lower AoA when the load was increased. The tendency is that the flexible foil has higher thrust and the twist to a higher AoA for the flexible foil might be the case.

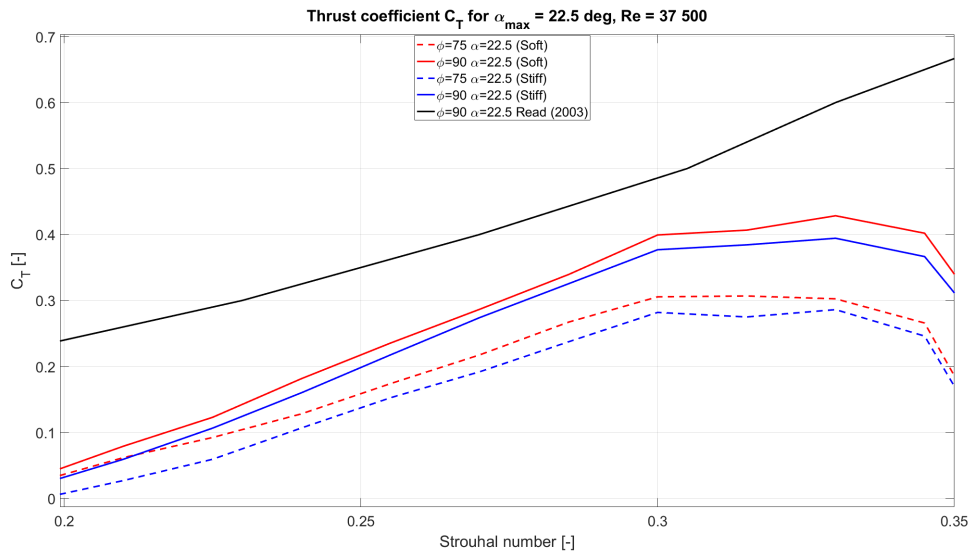


Figure 6.7: C_T at $\alpha_{max} = 22^\circ$ for stiff and flexible foil, at $\phi = 90^\circ$ and $\phi = 75^\circ$

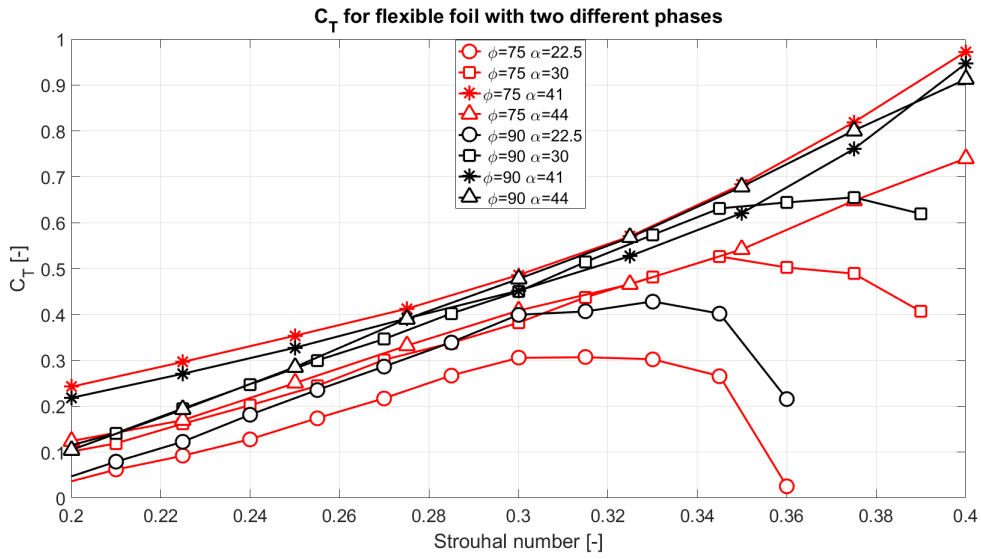


Figure 6.8: C_T for flexible foil with $\phi = 90^\circ$ and $\phi = 75^\circ$.

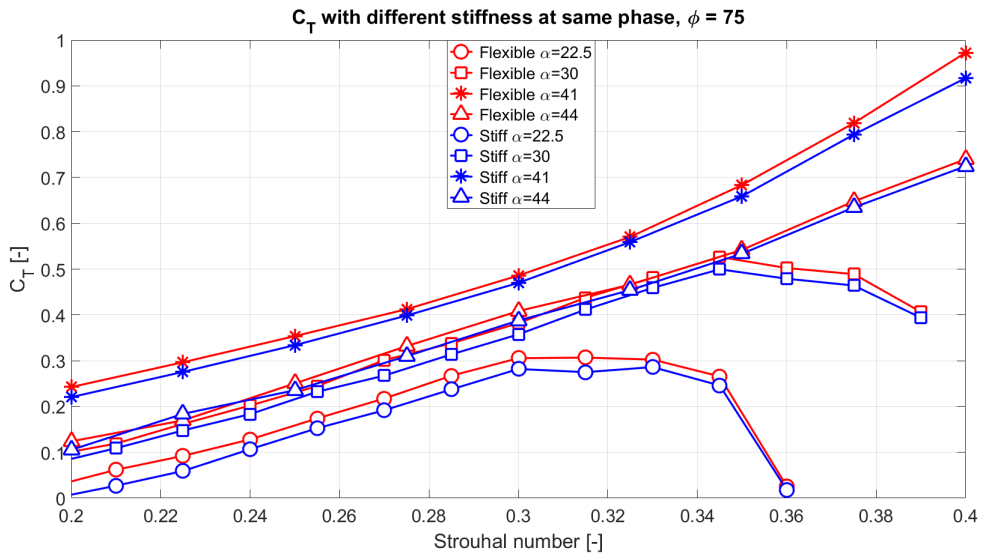


Figure 6.9: C_T for the stiff and the flexible foil with $\phi = 75^\circ$

6.3.2 Power Coefficient

This section is presenting the power coefficient, C_P , with respect to St . Recall that the power was obtained by use of Equation 27 and the values recorded over 18 peri-

ods. The power is the work done by the "foil rig" to create the motion in sway and yaw. The power depends on the moment around the z-axis of the foil, M_z , the lift force, L , and the sway and yaw velocities (\dot{y}_{sway} , $\dot{\theta}_{yaw}$).

In Figure 6.11 the energy used by the "foil rig" is presented as the power coefficient, C_P . The power coefficient depend highly on St . The increase in C_P is strongly dependent on $St > 0.30$. Higher St is equivalent with higher f_m . Large f_m has a significantly effect on \dot{y}_{sway} and $\dot{\theta}_{yaw}$. For high velocities the power is increasing.

The energy used during on oscillation is less for $\phi = 90^\circ$ if the yaw angle is small. In Figure 6.11 the yaw angle is small ($\theta_{yaw} = 10^\circ$). For $\theta_{yaw} = 10^\circ$ the phase of 75° is more energy consuming than $\phi = 90^\circ$. For $\theta_{yaw} = 20^\circ$ and $\theta_{yaw} = 26^\circ$ ($\alpha_{max} = 44^\circ$ and $\alpha_{max} = 30^\circ$) a phase of 90° is more energy consuming, relative to $\phi = 75^\circ$. In general the energy used to move the foil is the same regardless the stiffness of the foil.

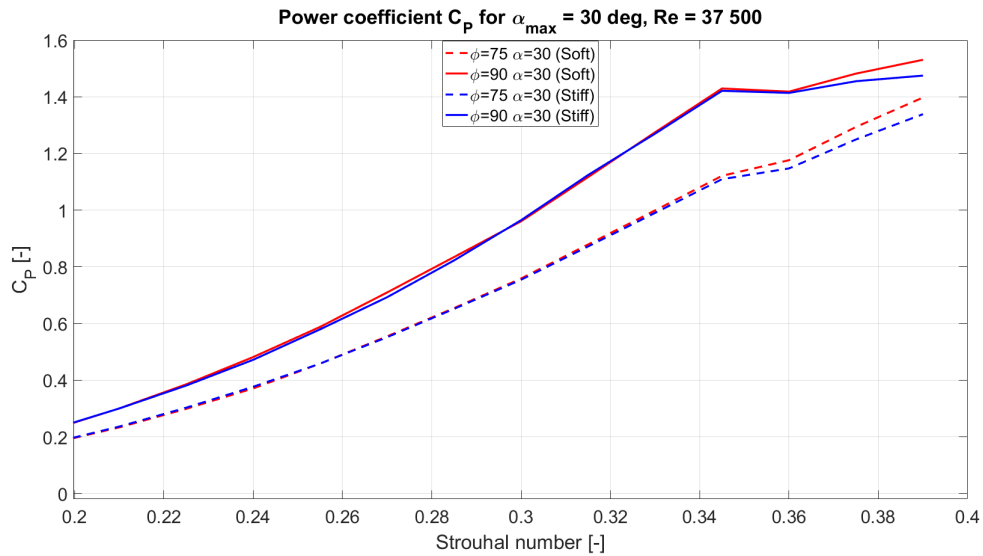


Figure 6.10: C_P versus St at $\alpha_{max} = 30^\circ$ and $\theta = 26^\circ$, for stiff and flexible foil, at $\phi = 90^\circ$ and $\phi = 75^\circ$

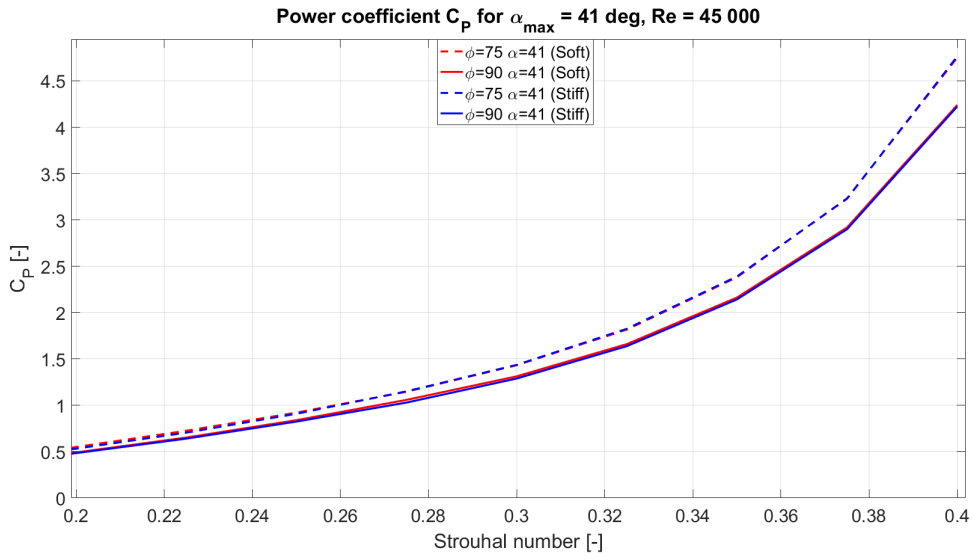


Figure 6.11: C_P versus St at $\alpha_{max} = 41^\circ$ and $\theta = 10^\circ$, for stiff and flexible foil, at $\phi = 90^\circ$ and $\phi = 75^\circ$

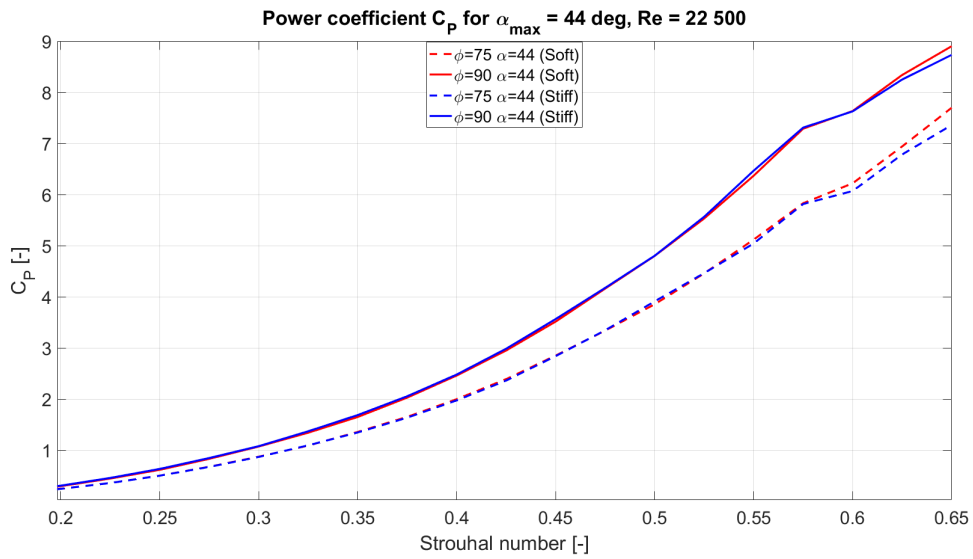


Figure 6.12: C_P versus St at $\alpha_{max} = 44^\circ$ and $\theta = 20^\circ$, for stiff and flexible foil, at $\phi = 90^\circ$ and $\phi = 75^\circ$

6.3.3 Propulsion Efficiency

This Section present and describes the propulsion efficiency and compare the results with the ideal efficiency, η_i .

The propulsion efficiency, η_p , is compared with the ideal efficiency, η_i . The ideal efficiency describes the maximum theoretical efficiency possible for a given load on the lifting surface. The ideal efficiency is larger than a physical propeller, but it illustrated the trend between the generated thrust and efficiency. In general low C_T will have a high η_i , and high C_T gives low η_i (Equation [38](#)). One possible application for the hydrofoil is to replace the propeller as the main propulsion device. To replace the propellers, the hydrofoil should have an efficiency close to the propeller used today, because of this the results for η_p is compared with η_i . It can also be mention that a common Wageningen B-series propeller has a maximum efficiency of $\approx 75\%$ for low C_T [21](#).

$$\eta_i = \frac{2}{1 + \sqrt{1 + C_T}} \quad (38)$$

In Figure [6.13](#) the propulsion efficiency versus $St = 0.10 - 0.40$ is illustrated. For low St the flexible foil has a higher η_p relative to the stiff foil, for higher St the stiff and flexible foil has the same η_p . For $St > 0.15$ the efficiency is decreasing. This is also the case for $\alpha_{max} = 44^\circ$, illustrated in Figure [6.14](#). The decrease in η_p might be due to the high α_{max} , inducing quite large C_P for $St > 0.20$ (Figure [6.11](#) and [6.12](#)).

According to Figure [6.18](#) the flexible foil have the highest η_p recorded in this study with $\eta_p = 0.561$. The highest efficiency is measured at $St = 0.285$ and $\alpha_{max} = 22.5^\circ$. Read noticed a plateau with efficiency of 0.50-0.60 in range of St .

It is a tendency that the flexible foil with $\phi = 75^\circ$ has the highest η_p . Figure [6.15](#) illustrates the plot of η_i and η_p for the flexible foil with $\phi = 75^\circ$ and $\alpha_{max} = 22.5^\circ, 30^\circ, 41^\circ$ and 44° . The same tendency is illustrated for a various range of St . The tests with lowest α_{max} (22.5° and 30°) is the motion with the highest η_p . $\alpha_{max} = 41^\circ$ is the motion with lowest efficiency for $St = 0.22 - 0.34$. The same motion has the highest C_P compared to the motions with $\alpha_{max} = 22.5^\circ, 30^\circ, 44^\circ$. $\alpha_{max} = 41^\circ$ is the only run

with $\theta = 10^\circ$. This might lead to large horizontal forces in cross flow direction, lift. Large lift will induce large amount of energy and the power will increase. The other motion, $\alpha_{max} = 22.5^\circ, 30^\circ, 44^\circ$, had higher yaw angle amplitude: $\theta_{yaw} = 26^\circ, 21^\circ, 2^\circ$, respectively.

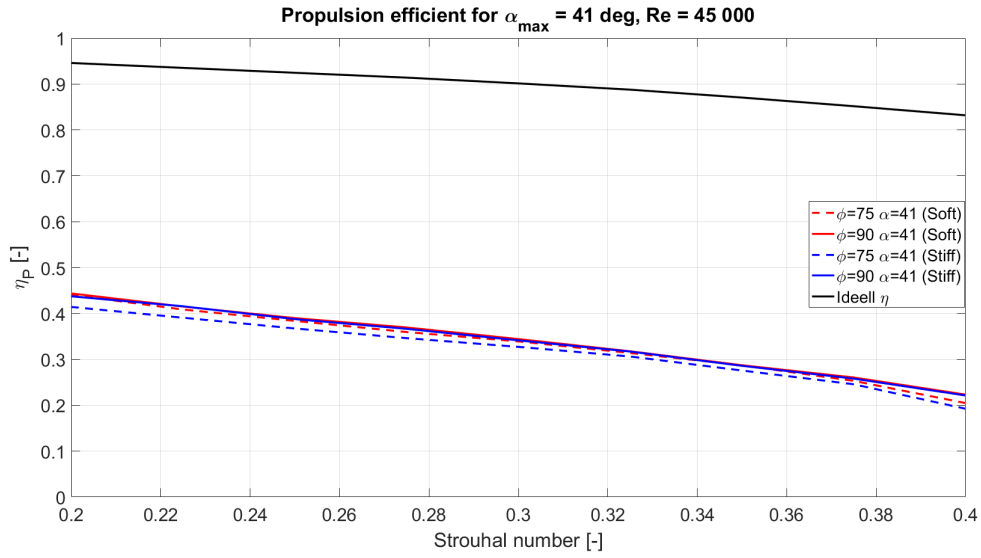


Figure 6.13: η_p versus St at $\alpha_{max} = 41^\circ$ and $\theta = 10^\circ$, for stiff and flexible foil, at $\phi = 90^\circ$ and $\phi = 75^\circ$

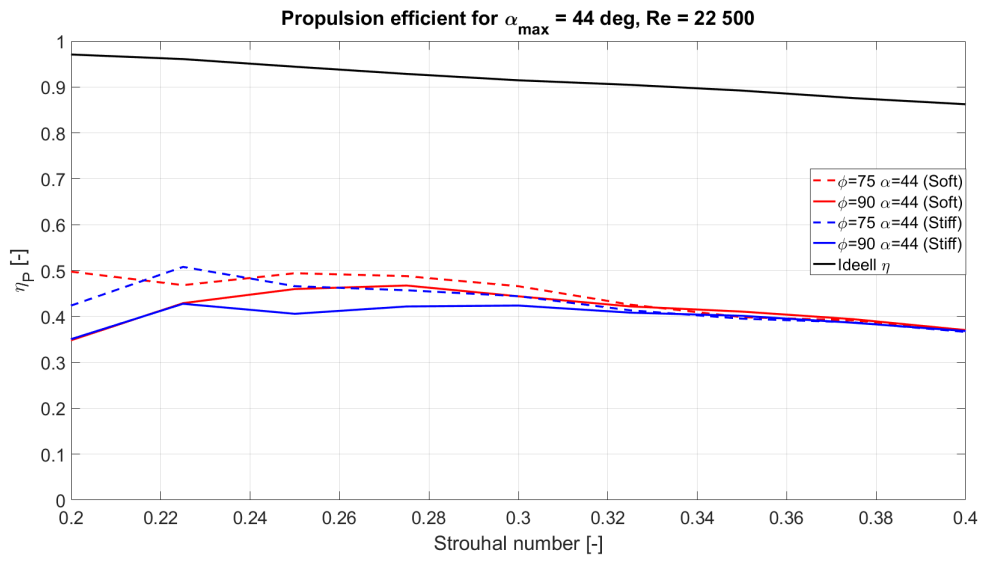


Figure 6.14: η_p versus St at $\alpha_{max} = 44^\circ$ and $\theta = 20^\circ$, for stiff and flexible foil, at $\phi = 90^\circ$ and $\phi = 75^\circ$

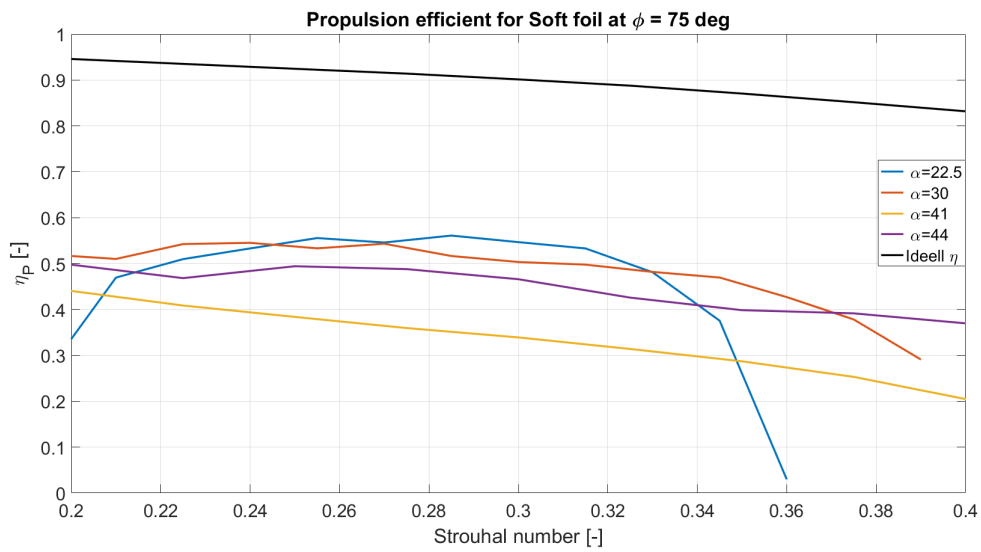


Figure 6.15: η_p versus St for flexible foil with $\phi = 75^\circ$

6.3.4 Local and Global Maximum

This section describes the maximum values recorded for each run for the different foils and phases. In Figure [6.16](#), [6.17](#) and [6.18](#) the maximum value for each run is presented for C_T , C_P and η_p . It is used colors to detect any trends in the results. For C_T and η_p green color is used as maximum and red is minimum. For C_P it is opposite, red is maximum and green is minimum. Notice that all the values presented in Figure [6.16](#), [6.17](#) and [6.18](#) is the maximum value from each respective runs.

In Figure [6.20](#) and [6.19](#) a bar plot illustrates the correlation between the maximum η_p or C_T . The top graph in Figure [6.20](#) and [6.19](#) is the maximum value from each run ($\eta_{p_{max}}$ and $C_{T_{max}}$). The bottom graph is the corresponding (same St and run) for C_T or η_p . This is described in Equation bellow:

$$\begin{aligned}\eta_{p_{max}}(St(i)) &= C_T(St(i)) \\ C_{T_{max}}(St(j)) &= \eta_p(St(j))\end{aligned}\tag{39}$$

In Figure [6.16](#) the largest C_T obtain in this study is with the flexible foil at $\phi = 75^\circ$ and $\alpha_{max} = 41^\circ$ ($C_T = 0.97$). This is only slightly above the maximum C_T for flexible foil at $\phi = 90^\circ$ and $\alpha_{max} = 41^\circ$. For all other α_{max} the flexible foil with $\phi = 90^\circ$ has the highest maximum C_T . Read (2003) recorded $C_T = 0.90$ at $\alpha_{max} = 35^\circ$. Read argued that large η_p was obtained for small α_{max} and low C_T . The highest recorded η_p is at $\alpha_{max} = 22.5^\circ$ for the flexible foil at $\phi = 75^\circ$ ($\eta_p = 0.56$). The corresponding C_T is 0.28, which is significantly smaller than maximum recorded thrust coefficient of 0.97 ($\alpha_{max} = 44^\circ$). Going the other way, a large C_T for $\alpha_{max} = 44^\circ$ give $\eta_p \approx 0.35$.

In Figure [6.17](#) the maximum C_P from each run is listed. The highest recorded C_P is for the stiff foil at $\phi = 75^\circ$ and $\alpha_{max} = 41^\circ$ ($C_P = 4.76$). It is noticed that every C_P at $\alpha_{max} = 41^\circ$ is higher than C_P for the other α_{max} . As discussed earlier $\alpha_{max} = 41^\circ$ is the only run with $\theta = 10^\circ$. A yaw angle of 10° generates the highest thrust (Figure [6.16](#)), but also consume the largest amount of energy, highest C_P .

What seems to be the α_{max} with the highest η_p , regardless the phase or stiffness

is 22.5° . This condition has quite good propulsion efficiency ($\eta_p = 0.48 - 0.56$) for all the runs (Figure 6.20). The corresponding C_T (for the maximum η_p) for $\alpha = 22.5^\circ$ is also quite good, specially for $\phi = 90^\circ$ (blue and yellow bars), with $C_T > 0.40$ (Bottom of Figure 6.20)

C_T	<i>Stiff</i>		<i>Flexible</i>	
	$\phi = 90$	$\phi = 75$	$\phi = 90$	$\phi = 75$
α				
15	0.0836	0.0490	0.0884	0.0585
22.5	0.3943	0.2861	0.4284	0.3068
30	0.6345	0.4995	0.6551	0.5265
41	0.9345	0.9168	0.9464	0.9724
44	0.9120	0.7245	0.9123	0.7399

Figure 6.16: The maximum C_T from each run of the two phases and two foils, for all the maximum AoA (α_{max}). The light green is the local maximum (largest maximum value for each α_{max}), green is global maximum value (largest maximum overall). Light red is local minimum (smallest maximum value for each α_{max}), red is global minimum in the table (smallest maximum for all the runs).

C_P	<i>Stiff</i>		<i>Flexible</i>	
	$\phi = 90$	$\phi = 75$	$\phi = 90$	$\phi = 75$
α				
15	0.2153	0.3192	0.2250	0.3490
22.5	0.8305	0.8210	0.8192	0.8726
30	1.4747	1.3386	1.5305	1.3973
41	4.2238	4.7639	4.2397	4.7510
44	2.4832	1.9780	2.4636	2.0010

Figure 6.17: The maximum C_P from each run of the two phases and two foils, for all the maximum AoA (α_{max}). The light green is the local minimum (smallest maximum value for each α_{max}), green is global minimum value (smallest maximum overall). Light red is local maximum (largest maximum value for each α_{max}), red is global maximum in the table (largest maximum for all the runs).

η_p	<i>Stiff</i>		<i>Flexible</i>	
	$\varphi = 90$	$\varphi = 75$	$\varphi = 90$	$\varphi = 75$
α				
15	0.4351	0.3644	0.4882	0.4484
22.5	0.4823	0.5035	0.5254	0.5610
30	0.4848	0.5064	0.5143	0.5452
41	0.4628	0.4429	0.4949	0.5173
44	0.4276	0.4901	0.4674	0.4976

Figure 6.18: The maximum η_p from each run of the two phases and two foils, for all the maximum AoA (α_{max}). The light green is the local maximum (largest maximum value for each α_{max}), green is global maximum value (largest maximum overall). Light red is local minimum (smallest maximum value for each α_{max}), red is global minimum in the table (smallest maximum for all the runs).

Figure 6.19 compare the maximum C_T with the corresponding η_p (same St) for all the runs. Figure 6.20 does the same, but the other way around, C_T at maximum η_p . The highest C_T is at $\alpha_{max} = 41^\circ$ ($C_T \approx 0.9$), the corresponding η_p is quite low ($\eta_p < 0.25$). The highest η_p for maximum C_T is noticed at $\alpha_{max} = 22.5^\circ$, with $\eta_p \approx 0.50$ and maximum $C_T = 0.30 - 0.40$. In Figure 6.20 the highest efficiency is at $\alpha_{max} = 22.5^\circ$. At this condition the thrust coefficient for a phase of 90° is measured to above 0.40. This is the highest recorded C_T at maximum propulsion efficiency.

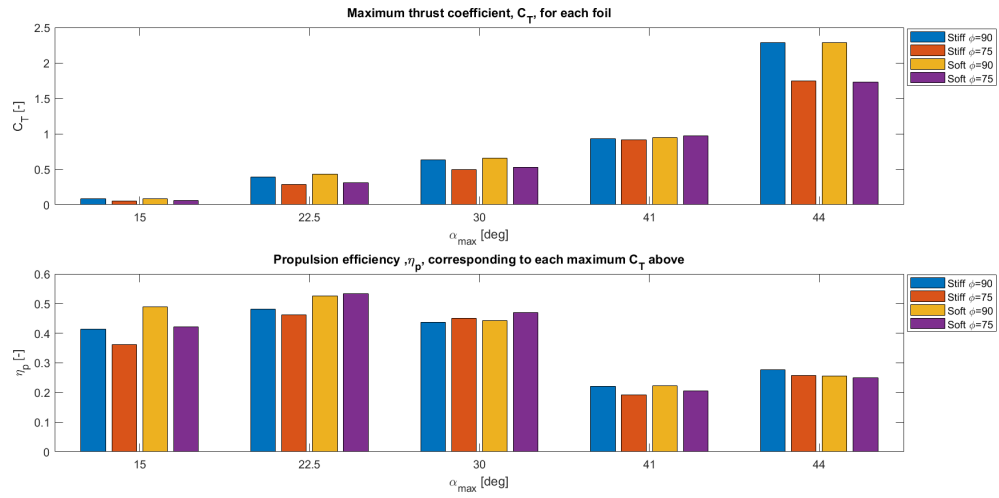


Figure 6.19: The top graph is the maximum thrust coefficient, C_T , from each run. The bottom graph is the corresponding η_p to each of the maximums in the top graph (same St). Test done for the stiff and flexible foil at $\phi = 90^\circ$ and $\phi = 75^\circ$. Test range is: $St = 0.20 - 0.40$ and $Re = 22500 - 52500$.

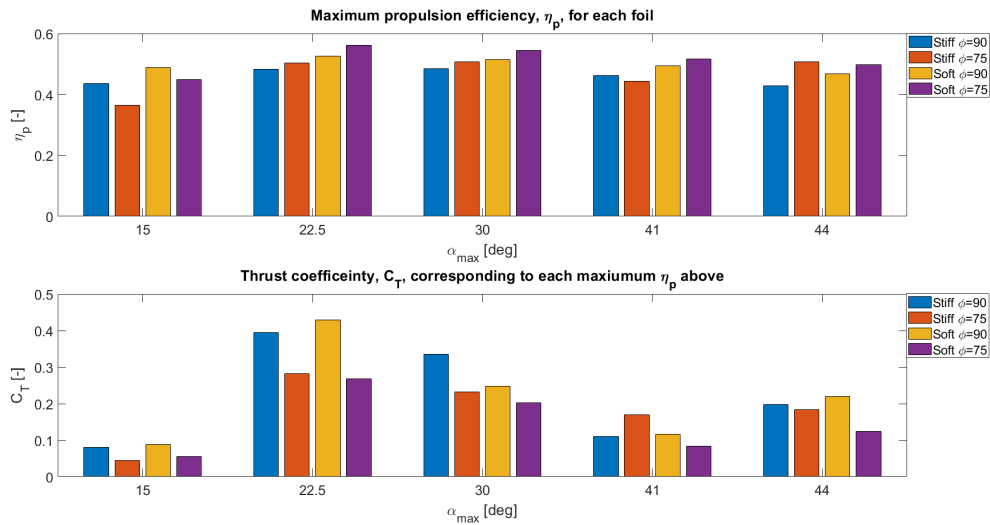


Figure 6.20: The top graph is the maximum propulsion efficient, η_p , from each run. The bottom graph is the corresponding C_T to each of the maximums in the top graph (same St). Test done for the stiff and flexible foil at $\phi = 90^\circ$ and $\phi = 75^\circ$. Test range is: $St = 0.20 - 0.40$ and $Re = 22500 - 52500$.

6.3.5 Lift Coefficient versus Propulsion Efficiency

This section describe the propulsion efficiency, η_p and the dependency of the thrust coefficient, C_T . In general a trend towards high η_p for low C_T is observed in earlier sections. The same trend is noticed when analyzing C_T versus η_p . In Figure 6.21 and 6.22 η_p versus C_T is illustrated for $\phi = 75^\circ$ and $\phi = 90^\circ$, respectively. The tendency is that flexible foil (red) has higher efficiency relative to stiff foil (blue). In Section 6.3.1 and 6.3.2 the results showed that the flexible foil has a somewhat lower C_P than the stiff foil, at $\theta > 10^\circ$. The thrust coefficient is the same for flexible and stiff foil. Recall Equation 29, a smaller C_P for the same C_T will give higher η_p .

$$\eta_p = \frac{C_T}{C_P} \quad (40)$$

Figure 6.23 is a complete illustration of C_T versus η_p for all the runs done in this thesis. A plateau with $\eta_p > 0.5$ is located for $C_T < 0.45$. For higher C_T the efficiency is smaller. For $C_T > 1.0$ the highest η_p is 0.36. Figure 6.24 is a zoom of the highest η_p , from Figure 6.23. C_T is in the range of 0.05-0.55. For the flexible foil (red and pink markers) with $C_T = 0.1 - 0.35$ the efficiency is somewhat higher than the efficiency of the stiff foil (black and blue markers). In this range most of the runs for flexible foil have $\eta_p > 0.5$.

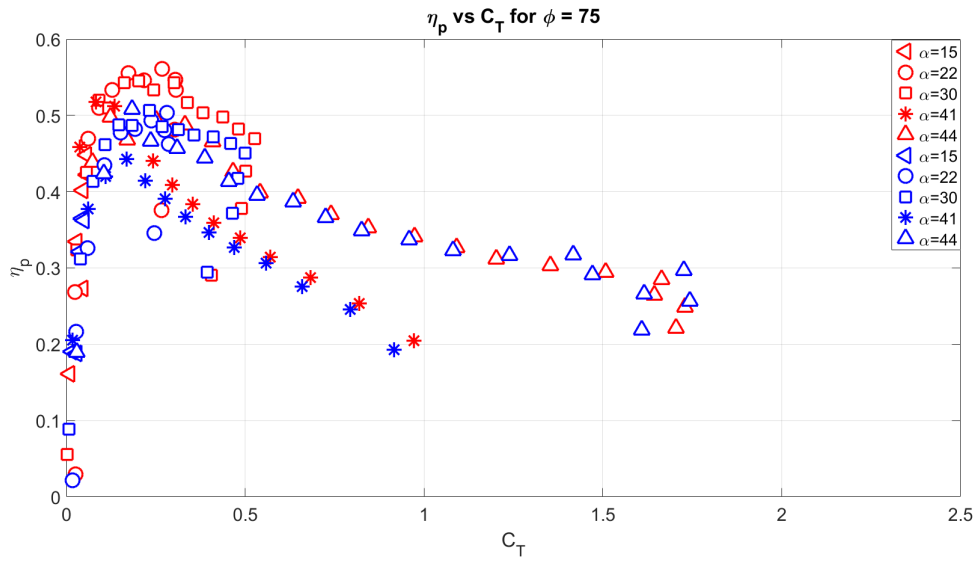


Figure 6.21: C_T versus η_p for $\phi = 75^\circ$. Red is the flexible foil. Blue is the stiff foil

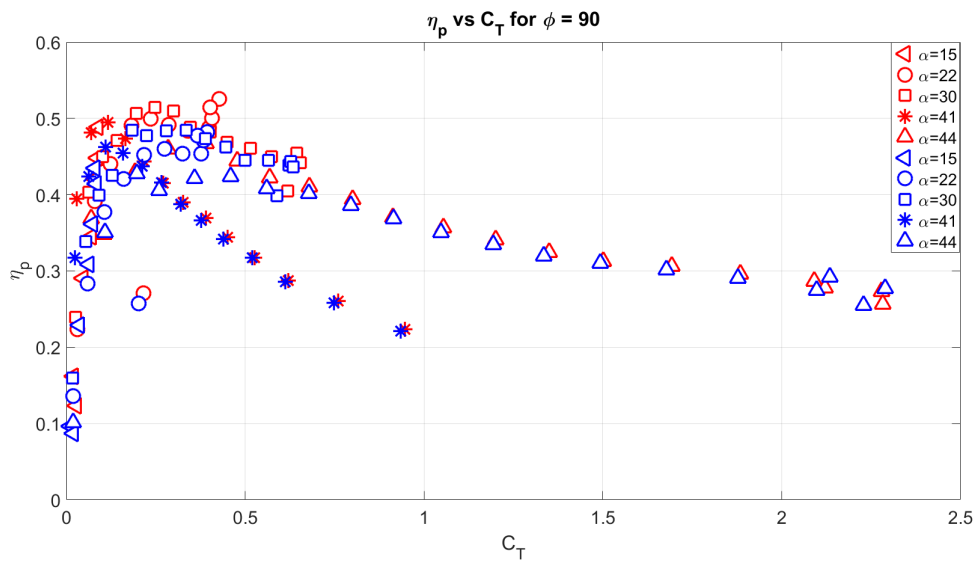


Figure 6.22: C_T versus η_p for $\phi = 90^\circ$. Red is the flexible foil. Blue is the stiff foil

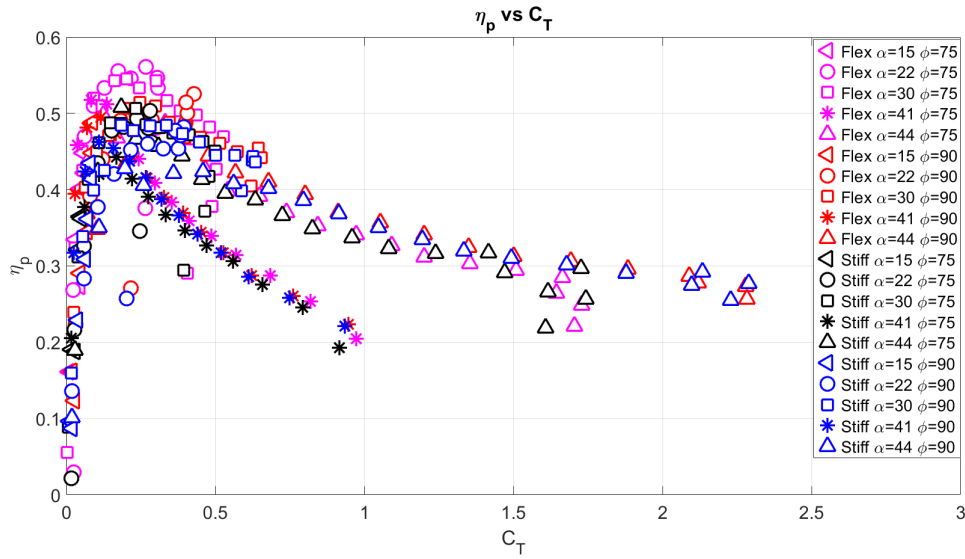


Figure 6.23: C_T versus η_p for all the runs. Red markers is the flexible foil with $\phi = 75^\circ$, pink markers is the flexible foil with $\phi = 90^\circ$, black markers is the stiff foil with $\phi = 75^\circ$ and blue markers is the stiff foil with $\phi = 90^\circ$.

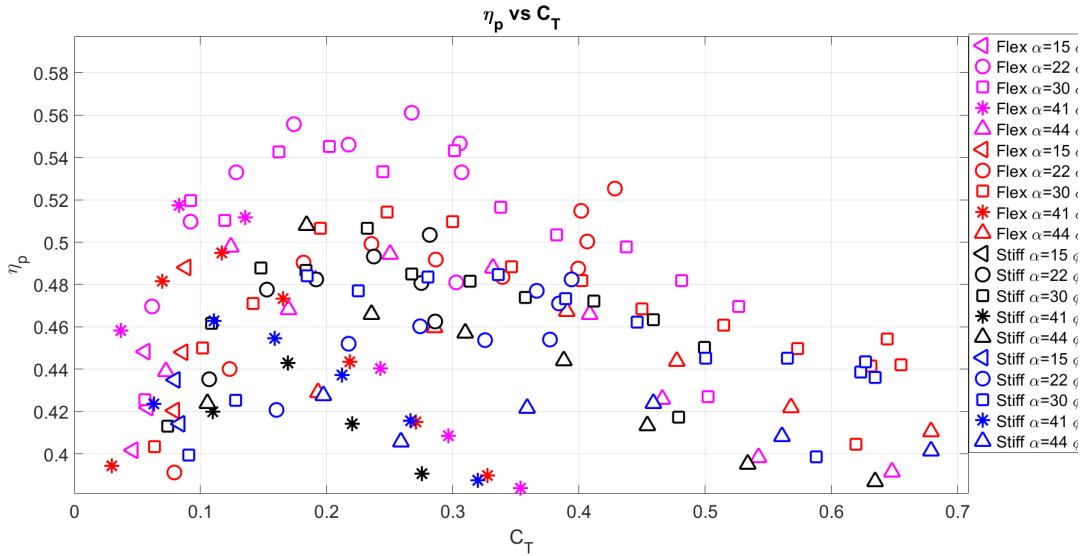


Figure 6.24: A zoom of the highest η_p . C_T versus η_p for all the runs. Red markers is the flexible foil with $\phi = 75^\circ$, pink markers is the flexible foil with $\phi = 90^\circ$, black markers is the stiff foil with $\phi = 75^\circ$ and blue markers is the stiff foil with $\phi = 90^\circ$.

6.3.6 Power, Thrust and Lift During One Oscillation

The motion of the foil is oscillating in yaw and sway. In this section, the motion of the foil is compared with the generated thrust and power of the foil. To see how this changes during the period of motion and when the thrust is generated. The power coefficient, C_P , is the real-time value during on oscillation and was calculated with Equation 27. Thrust coefficient, C_T , is the real-time value from the drag force F_D and was calculated with Equation 25.

In Figure 6.25, it is noticed that C_P is negative during the oscillation, the foil is using energy when moving in sway and yaw. The thrust coefficient, C_T , is oscillating between negative and positive values. For negative C_T , the foil is consuming energy from the water. During the oscillation, the foil is consuming energy when the foil is at maximum sway amplitude ($y_{sway} = \pm 0.075$ m) and slightly before θ_{yaw} crosses 0° . However, most of the time, C_T is positive, and the foil is generating thrust. Maximum C_T occur slightly after y_{sway} crosses zero and when θ_{yaw} is close to maximum.

The foil is generation the most thrust in the middle of motion when the AoA is largest. It is consuming energy when changing sway direction from negative to positive (or the other way around).

In Figure 6.26 the lift (C_L), moment (C_M) and thrust (C_T) is illustrate for the flexible foil for one oscillation. The generated lift is larger than the thrust during one oscillation. The moment is 180° out of phase and is quite small relative to the lift and thrust (in Figure 6.25, a factor of 10 is used for C_M).

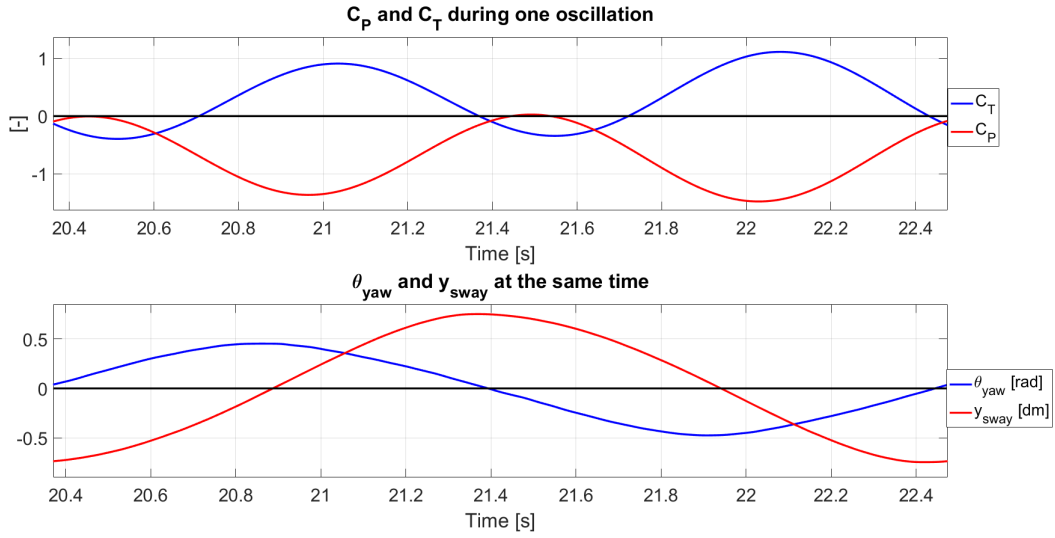


Figure 6.25: Motion and forces during one oscillation of motion for the run with highest propulsion efficiency ($\eta_p = 0.56$). It was obtained for the flexible foil with $\phi = 75^\circ$ and $\alpha_{max} = 22.5^\circ$ at $St = 0.285$. The recorded mean thrust and power coefficients is $C_T = 0.28$ and $C_P = 0.50$

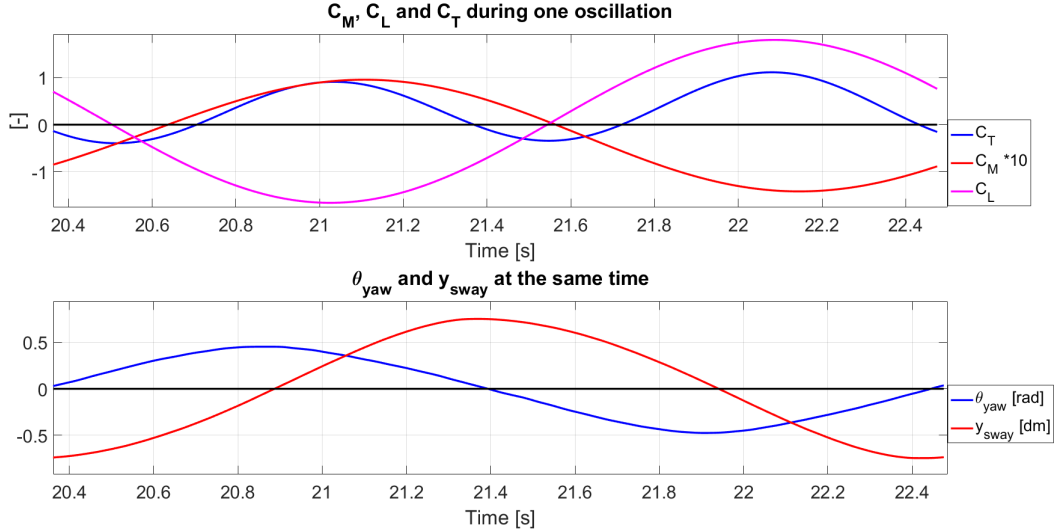


Figure 6.26: Motion and forces during one oscillation of motion for the run with highest thrust coefficient recorded ($C_{T_{stiff}} = 2.289$ and $C_{T_{flexible}} = 2.282$). It is obtained with $\phi = 90^\circ$ and $\alpha_{max} = 44^\circ$ at $St = 0.65$.

In Figure 6.27 the flexible and stiff foil is compared during one oscillation of motion, with regard to the lift, thrust and moment coefficients for the AoA with highest propulsion efficiency ($\eta_p = 0.56$, $\alpha_{max} = 22.5^\circ$). The flexible foil has a somewhat higher maximum of C_T during one oscillation, relative to the graph of the stiff foil. In earlier Sections, it was found that the flexible foil tends to have a higher C_T and η_p , than the stiff foil. It seems like the graph for the flexible foil for $C_T > 0$ lies above the graph of the stiff foil. The integral (area) over one period will give a higher C_T for the flexible foil, compared to the stiff foil.

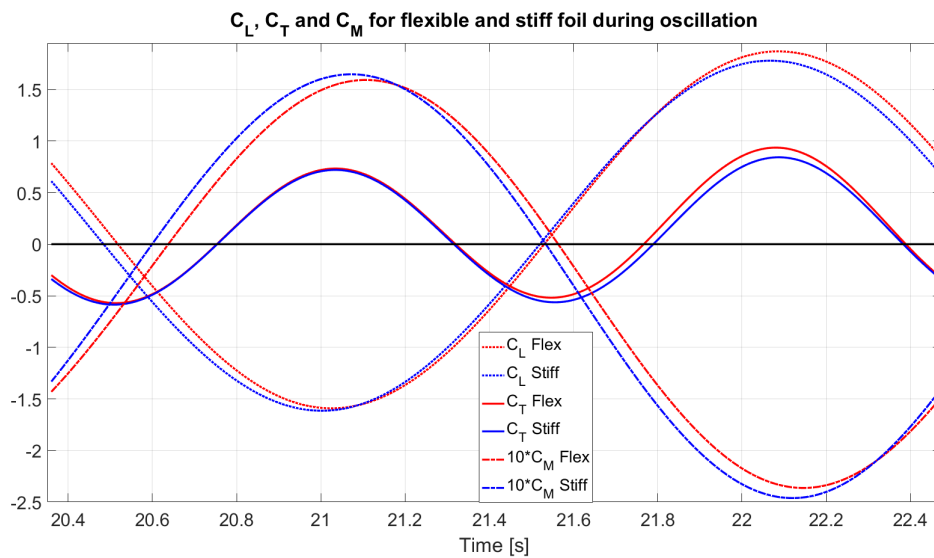


Figure 6.27: Lift, thrust and moment coefficients during one oscillation of motion for the AoA with highest propulsion efficiency ($\eta_p = 0.56$, $\alpha_{max} = 22.5^\circ$)

7 Conclusion

The model-scale experiments has been utilized for two hydrofoils with different stiffness. The dimension of the foil and the motion parameter was chosen to cover the most optimal range observed in nature [23] [36] [20] and indicated by other studies [3] [7]. Test was conducted at four Reynolds number ($Re = 22500, 37500, 45000, 52500$) and two phases ($\phi = 75^\circ, 90^\circ$). The stiff foil had turbulence stimulation (TS). The flexible foil had a grid on one side and smooth on the other side.

Agreement was found for both foils with the experiments from Read in 2003 [29] and Bösch in 2015 [7]. Specially the flexible foil had similarities in efficiency. The maximum efficiency recorded by Bösch's optimization study ($\approx 65\%$) could not be repeated.

The highest propulsion efficiency was recorded at $Re = 37500$ and $\alpha_{max} = 22.5^\circ$. The optimal range in nature ($St = 0.22 - 0.34$) was noticed as the range with highest efficiency ($\eta_p = 0.49 - 0.56$), regardless the stiffness of the foil.

The findings can be summarized to:

- The yaw angle amplitude affected the power consumption and the thrust generation. At low yaw angle, the power consumption and thrust generation were higher for a phase of 75° . A yaw angle higher than 20° a phase of 90° generated the most thrust and poser.
- A tendency towards the flexible foil with a phase of 75° for highest efficiency. Largest recorded efficiency of 56.1%.
- For thrust coefficient < 0.6 , a plateau of the highest efficiency is recorded.
- Strouhal number larger than 0.60 created the largest thrust ($C_T > 2.0$)
- A yaw angle of 10° generates the highest thrust, and consume the largest amount of energy, compared to yaw angle $> 20^\circ$.

7.1 Recommendation for further work

The flexible foil has shown promising results for the efficiency, compared to a foil with stiffer cross-sectional properties. An attempt was made in the design to make the foil twist to lower AoA at higher loads. Other designs can be made with a higher expected twist angle. The time was limited in this thesis, a larger test range of different expected twist angles might be considered, and other phases might also give promising results.

The following topics could be investigated further:

- Different design concerning the placement of the spars in the cross-section to expect a larger twist. Other material properties might also be of interest.
- Different turbulence stimulation on the flexible foil was not tested. Turbulence stimulation is a large topic and was not a part of this thesis.
- time was limited, and the optical measurement was not successfully conducted. The deflection and the behaviour of a flexible foil, and how this effect the lift and drag, can be of interest.

References

- [1] All about circuits. From: <https://www.allaboutcircuits.com/textbook/direct-current/chpt-9/strain-gauges/> (22.11.18).
- [2] ABBOTT, I. H. Theory of wing sections : including a summary of airfoil data, 2012.
- [3] ANDERSON, J., S.-K. B. D. . T. M. Oscillating foils of high propulsive efficiency. *Journal of Fluid Mechanics* 360 (1998), 41–72.
- [4] AUTODESK.HELP. Mesh settings inventor. From: <https://knowledge.autodesk.com/support/inventor-products/learn-explore/caas/CloudHelp/cloudhelp/2014/ENU/Inventor/files/GUID-10291E2B-03E4-4A5E-AB23-BC6083B6538A-htm.html/> (10.02.19).
- [5] BLAND, J. M., AND ALTMAN, D. G. Statistics notes: Measurement error and correlation coefficients. *BMJ* 313, 7048 (1996).
- [6] BRASLOW, A. L., AND KNOX, E. C. Simplified method for determination of critical height of distributed roughness particles for boundary-layer transition at mach numbers from 0 to 5, 1958.
- [7] BÖSCH, L. Thrust optimisation of an oscillating hydrofoil, 2017.
- [8] CARICHAEL, B. H. Low reynolds number airfoil survey. *NASA Contractor Report* (1981).
- [9] CENGEL, Y. A., AND CIMBALA, J. M. *Fluid mechanics : fundamentals and applications*, 3rd ed. in si units. ed. McGraw-Hill, Boston, 2014.
- [10] CHABAUD, V. Lecture notes in tmr7 experimental methods in marin hydrodynamic, October 2018.
- [11] CLARK, L. Aeroastro magazine - mit - faculty profile. From: <http://web.mit.edu/aeroastro/news/magazine/aeroastro-no3/2006drela.html> (2006).

- [12] D GARCIA, JEAN-JOSÉ ORTEU, L. P. A combined temporal tracking and stereo-correlation technique for accurate measurement of 3d displacements: application to sheet metal forming. *Journal of Materials Processing Technology* (2002), 736–742.
- [13] DRELA, M., AND YOUNGREN., H. Xfoil - subsonic airfoil development system. From: <https://web.mit.edu/drela/Public/web/xfoil/> (06.03.19).
- [14] ECSEDI, I., AND BAKSA, A. Notes on the centre of shear. *International Journal of Mechanical Engineering Education* 40, 3 (2012), 220–233.
- [15] ELOY, C. *Journal of fluids and structures*. 205–218.
- [16] FALTINSEN, O. M. *Sea loads on high-speed marine vehicles*, 2000.
- [17] FORNBERG, B. Generation of finite difference formulas on arbitrarily spaced grids. *Mathematics of Computation* 51, 184 (1988), 699–706.
- [18] GODØ, J. M. Hydrodynamic design of a foilborne flapping foil ship (unpublished master’s thesis), 2015.
- [19] GRACEY, W. Summary of methods of measuring angle of attack on aircraft, 1958.
- [20] GRAHAM K TAYLOR, MICHAEL S TRIANTAFYLLOU, C. T. *Animal locomotion*, 2010.
- [21] GULDHAMMER, H. E. *Ish propeller diagrams : log-log-diagrams of the wageningen b-series*, 1984.
- [22] HOVER, F., HAUGSDAL, , AND TRIANTAFYLLOU, M. Effect of angle of attack profiles in flapping foil propulsion. *Journal of Fluids and Structures* 19, 1 (2004), 37–47.
- [23] LIGHTHILL, M. Aquatic animal propulsion of high hydromechanical efficiency. *Journal of Fluid Mechanics* 44, 2 (1970), 265–301.

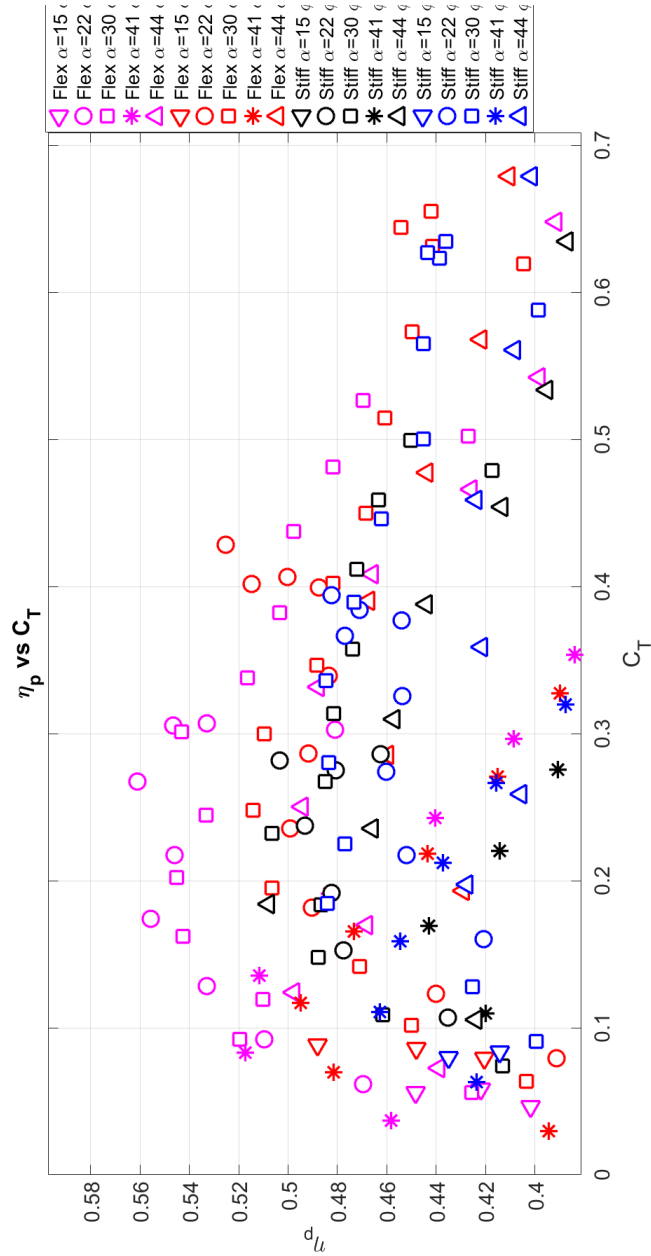
- [24] MINSAAS, K., AND STEEN, S. *Lecture Notes TMR Naval Hydrodynamics at NTNU*. Institutt for marin teknikk, NTNU, 2014.
- [25] MSE. Measurement science enterprise. mse inc. website, June 2018. <http://measurementsci.com/how-an-ldv-lda-works/>.
- [26] NORRIE, D. H. A first course in the finite element method: D.I. logan, pws engineering, boston, u.s.a., 1986, 617 pages, isbn 0-534-05394-7 (book review). *Finite Elements in Analysis Design* 3, 2 (1987), 162–163.
- [27] PETTERSEN, B. *Marin Teknikk 3 - Hydrodynamikk*. Institutt for marin teknikk, NTNU, 2007.
- [28] PHOTRON. Fastcam mh4. From: <https://photron.com/fastcam-mh4-10k/> (29.11.2018).
- [29] READ, D., HOVER, F., AND TRIANTAFYLLOU, M. Forces on oscillating foils for propulsion and maneuvering. *Journal of Fluids and Structures* 17, 1 (2003), 163–183.
- [30] ROOIJ, R., AND TIMMER, W. Roughness sensitivity considerations for thick rotor blade airfoils. *Journal of Solar Energy Engineering-transactions of The Asme - J SOL ENERGY ENG* 125 (01 2003).
- [31] SAVIO, L. Measurements of the deflection of a flexible propeller blade by means of stereo imaging. *Fourth International Symposium on Marine Propulsors, Texas, USA* (2015).
- [32] SFAKIOTAKIS, M., LANE, D., AND DAVIES, J. Review of fish swimming modes for aquatic locomotion. *IEEE Journal of Oceanic Engineering* 24, 2 (1999), 237–252.
- [33] STEEN, S. *TMR7 - Experimental methods in Marine Hydrodynamics*. 2014.
- [34] STRATASYS. Material library. From: <https://store.stratasys.com/stratasysstorefront/stratasys/en/%26-Service-Consumables/c/1?text=defaultPagedisplay=allMaterials> (28.11.2018).

- [35] TAYLOR, G. K., NUDDS, R. L., AND THOMAS, A. L. R. Flying and swimming animals cruise at a strouhal number tuned for high power efficiency. *Nature* 425, 6959 (2003).
- [36] TAYLOR, G. K., NUDDS, R. L., AND THOMAS, A. L. R. Flying and swimming animals cruise at a strouhal number tuned for high power efficiency. *Nature* 425, 6959 (2003).

Appendices

A Graphs with C_T , C_P , η_p , and Static Lift and Drag

A.1 C_T vs η_p



II

Figure A.1: Red: Flexible foil ($\phi = 75^\circ$). Pink: Flexible foil ($\phi = 90^\circ$). Black: Stiff foil ($\phi = 75^\circ$). Blue: Stiff foil ($\phi = 90^\circ$)

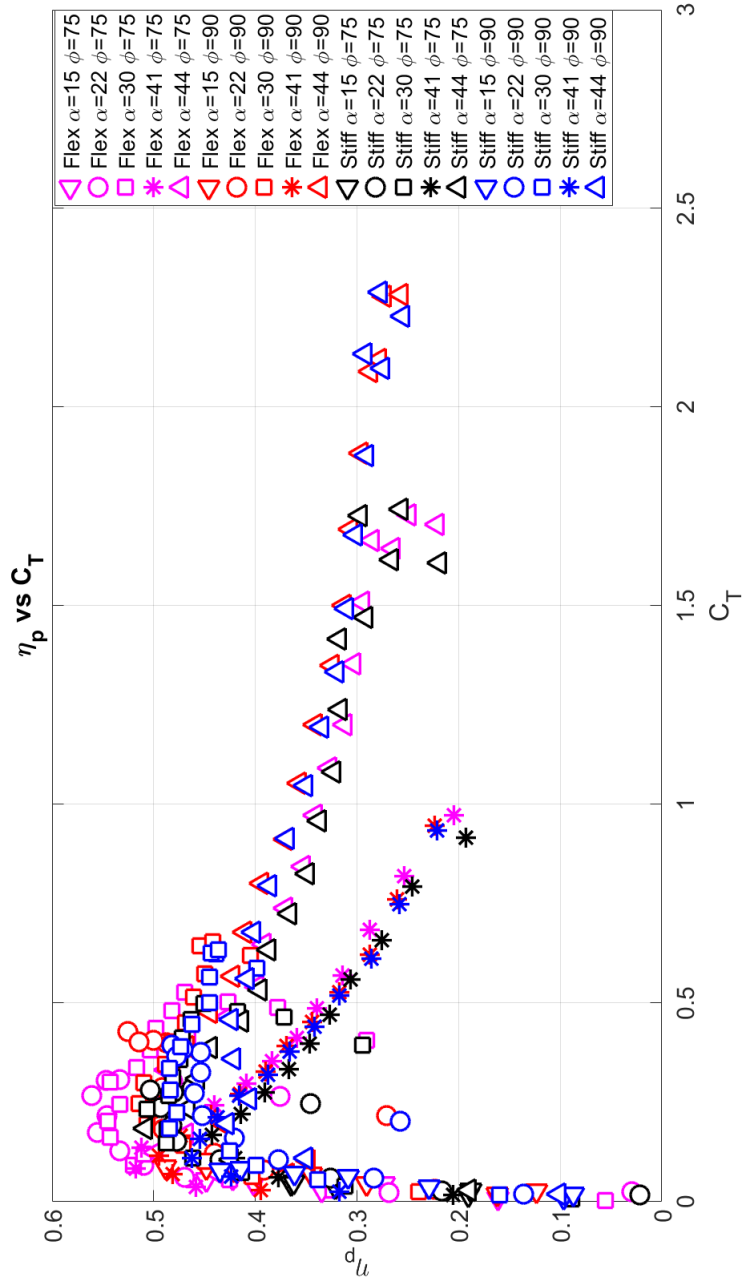


Figure A.2: Red: Flexible foil ($\phi = 75^\circ$). Pink: Flexible foil ($\phi = 90^\circ$). Black: Stiff foil ($\phi = 75^\circ$). Blue: Stiff foil ($\phi = 90^\circ$) III

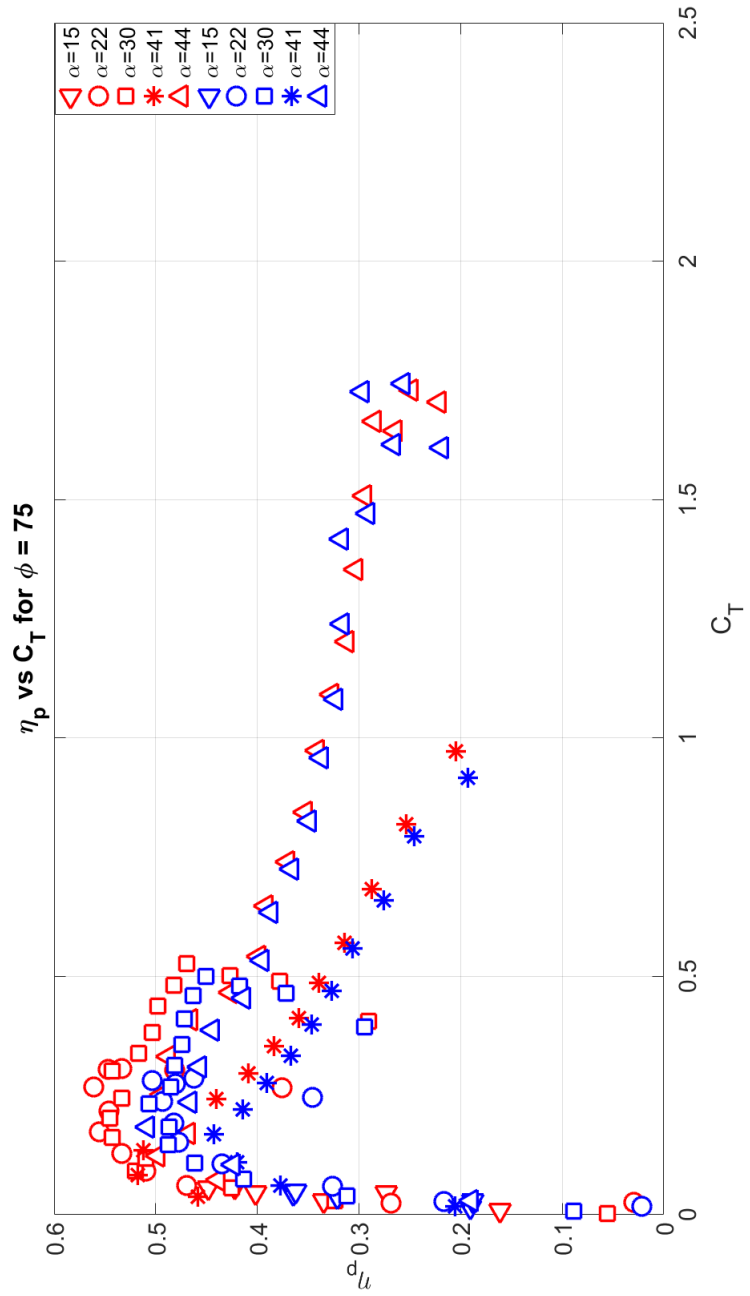


Figure A.3: $(\phi = 75^\circ)$
IV

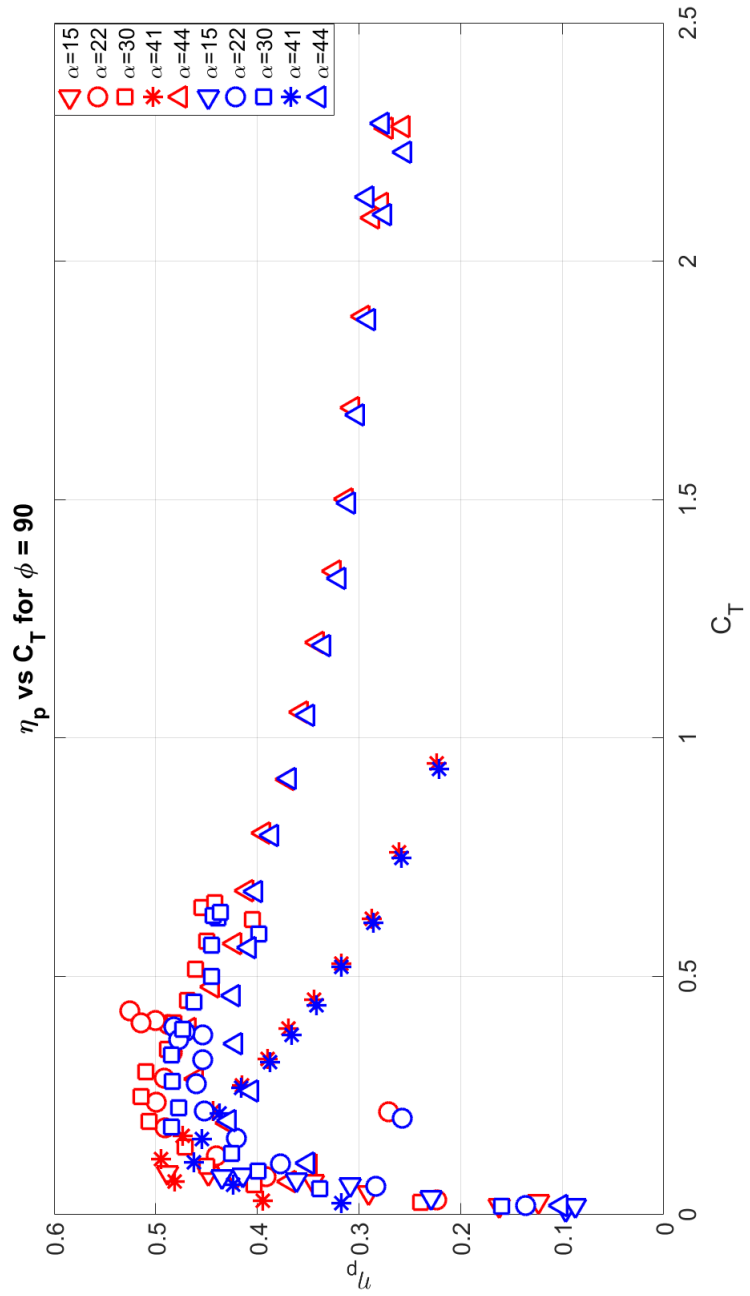
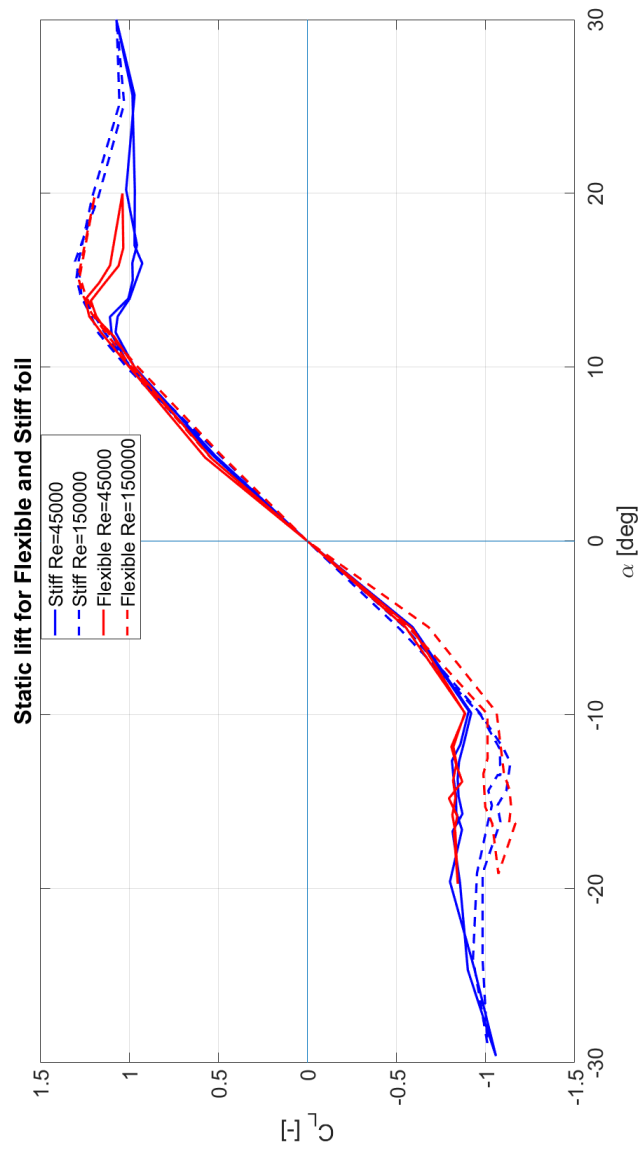
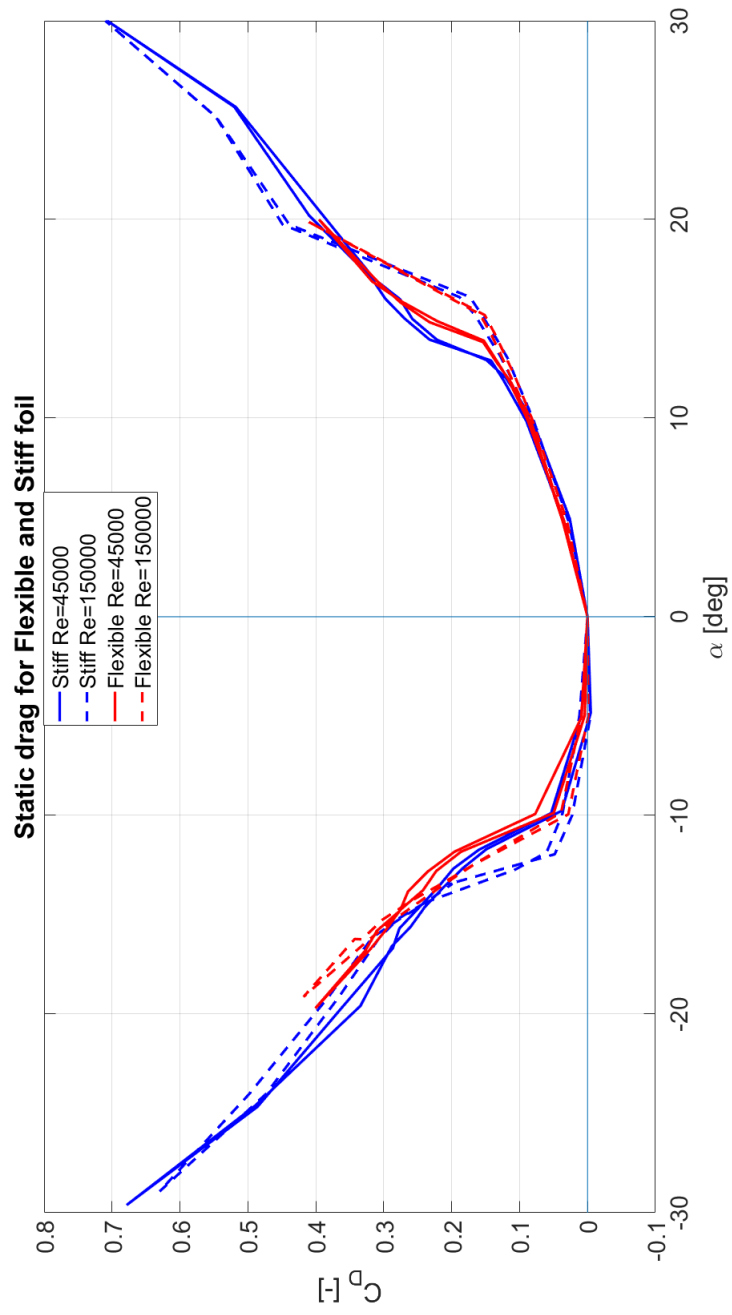
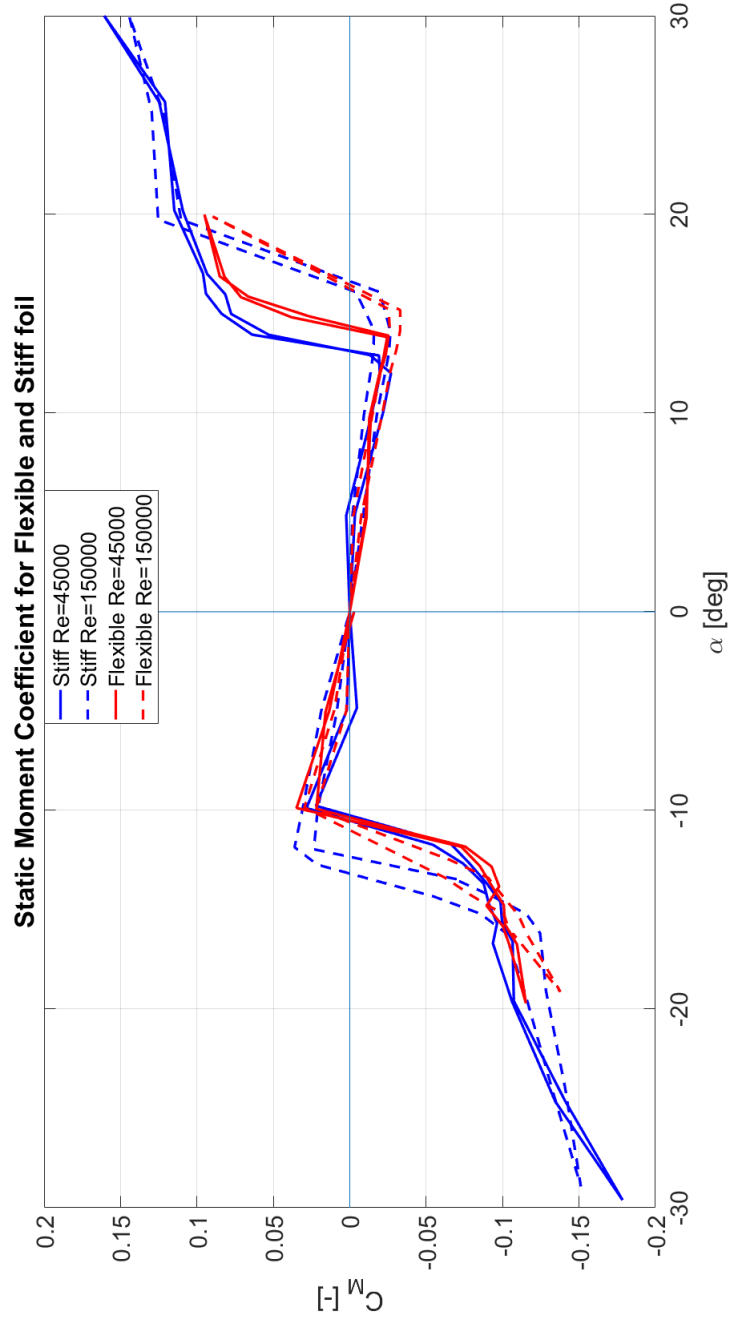


Figure A.4: $(\phi = 90^\circ)$

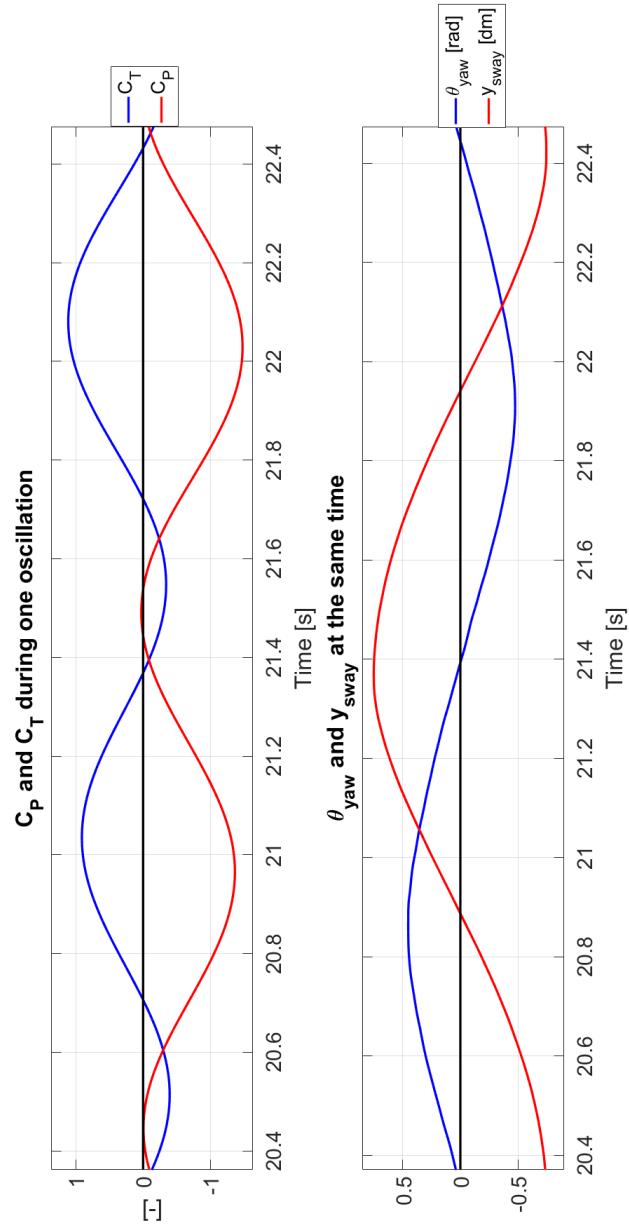
A.2 Static Lift and Drag

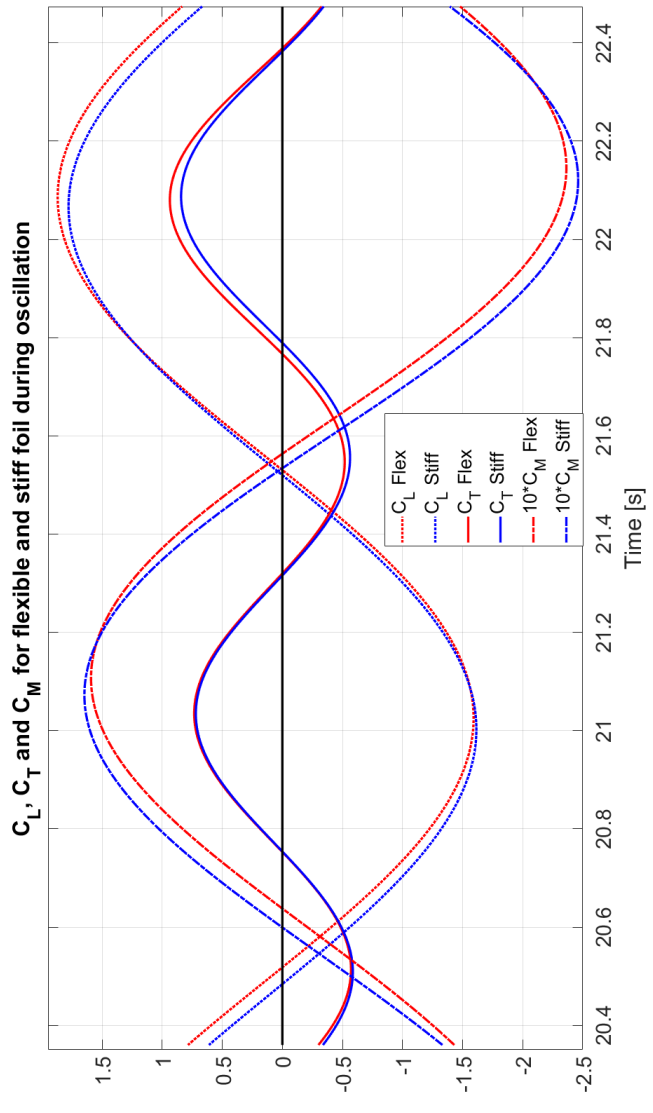




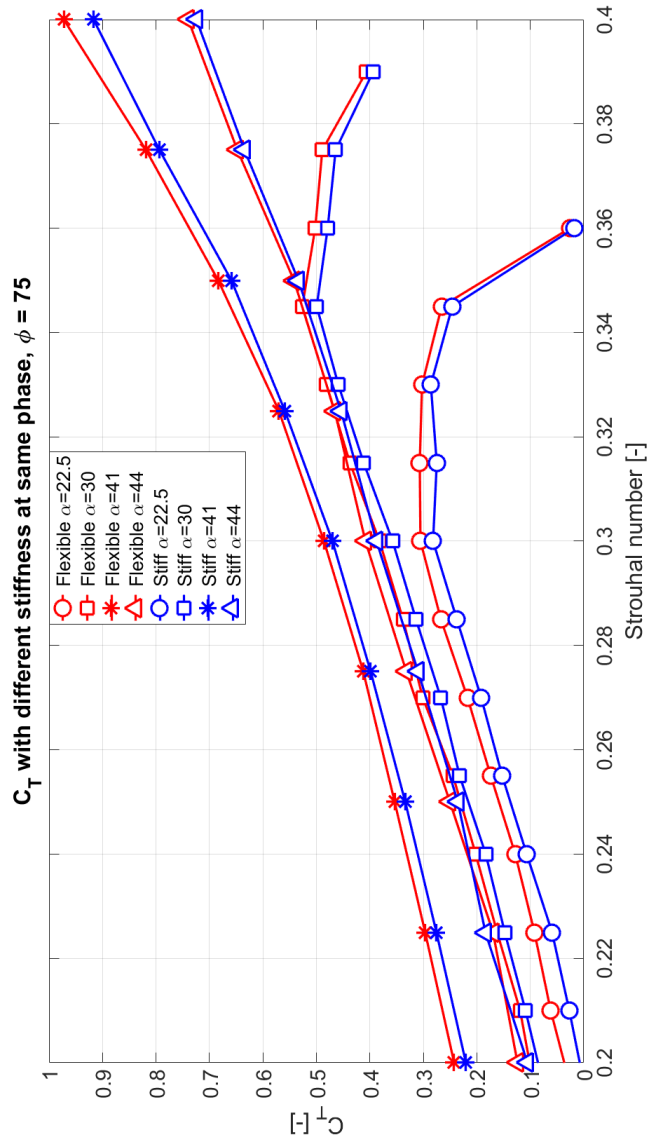


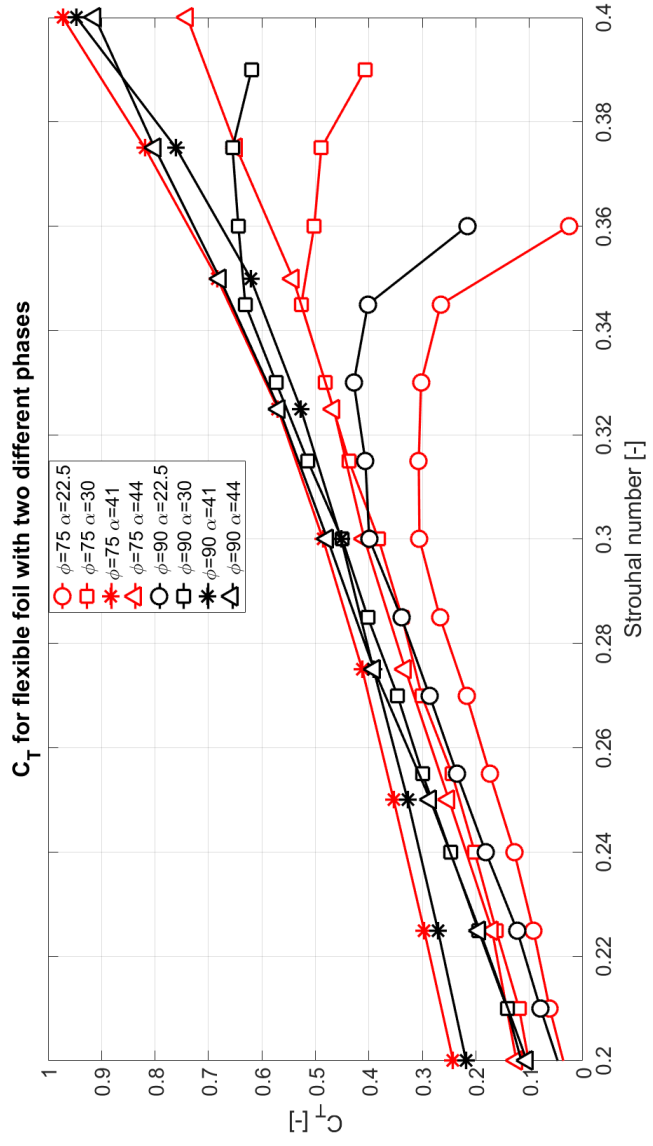
A.3 Forces During One Oscillation

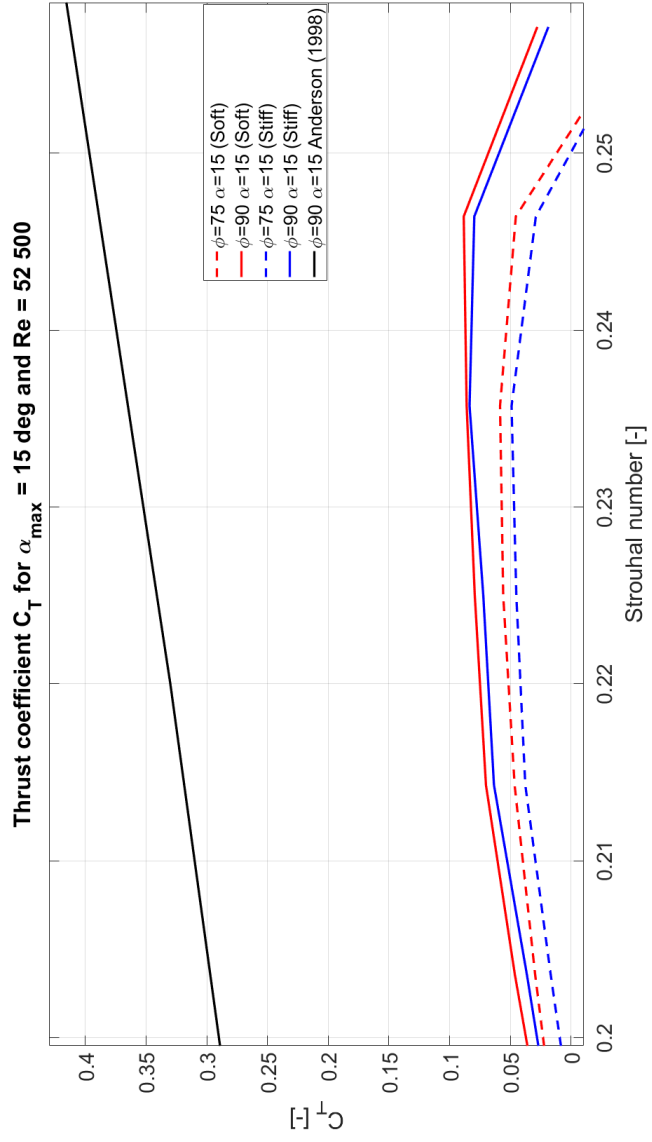


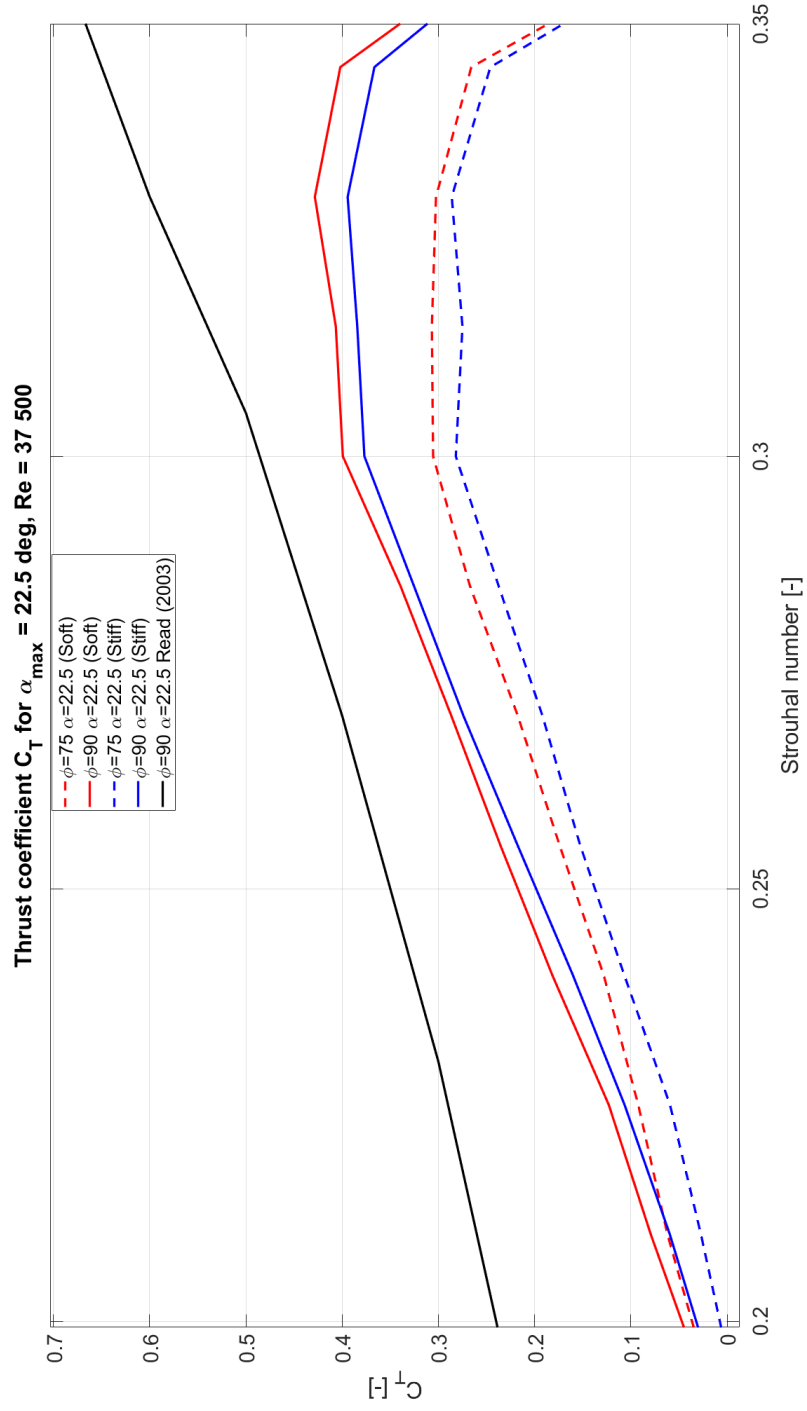


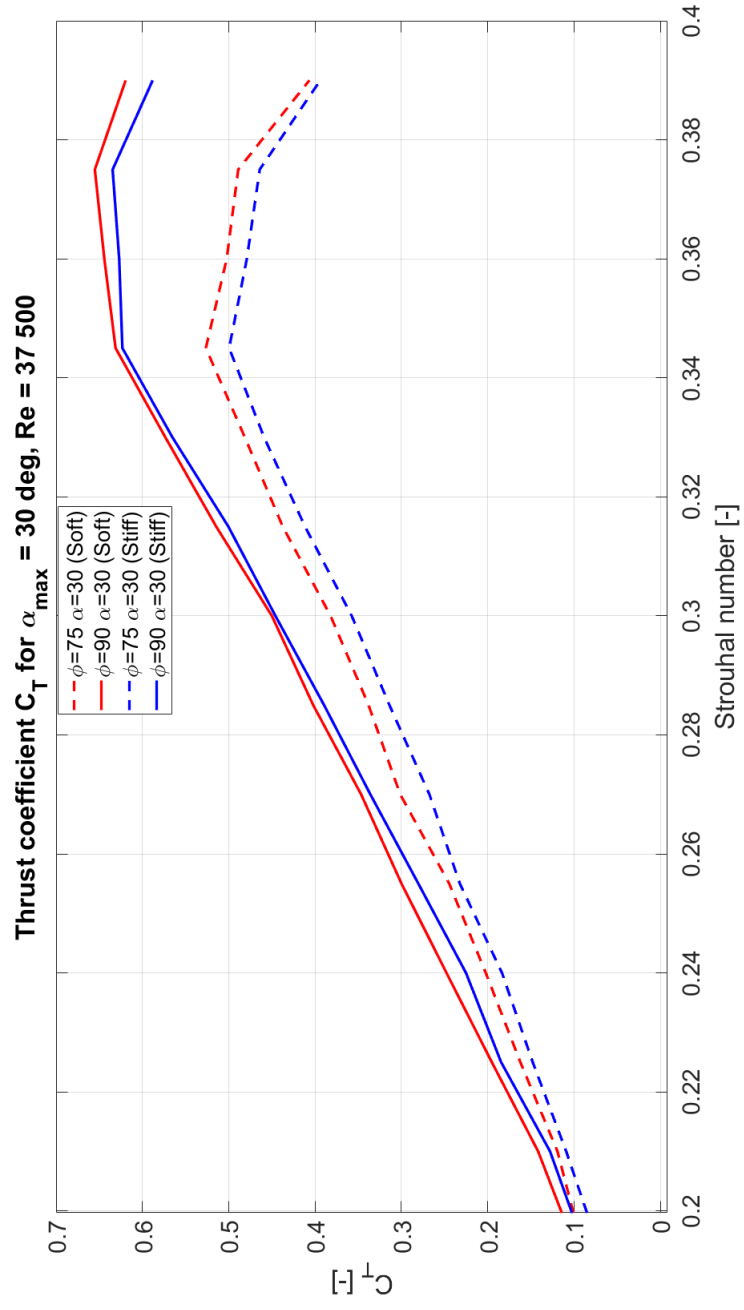
A.4 C_T

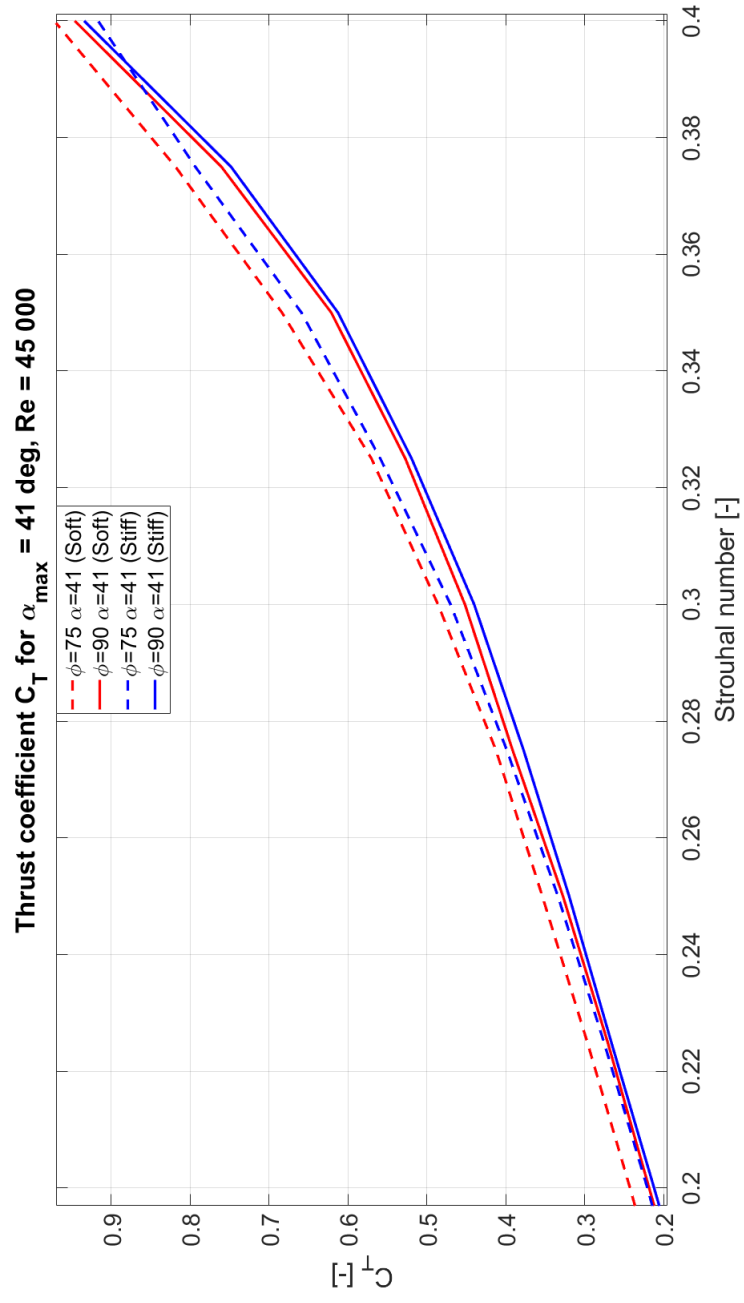


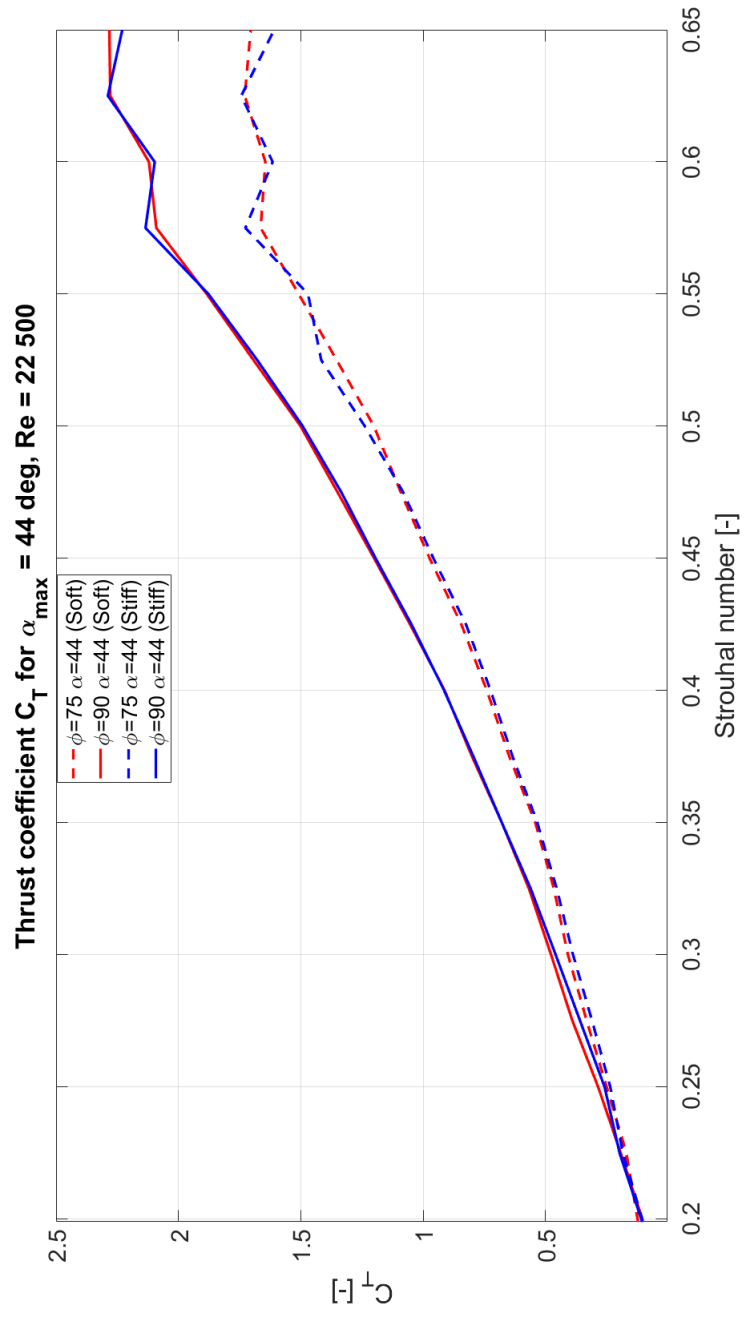




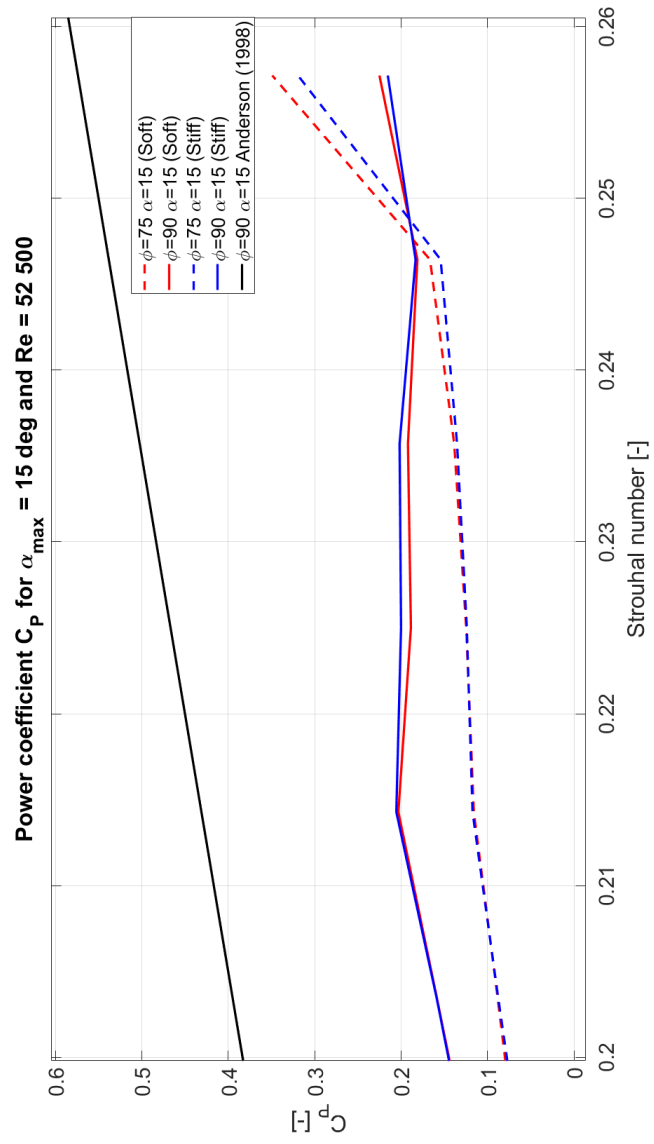


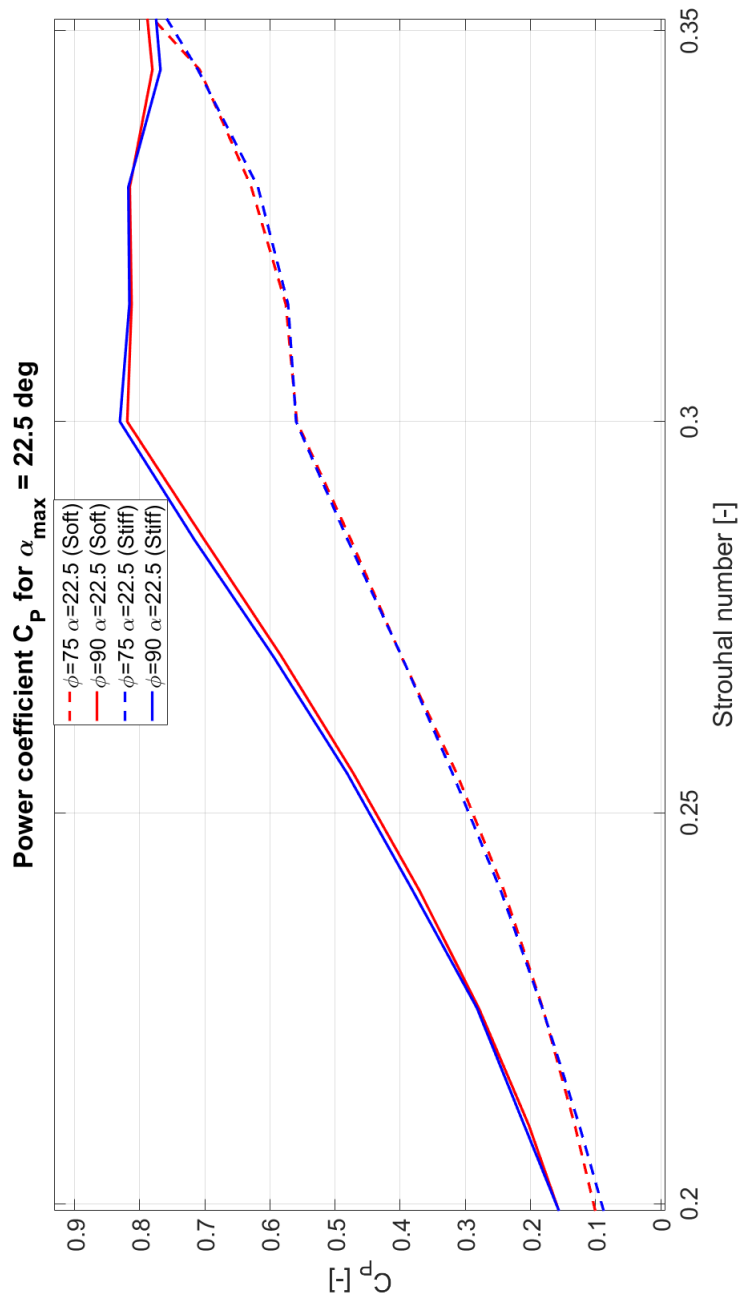


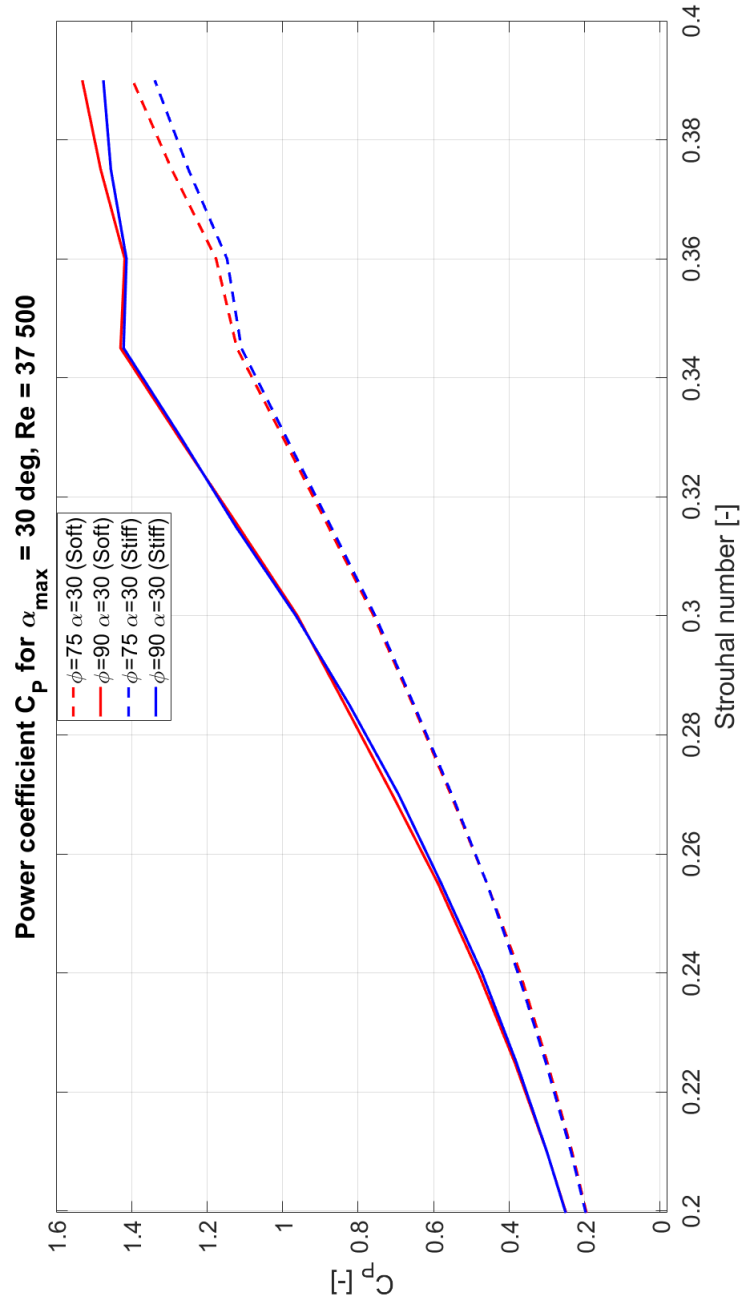


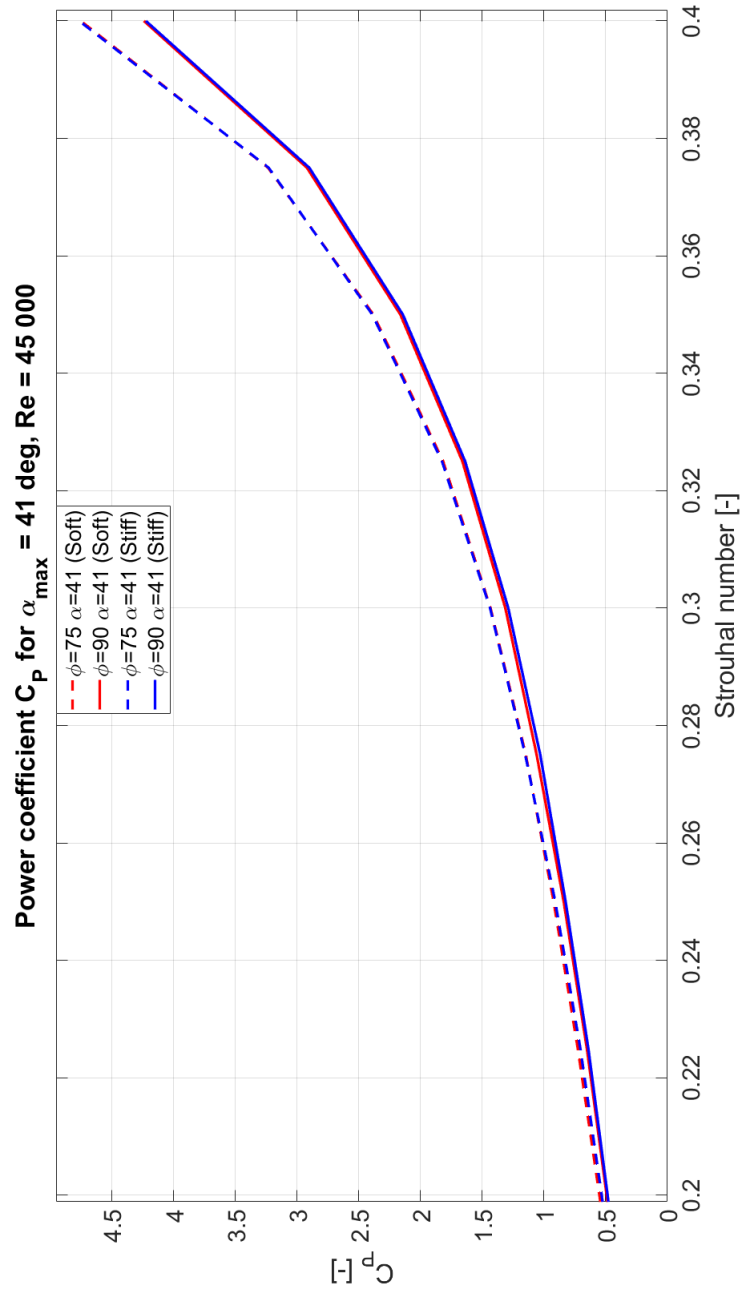


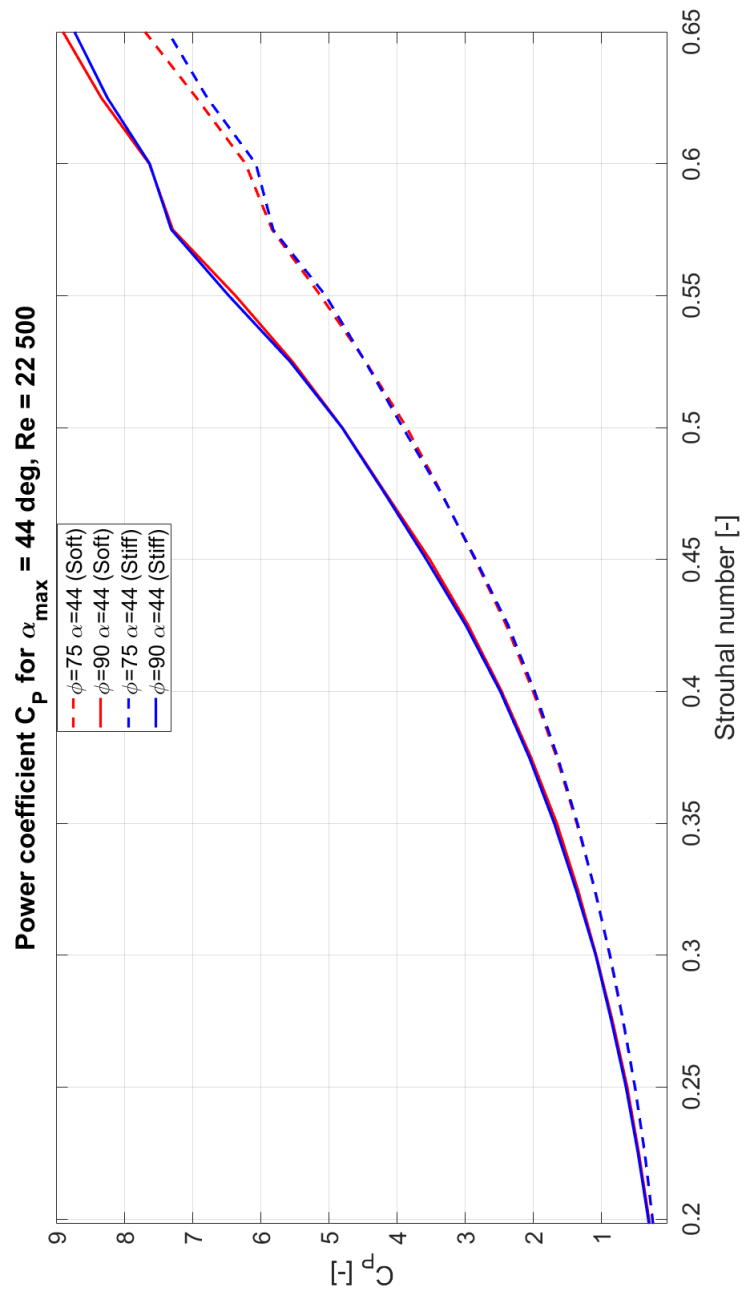
A.5 C_P



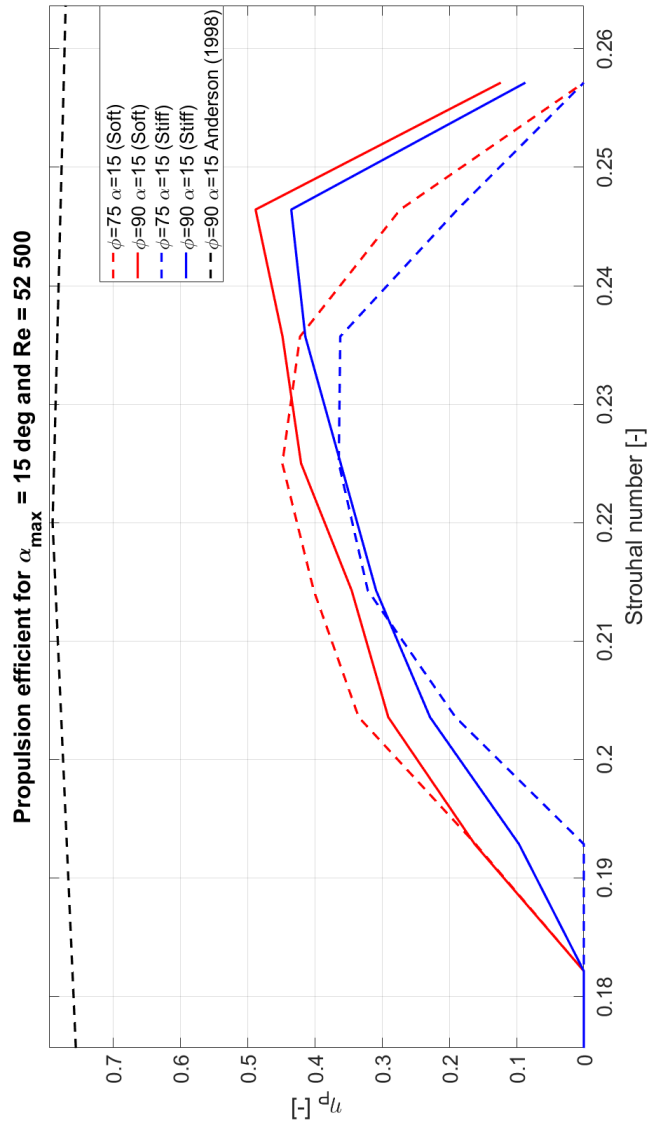


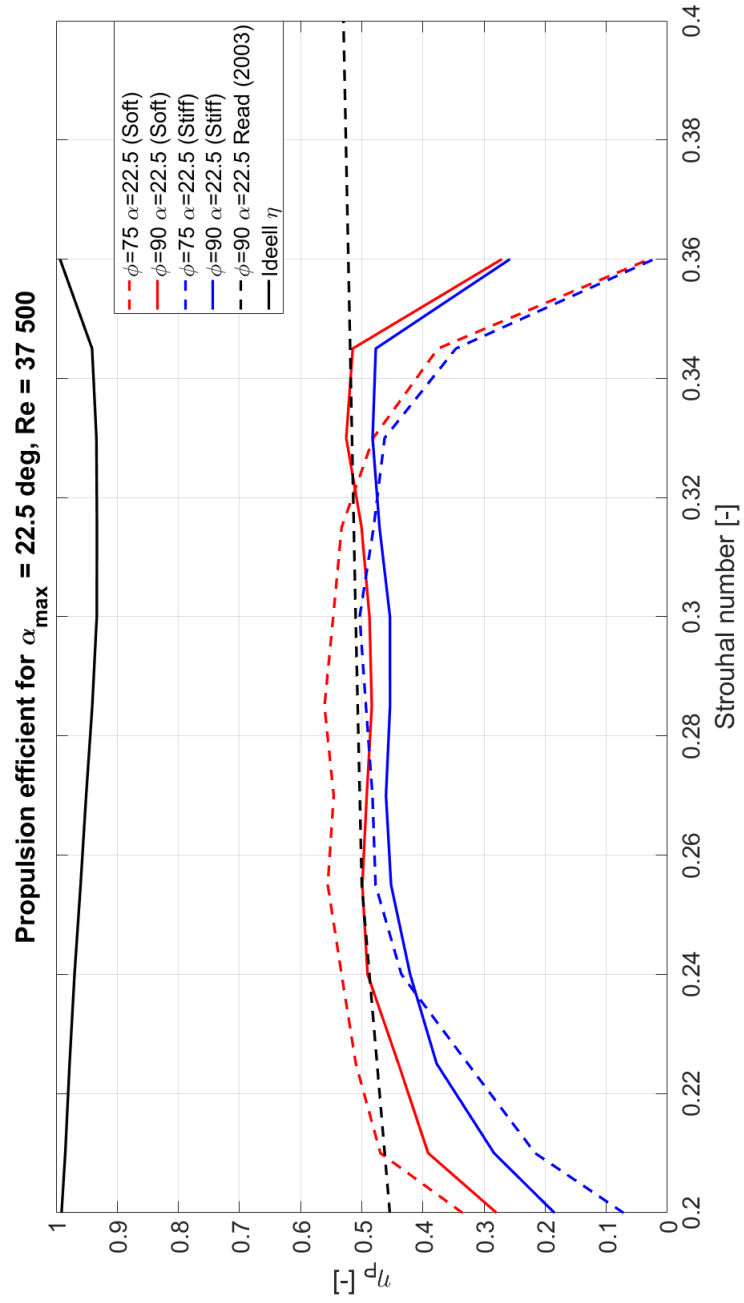


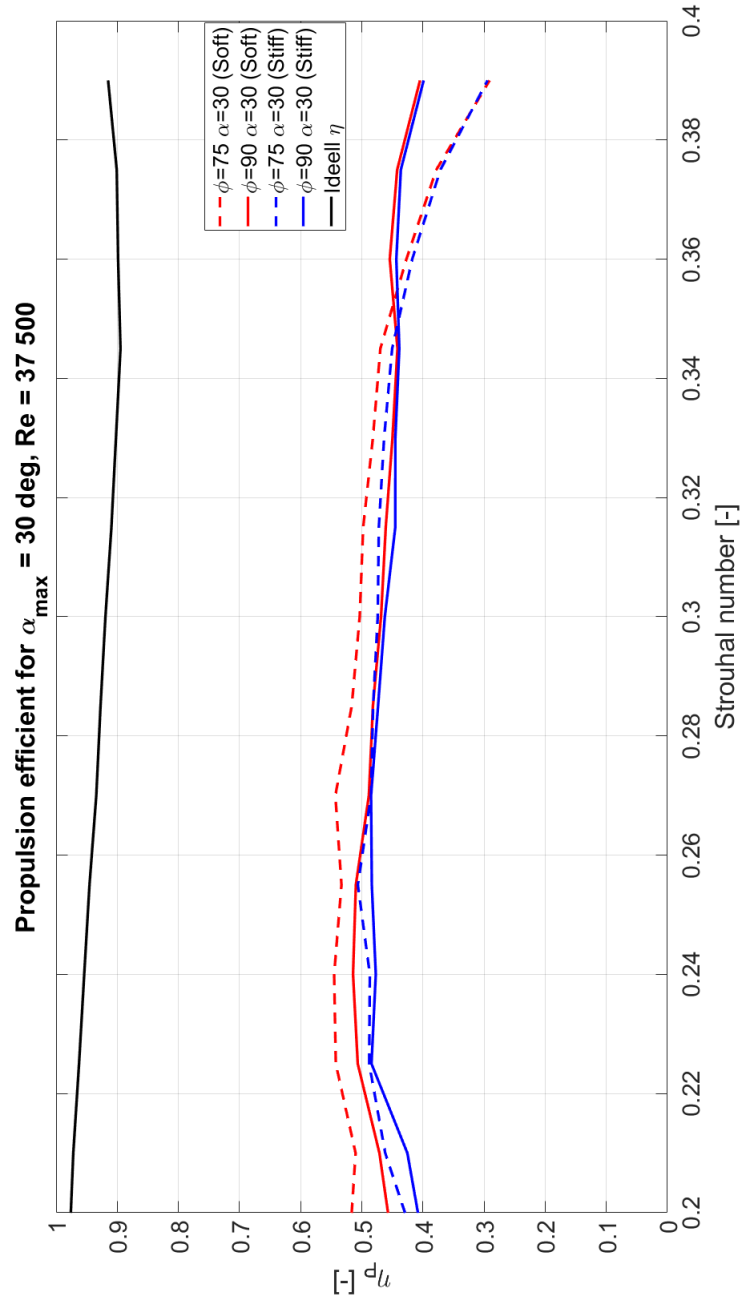


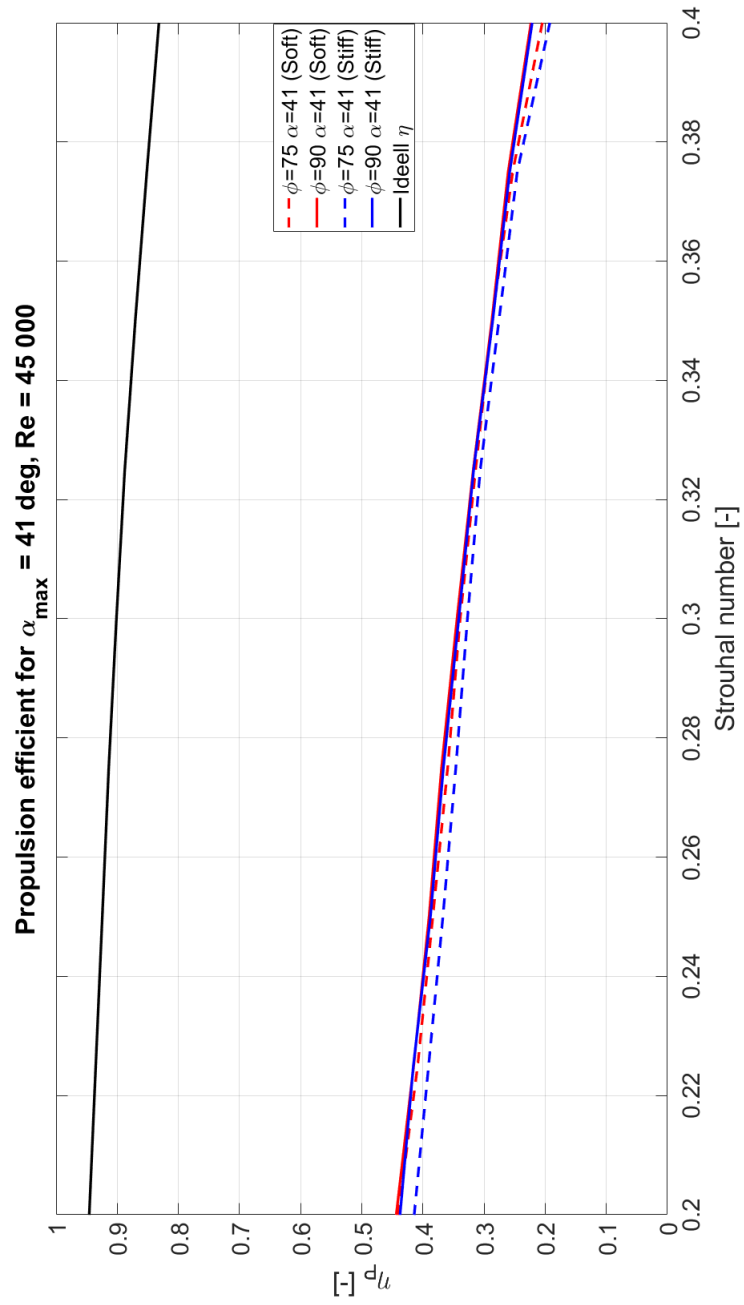


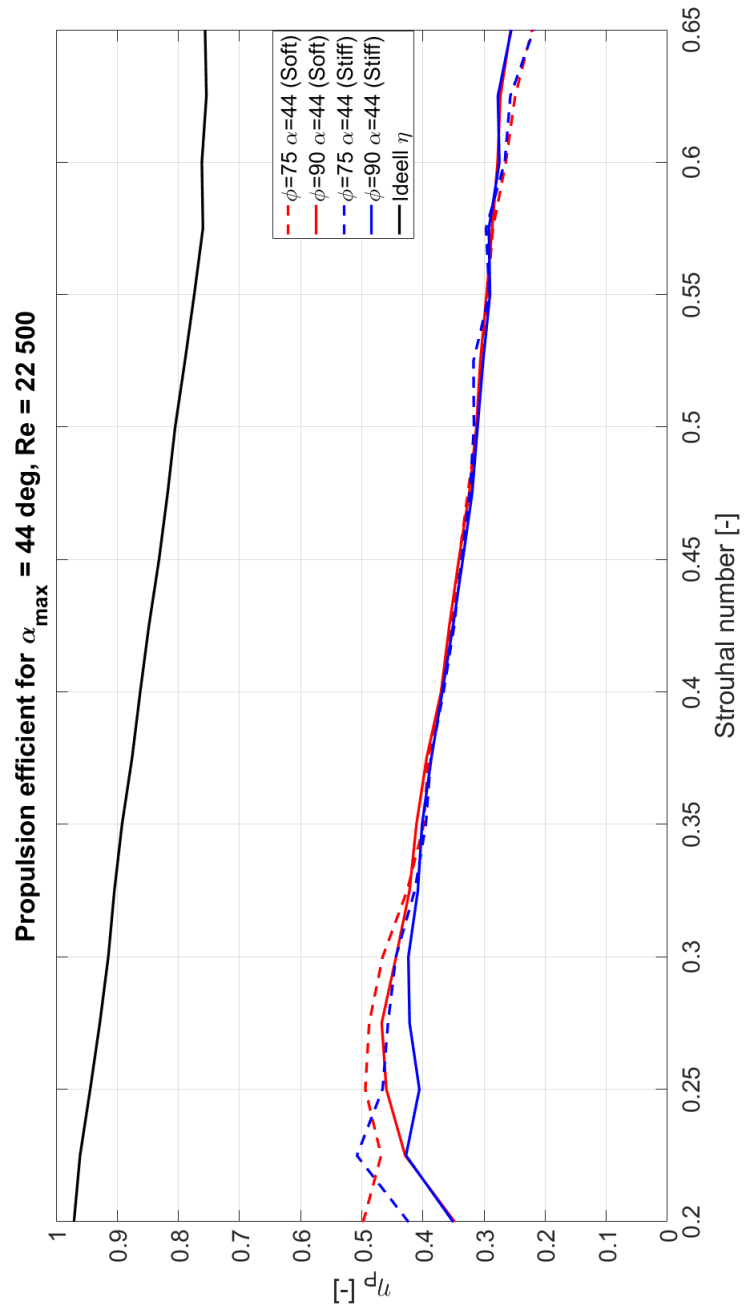
A.6 η_p

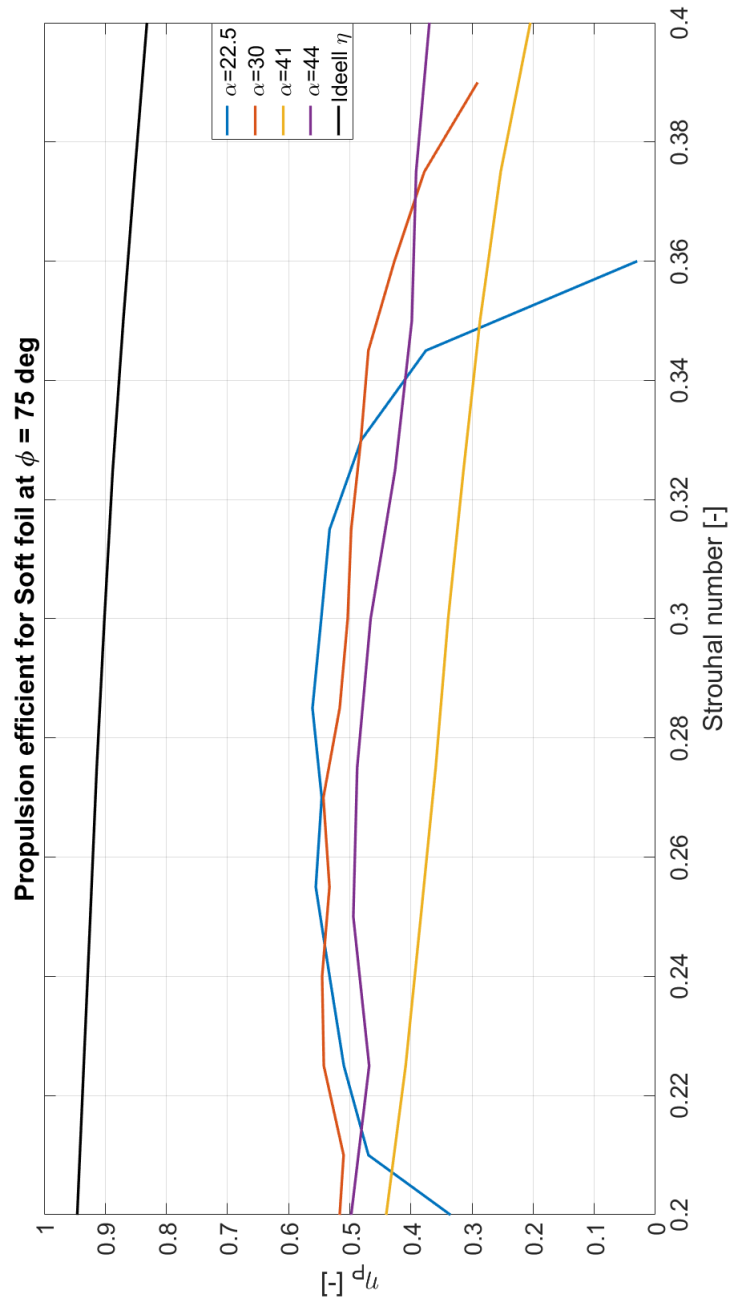




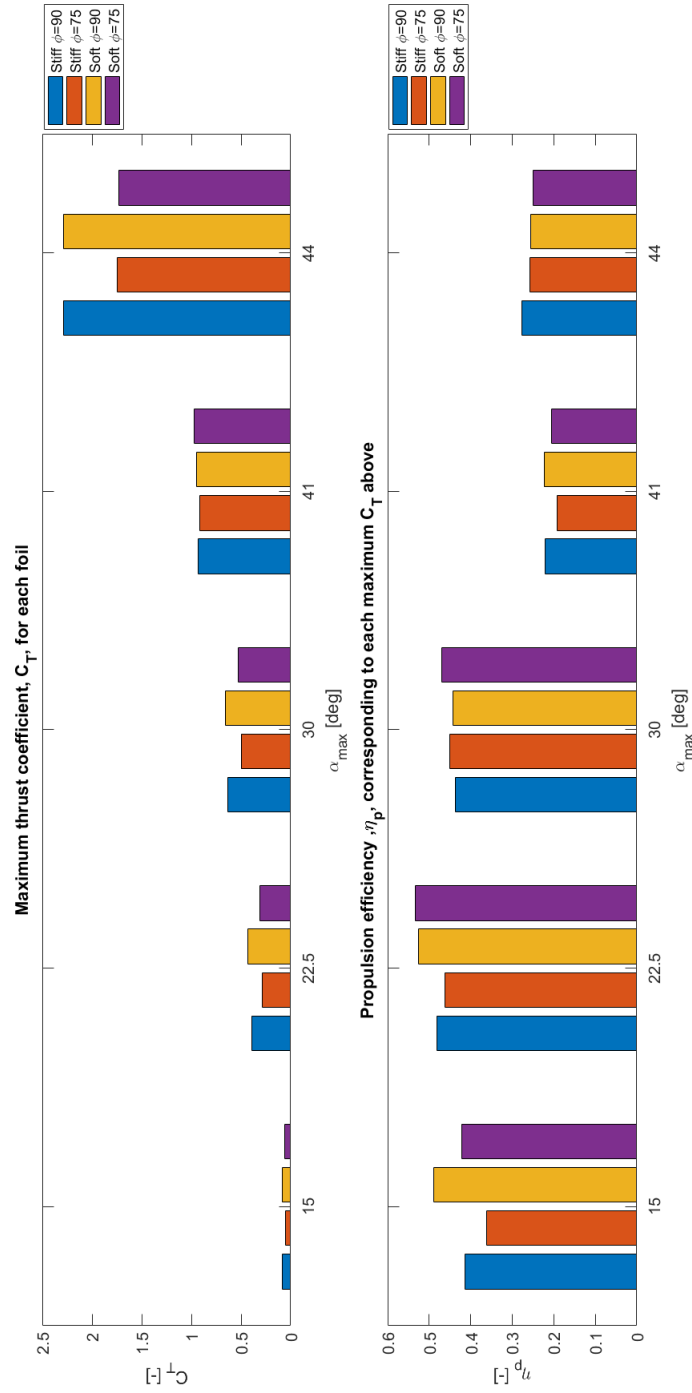


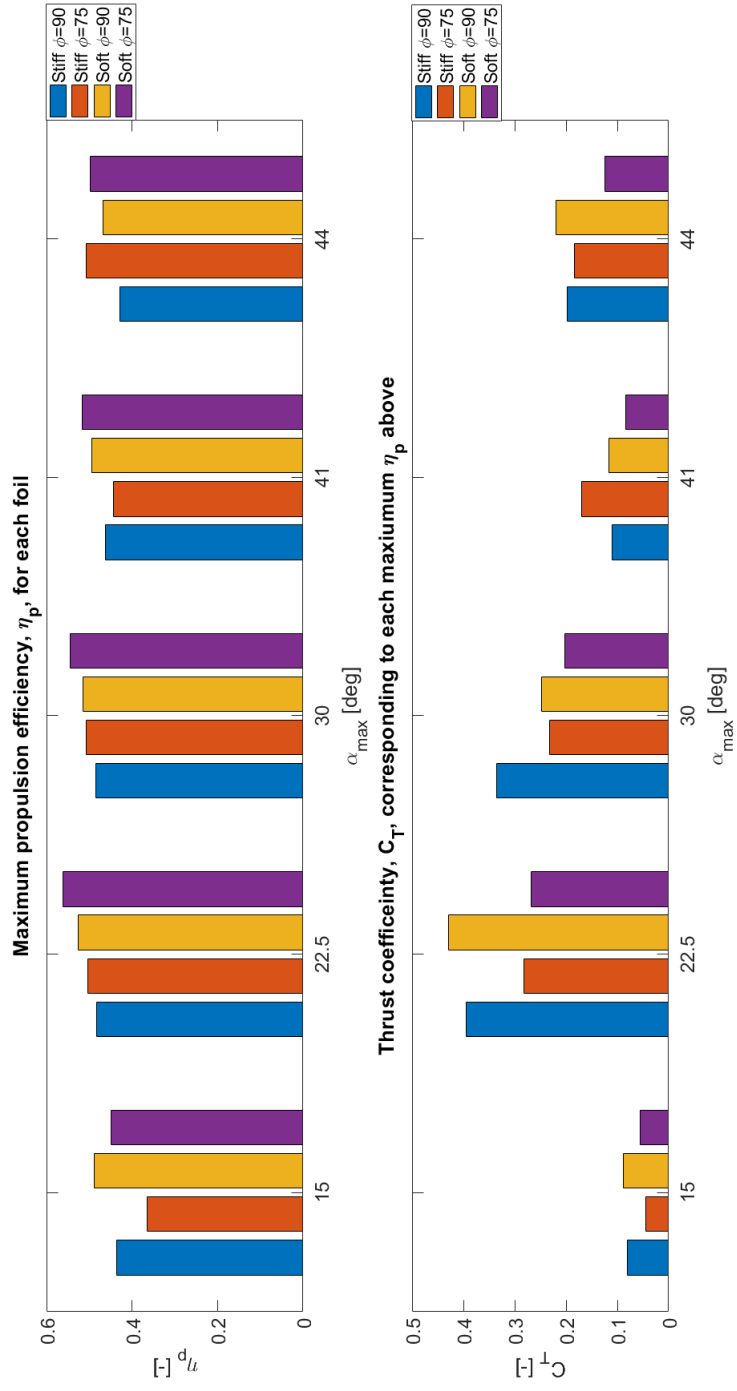






A.7 Bar plot with maximum C_T and maximum η_p





B Stratasys and printing

Material	Yield stress [σ_Y]	Young's Modulus [E]	Elongation at Break % of model length	Transition temperature [T_g]
Vero Blue	50-60 MPa	2.0-3.0 GPa	15-25%	48-50 °C
ABS Plus	55-60 MPa	2.6-3.0 GPa	25-40%	47-53 °C
RGD 525	70-80 MPa	3.1-3.5 GPa	10-15%	62-65 °C
Vero Gray	50-65 MPa	2.0-3.0 GPa	10-25%	52-54 °C

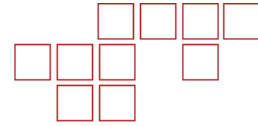
Table 8: Material properties of the plastic material of interest for printing of the soft foil by use of PolyJet 3D-printer. Information from Stratasys's Material Library [34]. Complete tables are found in Figure B.1

VERO PUREWHITE, VEROBLOCKPLUS, VEROCYAN, VEROGRAY, VEROMAGENTA, VEROMAGENTAV, VEROWHITEPLUS, VEROYELLOW, VEROYELLOWV			
	ASTM	ENGLISH	METRIC
Tensile strength	D-638-03	7,250-9,450 psi	50-65 MPa
Elongation at break	D-638-05	10-25%	10-25%
Modulus of elasticity	D-638-04	290,000-435,000 psi	2,000-3,000 MPa
Flexural Strength	D-790-03	11,000-16,000 psi	75-110 MPa
Flexural Modulus	D-790-04	320,000-465,000 psi	2,200-3,200 MPa
HDT, °C @ 0.45MPa	D-648-06	113-122 °F	45-50 °C
HDT, °C @ 1.82MPa	D-648-07	113-122 °F	45-50 °C
Izod Notched Impact	D-256-06	0.375-0.562 ft-lb/inch	20-30 J/m
Water Absorption	D-570-98 24hr	1.1-1.5%	1.1-1.5%
Tg	DMA, E»	126-129 °F	52-54 °C
Shore Hardness (D)	Scale D	83-86 (Scale D)	83-86 (Scale D)
Rockwell Hardness	Scale D	73-76 (Scale M)	73-76 (Scale M)
Polymerized density	Scale M		1.17-1.18 g/cm ³
Ash content (VeroGray, VeroWhitePlus)	USP281	0.23-0.26 %	0.23-0.26%
Ash content (VeroBlackPlus)	USP281	0.01-0.02 %	0.01-0.02%

Figure B.1: Material properties for Vero Gray. This is the standard material used by SINTEF Ocean for 3D printing. Data from Stratasys material library [34]

C FASTCAM MH4 camera

FASTCAM MH4



Specifications

FRAME RATE (fps)	MAX RESOLUTION (pixels)	EXPOSURE TIME	RECORD DURATION (seconds) 1GB / 2GB memory	RECORD DURATION (frames) 1GB / 2GB memory
250	512×512	1/frame rate to 6µs	16.0 / 32.0	4,092 / 8,184
500	512×512		8.0 / 16.0	4,092 / 8,184
1,000	512×512		4.0 / 8.0	4,092 / 8,184
2,000	512×512		2.0 / 4.0	4,092 / 8,184
3,000	512×352		1.9 / 3.8	5,693 / 11,386
4,000	512×256		2.0 / 4.0	8,184 / 16,368
8,000	512×128		2.0 / 4.0	16,368 / 32,736
10,000	512×96		2.2 / 4.4	21,824 / 43,648

Sensor	CMOS (Bayer system color, single sensor) with 10µm pixel, global electronic shutter and over-exposure protection	Video Output	NTSC or PAL. Live video during recording. Ability to zoom, pan and scroll within image via keypad
Shutter	Global electronic shutter from 20ms to 6µs	Recording Modes	Start, End, Center, Manual, Random
Saved Image Formats	JPEG, AVI, TIFF, BMP, RAW, RAWW, PNG, and FTIF	Camera Control	Through PFV software via Gigabit Ethernet and RS422 keypad with built in LCD monitor
Phase Lock	Enables cameras to be synchronized precisely together to a master camera or external source	Shock	100G @ 10ms 6 axis
Triggering	Selectable positive or negative TTL 5Vp-p, switch closure	Dimensions and Weight	Processor: 150mm (5.91")H x 245mm (9.65")W x 180mm (7.09")D *excluding protrusions Weight: 16.75 lbs (7.6kg) Camera Head: 35mm (1.38")H x 35mm (1.38") W x 34mm (1.34")D *excluding protrusions Weight: 0.66 lbs (0.3 kg)
Lens Mount	NF-mount, C-mount (Optional)	Power Requirements	100V - 240V AC , 65VA, 50-60Hz optional DC operation 22-32 VDC
Data Display	Frame Rate, Shutter Speed, Trigger Mode, Date or Time (can be switched), Status (Playback/Record), Real Time, Frame Count and Resolution		
Video Formats	NTSC, PAL RS170 video output		

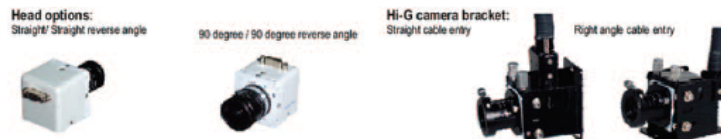


Figure C.1: Information about the Photron FASTCAM MH4 obtained from Luca Savio and from the home page of Photron [28]

On-board, Multi-head High-Speed Video System developed specifically for Automotive Safety Testing

The world's smallest camera head design providing high frame rates and excellent light sensitivity

Photron introduces the FASTCAM MH4 with four tiny cameras, each less than one and a half inches (35mm) cubed, providing incredibly light sensitive performance up to two thousand full resolution fps (frames per second). The cameras are connected to a compact processor unit, complete with battery backup for thirty minutes data retention in the event of power loss, via light-weight, flexible cables, and are available with either one or two Gigabyte onboard memory configurations dependent on your event duration.

The FASTCAM MH4 is engineered referring to SAE-J211 for operation under the most testing of environments and can operate under shock forces as massive as 100G's in any axis. The sub-compact camera heads are available with high-G lens mounts but are still lightweight enough to fit in just about any onboard location without requiring serious reinforcements. Camera heads are available in two different configurations (top cable or rear cable), and camera cable connectors are available in three different arrangements, so that cameras can be mounted in just about any configuration or orientation, ensuring you get good looking results every time.

An additional high-G battery pack is available for tests where supplying external power through costly and potentially weak umbilical cables is undesirable, or where the security of an uninterrupted power supply unit (UPS) is advantageous.

Benefits

- Small and lightweight camera head 35mm x 35mm x 34mm, weight 90g per head (excluding lens)
- Supports from one to four camera heads per processor
- High-G; 100G for 10ms in any axis
- 512 x 512 pixel resolution up to 2,000 fps
Reduced resolution up to 10,000 fps
- Gigabit Ethernet (1000BASE-T) interface
- Optional remote keypad with integrated 5" LCD video monitor for simple control of all functions and rapid switching between camera heads
- Optional Hi G battery pack for operation where external power is unavailable



Photron

www.photron.com

Figure C.2: Information about the Photron FASTCAM MH4 obtained from Luca Savio and from the home page of Photron [28]

D MATLAB

D.1 Post processing of data

```
1 clc
2 clear
3 close all
4
5 flagPlotLive           = 1;
6 flagDrag               = 1;
7     flagPSD_Drag       = 0;
8     flagDrag_filt      = 0;
9     flagDrag_int_filt  = 0;
10
11 flagMz_and_Lift        = 1;
12     flagPSD_Mz         = 0;
13     flagMz_filt        = 0;
14     flagMz_int_filt    = 0;
15
16     flagPSD_Lift        = 0;
17     flagLift_filt       = 0;
18     flagLift_int_filt  = 0;
19
20 flagCR                 = 1; %Need both Drag and Lift flag!
21 flagFeathering         = 0;
22 flagPower              = 0; %Need both Drag and Lift flag!
23 flagMz_Drag            = 0;
24 flagMotion             = 0;
25
26 flagWriteToFile        = 0;
27
28 %% Calling on file
29 % Husk     bytte hastighet U = 0.3 eller U = 0.15 eller U = 0.25!!
30 file1      = '4712.bin';
31 freq       = 0.475;
32 U          = 0.25;      % Inflow velocity [m/s]
```

```

33 offset          =      1; % = 1 to find the offset in the ...
    beginning of the time series, and adjust the value.
34 filt_freqMz     = freq*0.2;
35 filt_freqDrag   = (freq*2) + 0.2;
36 filt_freqLift   = filt_freqMz;
37 [a1, a2] = catman_read_5r8(file1);
38 %% Raw data
39 time = a2(1).data;
40 % Divided by -1000 to go from [mm] to [m], and to change sign
41 sway = (a2(6).data)*(-1/1000);
42 % Change from [deg] to [rad], and change sign.
43 yaw = (a2(7).data)*(-pi/180);
44 % Need to remove the offset in the data
45 Fx = (a2(14).data);
46 Fy = (a2(15).data);
47 Mz = a2(18).data;
48 FL = (a2(19).data) ; % Lift force
49 Fd = (a2(20).data) ; % Drag force
50 dt = time(2)-time(1);
51 if offset
52     time_offset = 10; % First 10 seconds used to find offset
53     number_of_points_offset = time_offset/dt;
54     Fl_with_offset = FL; % Lift force
55     Fd_with_offset = Fd; % Drag force
56     Fd_offset_interval = Fd_with_offset(1:number_of_points_offset);
57     Fl_offset_interval = Fl_with_offset(1:number_of_points_offset);
58     Fd_offset = mean(Fd_offset_interval);
59     Fl_offset = mean(Fl_offset_interval);
60     % Subtracting 0.07 from the Drag. When U is not zero at start
61     % This is the friction drag.
62     % When start at U=0, 0.07 subtraction from the lift, due to ...
        extra lift
63     % in the time series when the water starts flow around the foil.
64     Fd = Fd_with_offset + abs(Fd_offset) - 0.1 ;
65     FL = Fl_with_offset - Fl_offset;% - 0.35;
66 end
67
68 fs      = 200; % Sampling frequency [Hz]
69 rho     = 1000; % Density [kg/m^3]

```

```

70 c      = 0.15;      % Cord lenght [m]
71 s      = 0.4;      % Span lenght [m]
72
73 St = 2*0.075*freq/U;
74 % plot(time, sway, time, yaw)
75 % legend('sway','yaw')
76 % grid on
77 %% Finding the interval to use in the calculations
78 T = 1/freq;          % Period of one oscillation of the foil [T ...
    = s]
79 % dt = time(2)-time(1);      %
80 periods = 18;           % Number of periods to use
81 periods_live = 1;
82 number_of_index = (1/(freq*dt)+5)*periods; % Number of index to use
83 number_live = (1/(freq*dt))*periods_live; % Number of index to use
84 move = 67;
85 % Find first min.Start of the period for file1
86 for i = 1:length(sway)
87     if sway(i) < -0.074
88         I = i;
89         I_live = I+number_live+move;
90         break;
91     end
92 end
93 Time_first_period_starts = dt*I;
94 interval = (I:round(I+number_of_index)); % Create interval ...
    to use
95 live = (round(I_live):round(I_live+number_live+2));
96
97 %% Sort out the data from the interval of interest
98 time_interval = time(interval);
99 time_live = time(live);
100 sway_interval = sway(interval);
101 sway_live = sway(live);
102 yaw_interval = yaw(interval);
103 yaw_live = yaw(live);
104 Fx_interval = Fx(interval);
105 Fy_interval = Fy(interval);
106 Mz_interval = Mz(interval);

```

```

107 Lift_interval = FL(interval);
108 Drag_interval = Fd(interval);
109
110 %% Drag section
111 if flagDrag
112     %% PSD of Drag force BEFORE FILTERING
113     freq_Drag = 0:fs/length(Fd):fs/2; %Frequency axis
114     fft_Drag = fft(Fd); %Fast fourier transform ...
        of the time series
115     fft_Drag = fft_Drag(1:length(Fd)/2+1); %Only including ...
        values up to the Nyquist frequency
116     psd_Drag = (1/(length(Fd)*fs))*abs(fft_Drag).^2; %Calculating ...
        the PSD
117     psd_Drag(2:end-1) = 2*psd_Drag(2:end-1); %Making it ...
        one-sided. Zero'th and Nyquist element
118                                     %not doubled as ...
                                     they occur only ...
                                     once
119
120 %% Design Filter
121 %
122 D = ...
        designfilt('lowpassfir', 'FilterOrder', 4, 'PassbandFrequency', ...
        filt_freq_Drag, 'PassbandRipple', 0.4, ...
        'SampleRate', 200);
123 % Apply filter
124 Fd_filt = filtfilt(D, Fd);
125 %% PSD of the Drag force AFTER FILTERING
126 % Follows the same procedure as for the raw data
127 fft_Drag_filt = fft(Fd_filt);
128 fft_Drag_filt = fft_Drag_filt(1:length(Fd)/2+1);
129 psd_Drag_filt = (1/(length(Fd)*fs))*abs(fft_Drag_filt).^2;
130 psd_Drag_filt(2:end-1) = 2*psd_Drag_filt(2:end-1);
131
132 FD_interval_filt = Fd_filt(interval);
133
134 %% Plotting Drag
135 if flagPSD_Drag
136     figure;
137     plot(freq_Drag(1:130), psd_Drag(1:130)) %No filter

```

```

138     hold on
139     plot(freq_Drag(1:130), psd_Drag_filt(1:130))    %After filter
140     hold off
141     title('PSD of the Drag')
142     xlabel('frequency [Hz]')
143     ylabel('Power Spectral Density [m^2/Hz]')
144     legend('Unfiltered', 'Filtered')
145 end
146 if flagDrag_filt
147     figure;
148     plot(time,Fd)    %No filter
149     hold on
150     plot(time,Fd_filt)    %After filter
151     hold off
152     title('Drag force before and after filtering')%title(file)
153     xlabel('Time [s]')
154     ylabel('Drag Force [N]')
155     legend('Unfiltered', 'Filtered')
156 end
157 if flagDrag_int_filt
158     figure;
159     plot(time_interval,Drag_interval)    %No filter
160     hold on
161     plot(time_interval,FD_interval_filt)    %After filter
162     hold off
163     title('Drag Force for a given interval before and ...
164           after filtering')%title(file)
165     xlabel('Time [s]')
166     ylabel('Drag [N]')
167     legend('Unfiltered', 'Filtered')
168 end
169 %% Finding Fd (Thrust) and C_T
170 % Using trapz-method to integrate the force over x ...
171 % intervals. For the
172 % filtered and unfiltered data
173 Fd_integrated_filt = ...
174     trapz(time_interval,FD_interval_filt)/(periods*T);
175 Fd_integrated = ...
176     trapz(time_interval,Drag_interval)/(periods*T);

```

```

173     % Coefficient for Lift and Drag
174     % CT = Fd.integrated_filt/(rho*0.5*c*s*U^2);
175     % CT with the frictional drag included.
176     % Value from C_DF = 2 C_f (1 + 2 t/c + 60 (t/c)^4 )
177     CT = Fd.integrated_filt/(rho*0.5*c*s*U^2);
178     % Live for the Thrust and CT
179     Thrust_live_interval = Fd_filt(live);
180     CT_live              = ...
        Thrust_live_interval./(rho*0.5*c*s*U^2);
181
182
183 end % FlagDrag
184
185 %% Mz and Lift section
186 if flagMz_and_Lift
187     %% PSD of Mz and Lift BEFORE FILTERING
188     freq_Mz = 0:fs/length(Mz):fs/2;
189     fft_Mz = fft(Mz);
190     fft_Mz = fft_Mz(1:length(Mz)/2+1);
191     psd_Mz = (1/(length(Mz)*fs))*abs(fft_Mz).^2;
192     psd_Mz(2:end-1) = 2*psd_Mz(2:end-1);
193
194     freq_Lift = 0:fs/length(FL):fs/2;
195     fft_Lift = fft(FL);
196     fft_Lift = fft_Lift(1:length(FL)/2+1);
197     psd_Lift = (1/(length(FL)*fs))*abs(fft_Lift).^2;
198     psd_Lift(2:end-1) = 2*psd_Lift(2:end-1);
199     %% Design Filter
200     %
201     D_Mz = ...
        designfilt('lowpassiir','FilterOrder',4,'PassbandFrequency', ...
        filt_freq_Mz,'PassbandRipple', 0.2, ...
202         'SampleRate', 200);
203     D_Lift = ...
        designfilt('lowpassiir','FilterOrder',4,'PassbandFrequency', ...
        filt_freq_Lift,'PassbandRipple', 0.2, ...
204         'SampleRate', 200);
205 % xint=interp1(time,x,t); %Interpolate data
206 % xclean=clean_data(xint,3,0.001); %Clean data

```



```

207 %     cutoff=[0.3 0.8]; %Cut-off frequencies
208 % %     fnyq=1/(2*dt); %Nyquist frequency
209 %     [b,a]=butter(16,cutoff,'bandpass'); %Get filter coefficients
210 %     FL_filt      = filtfilt(b,a,FL);
211 %     D_Lift = ...
designfilt('bandpassfir','FilterOrder',24,'CutoffFrequency1', ...
0.2 , 'CutoffFrequency2', 0.6, 'SampleRate', 200);
212 % Apply filter
213 Mz_filt      = filtfilt(D_Mz,Mz);
214 FL_filt      = filtfilt(D_Lift,FL);
215 sway_filt    = filtfilt(D_Lift,sway);
216 yaw_filt     = filtfilt(D_Mz,yaw);
217 %% PSD of the Mz and Lift AFTER FILTERING
218 % Follows the same procedure as for the raw data
219 fft_Mz_filt = fft(Mz_filt);
220 fft_Mz_filt = fft_Mz_filt(1:length(Mz)/2+1);
221 psd_Mz_filt = (1/(length(Mz)*fs))*abs(fft_Mz_filt).^2;
222 psd_Mz_filt(2:end-1) = 2*psd_Mz_filt(2:end-1);
223
224 fft_Lift_filt = fft(FL_filt);
225 fft_Lift_filt = fft_Lift_filt(1:length(FL)/2+1);
226 psd_Lift_filt = (1/(length(FL)*fs))*abs(fft_Lift_filt).^2;
227 psd_Lift_filt(2:end-1) = 2*psd_Lift_filt(2:end-1);
228
229 Mz_interval_filt = Mz_filt(interval);
230 FL_interval_filt = FL_filt(interval);
231 %% Calculating the sway and yaw velocity
232 % Combining the velocities with the Lift and moment around ...
z-axis.
233 % Using finite difference method to find the sway velocity.
234 % Second-order accuracy, first-order derivative
235 L_sway = length(sway);
236 for i = 1:L_sway
237     % Sway velocity
238     if i == 1 % Forward finite difference
239         sway_velocity(i) = ...
((-1.5*sway_filt(i)+2*sway_filt(i+1)-0.5*sway_filt(i+2))/dt);
240     elseif i == L_sway % Backward finite difference

```

```

241         sway_velocity(i) = ...
                ((0.5*sway_filt(i-2)-2*sway_filt(i-1)+1.5*sway_filt(i))/dt);
242     else                                     % Central finite difference
243         sway_velocity(i) = ...
                ((0.5*sway_filt(i+1)-0.5*sway_filt(i-1))/dt);
244     end
245     % Yaw velocity
246     if i == 1                               % Forward finite difference
247         yaw_velocity(i) = ...
                ((-1.5*yaw_filt(i)+2*yaw_filt(i+1)-0.5*yaw_filt(i+2))/dt);
248     elseif i == L_sway % Backward finite difference
249         yaw_velocity(i) = ...
                ((0.5*yaw_filt(i-2)-2*yaw_filt(i-1)+1.5*yaw_filt(i))/dt);
250     else                                     % Central finite difference
251         yaw_velocity(i) = ...
                ((0.5*yaw_filt(i+1)-0.5*yaw_filt(i-1))/dt);
252     end
253     end
254     % sway_velocity = diff(sway_filt);
255     % yaw_velocity = diff(yaw_filt);
256     % Sway velocity [m/s].
257     sway_velocity_interval = sway_velocity(interval);
258     yaw_velocity_interval = yaw_velocity(interval);
259     %% Finding FL, Mz, P (Power) and CP (Power coefficient)
260     % Lift force and sway velocity, integrated over x periods
261     % Filtered data
262     % Lift force integrated
263     FL_integrated_filt = ...
                trapz(time_interval,FL_interval_filt)/(periods*T);
264     % Lift and sway velocity
265     Lift_and_sway_filt = FL_filt.*sway_velocity;
266     Lift_and_sway_interval = ...
                FL_interval_filt.*sway_velocity_interval;
267     Lift_live_filt = FL_filt(live);
268     CL_live = Lift_live_filt/(rho*0.5*c*s*U^2);
269     % Lift_and_sway_interval = Lift_and_sway_filt(interval);
270     Lift_Sway_integrated = ...
                trapz(time_interval,Lift_and_sway_interval);
271     % Mz and yaw velocity

```

```

272     Mz_and_yaw_filt = Mz_filt.*yaw_velocity;
273     Mz_and_yaw_interval = ...
           Mz_interval_filt.*yaw_velocity_interval;
274     Mz_live_filt = Mz_filt(live);
275     CM_live = Mz_live_filt/(rho*0.5*c*s*U^3);
276 %     Mz_and_yaw_interval = Mz_and_yaw_filt(interval);
277     Mz_Yaw_integrated = trapz(time_interval,Mz_and_yaw_interval);
278     P_integrated = -(Lift_Sway_integrated + ...
           Mz_Yaw_integrated)/(T*periods);
279     CP = P_integrated/(rho*0.5*c*s*U^3)
280     CT = CT
281     eta_prop = CT/CP
282 % Live plot of Power and CP
283     P_filt = Lift_and_sway_filt + Mz_and_yaw_filt;
284     P_live = P_filt(live);
285     CP_live = P_live./(rho*0.5*c*s*U^3);
286
287 if flagPlotLive
288     zero = zeros(1,length(live));
289     textsize = 18;
290     figure;
291     set(plot(time_live,CP_live,time_live,CT_live,time_live,yaw_live,time_li
292     title('C_P and C_T during one oscillation')
293     xlabel('Time [s]')
294     ylabel('')
295     legend('CP [-]','CT [-]', '\theta_{yaw} ...
           [rad]','y_{sway} [dm]')
296     grid on
297     set(gca,'fontsize',textsize)
298
299     figure
300     ax1 = subplot(2,1,1);
301     set(plot(time_live,CT_live,'b',time_live,CP_live,'r',time_live,zero,'bl
302     title('C_P and C_T during one oscillation')
303     xlabel('Time [s]')
304     ylabel('[-]')
305     legend('C_T','C_P')
306     grid on
307     set(gca,'fontsize',textsize)

```

```

308
309     ax2 = subplot(2,1,2);
310     set(plot(time_live,yaw_live,'b',time_live,sway_live*10,'r',time_live,z
311     title('\theta_{yaw} and y_{sway} at the same time')
312     xlabel('Time [s]')
313     ylabel('')
314     legend('\theta_{yaw} [rad]','y_{sway} [dm]')
315     grid on
316     set(gca,'fontsize',textsize)
317 % ...
318
319     figure
320     ax3 = subplot(2,1,1);
321     set(plot(time_live,CT_live,'b',time_live,CM_live*10,'r',time_live,CL_li
322     title('C.M, C.L and C.T during one oscillation')
323     xlabel('Time [s]')
324     ylabel('[-]')
325     legend('C.T','C.M *10','C.L')
326     grid on
327     set(gca,'fontsize',textsize)
328
329     ax4 = subplot(2,1,2);
330     set(plot(time_live,yaw_live,'b',time_live,sway_live*10,'red',time_live,
331     title('\theta_{yaw} and y_{sway} at the same time')
332     xlabel('Time [s]')
333     ylabel('')
334     legend('\theta_{yaw} [rad]','y_{sway} [dm]')
335     grid on
336     set(gca,'fontsize',textsize)
337 end
338
339
340 %% Plotting Power during time serie
341 if flagPower
342     figure;
343
344     plot(time_interval,P_live_interval/10000) % Power
345     hold on

```

```

346         plot(time_interval,FD_interval_filt)      % Drag force
347         hold on
348         plot(time_interval, Mz_interval_filt)     % Mz
349         hold off
350         title(file1)
351         xlabel('Time [s]')
352         ylabel('')
353         legend('Power P [10*kW]', 'Drag force [N]', 'Mz [Nm] ')
354         grid on
355         set(gca, 'fontsize', textsize)
356     end
357
358
359     %% Plotting Mz
360     if flagPSD_Mz
361         textsize = 17;
362         figure;
363         plot(freq_Mz(1:130), psd_Mz(1:130))        %No filter
364         hold on
365         plot(freq_Mz(1:130), psd_Mz_filt(1:130))  %After filter
366         hold off
367         title('PSD of Mz')
368         xlabel('Frequenzy [Hz]')
369         ylabel('Power Spectral Density')
370         legend('Unfiltered', 'Filtered')
371         set(gca, 'FontSize', textsize)
372     end
373     if flagMz_filt
374         figure;
375         plot(time, Mz)                             %No filter
376         hold on
377         plot(time, Mz_filt)                        %After filter
378         hold off
379         title('Mz before and after filtering')%title(file)
380         xlabel('Time [s]')
381         ylabel('Moment around z-axis [Nm]')
382         legend('Unfiltered', 'Filtered')
383     end
384     if flagMz_int_filt

```

```

385     figure;
386     plot(time_interval,Mz_interval)      %No filter
387     hold on
388     plot(time_interval,Mz_interval_filt) %After filter
389     hold off
390     title('Mz for a given interval before and after ...
           filtering')%title(file)
391     xlabel('Time [s]')
392     ylabel('Mz [Nm]')
393     legend('Unfiltered', 'Filtered')
394 end
395 % Plotting Lift
396 if flagPSD.Lift
397     figure;
398     plot(freq_Lift(1:130),psd_Lift(1:130)) %No filter
399     hold on
400     plot(freq_Lift(1:130), psd_Lift_filt(1:130)) %After ...
           filter
401     hold off
402     title('PSD of the Lift Force')
403     xlabel('Frequenzy [Hz]')
404     ylabel('Power Spectral Density')
405     legend('Unfiltered', 'Filtered')
406 end
407 if flagLift_filt
408     figure;
409     plot(time,FL) %No filter
410     hold on
411     plot(time,FL_filt) %After filter
412     hold off
413     title('Lift force before and after ...
           filtering')%title(file)
414     xlabel('Time [s]')
415     ylabel('Lift[N]')
416     legend('Unfiltered', 'Filtered')
417 end
418 if flagLift_int_filt
419     figure
420     plot(time_interval,Lift_interval,time_interval,FL_interval_filt)

```

```

421         title('Lift force in the given interval before and ...
              after filtering')%title(file)
422         xlabel('Time [s]')
423         ylabel('Lift[N]')
424         legend('Unfiltered', 'Filtered')
425     end
426
427
428 end %flagMz_and_Lift
429
430 if flagCR
431     %% Finding Resultant Force coefficient
432     CR = (sqrt(Fd.integrated_filt.^2. + ...
              FL.integrated_filt.^2))/(0.5*c*s*rho*U^2);
433     CR_interval = CR(interval);
434     %% CR_max = max(CR_interval);
435     CR_mean = mean(CR_interval);
436     CR_plot = sqrt(FD.interval_filt.^2 + ...
              FL.interval_filt.^2)/(0.5*c*s*rho*U^2);
437     plot(time_interval,CR_plot)
438
439     figure
440     plot(time_interval,CR_interval*10,time_interval,FL.interval_filt,time_interval,
441          xlabel('Time [s]')
442          ylabel('')
443          legend('Resultant force coeff C.R*10 [-]','Lift force F.L ...
              [N]','Drag force D.L [N]')
444          title(file1)
445 end
446 %% Plotting motion of the foil
447 if flagMotion
448     textsize = 17;
449     figure
450     plot(time_interval,sway_interval,time_interval,sway_velocity_interval)
451     xlabel('Time [s]')
452     ylabel('Sway motion')
453     legend('Sway y- $\{pos\}$  [mm]','Sway velocity d/dt(y- $\{sway\}$ ) [mm/s]')
454     title('Sway motion of the foil from the interval chosen')
455

```

```

456     figure
457     plot(time_interval,yaw_interval,time_interval,yaw_velocity_interval)
458     xlabel('Time [s]')
459     ylabel('Yaw motion')
460     legend('Yaw \theta_{yaw} [mm]', 'Yaw velocity ...
         d/dt(\theta_{yaw}) [mm/s]')
461     title('Yaw motion of the foil from the interval chosen')
462
463     figure
464     plot(time,yaw,time,sway,time,Fx)
465     xlabel('Time [s]')
466     ylabel('')
467     legend('\theta_{yaw} [degrees]', 'y_{sway} [mm]', 'Fx')
468     title('Motion of the stiff foil at 0.95 Hz')
469     grid on
470     set(gca, 'FontSize',textsize)
471 end
472 %% Compare results Luca
473 if flagMz_Drag
474     figure;
475     plot(time_interval,Mz_interval)
476     hold on
477     plot(time_interval,sway_interval/100)
478     hold on
479     plot(time_interval,FD_interval_filt)    %After filter
480     hold off
481     title(file1)%title(file)
482     xlabel('Time [s]')
483     ylabel('')
484     legend('Mz [Nm*10]', 'Sway [m]', 'Drag force [N] ')
485 end
486 %%
487 if flagWriteToFile
488     % Write to txt-file. 'a' = append (legge til). Create new line ...
         with \n
489     % and write data on new line. Do not overwrite old data in the ...
         same document
490

```



```

491     fid = ...
         fopen('alpha15.0_soft_phase75_deg26_U0.35_5800_husk-aa-bytte-navn.txt','a');
492     formatSpec = '%6.4f %6.4f %6.4f %6.4f %6.4f %6.4f %6.4f \n';
493     fprintf(fid,formatSpec,freq,P.integrated,CP,Fd.integrated_filt,CT,eta_prop,CR);
494
495 end

```

D.2 Calculate shear centre and plot

```

1  % Finding shear center in cross section of foil with skott in span
2  % direction.
3  clear all
4
5  %Define the gemoetry of the foil cross section. All values are in ...
    mm. Skott
6  %C is a triangle with length lc and heigth hc. Skott D is the ...
    lower and
7  %upper part of the foil. Skott D is assumed two rectagles placed ...
    a distance
8  % 5.6 mm from center line of the foil (Origin)
9  ha = 16.55;      %Heigth of skott A
10 hb = 11;        %Heigth of skott B
11 hc = 7.86;      %Heigth of skott C
12 ta = (3:3:21);  %Thickness skott A
13 tb = ta;        %Thickness skott B
14 td = 3.4;       %Thickness skott D
15 lc = 30;        %Length skott C
16 ld = 112;       %Length skott D
17
18 V = 1;          %Applied shear force, lift of the foil [N]. Does ...
    not effect
19 %the result of shear center.
20
21 %Origin is defined at leading edge. The respective distances from ...
    origin

```

```

22 %to the skotts are da, db, dc and dd. This is the distance to the ...
    center
23 %of area of the skott.
24 da = (20:10:60);      %Distance from origin to skott A
25 db = 80;             %Distance from origin to skott B
26 dc = 130;           %Distance from origin to skott C
27 dd = 5.6;           %Distance from origin to skott D
28
29 for i = 1:length(ta)
30     for j = 1:length(da)
31 %Finding the second moment of inertia for the cross section.
32     Ixx_a(i) = ha^3*ta(i)/12;          %Inertia for skott A
33     Ixx_b(i) = hb^3*tb(i)/12;          %Inertia for skott B
34     Ixx_c = hc^3*lc/48;                %Inertia for skott C
35     Ixx_d = td^3*ld/12 + td*ld*dd^2;   %Inertia for skott D
36     Ixx(i) = Ixx_a(i)+Ixx_b(i)+Ixx_c+Ixx_d; %Total inertia
37
38 %Area moment of the skott. The area times the distance from origin.
39     Qa(i) = ha*ta(i)*ha;               %Area moment for skott A
40     Qb(i) = hb*tb(i)*hb;               %Area moment for skott B
41     Qc = hc*lc*0.5*hc/6;               %Area moment for skott C
42     Qd = td*ld*dd;
43 %Calculat shear tension
44     tau_a(i) = (Qa(i)*V)/(Ixx(i)*ta(i)); %Shear tension in ...
        skott A
45     tau_b(i) = (Qb(i)*V)/(Ixx(i)*tb(i)); %Shear tension in ...
        skott B
46     tau_c(i) = (Qc*V)/(Ixx(i)*lc);      %Shear tension in ...
        skott C
47     tau_d(i) = (Qd*V)/(Ixx(i)*td);      %Shear tension in ...
        skott C
48 %Calculat shear Force in the skott
49     Fa(i) = (tau_a(i)*ha*ta(i))/2;      %Shear force in skott A
50     Fb(i) = (tau_b(i)*hb*tb(i))/2;      %Shear force in skott B
51     Fc(i) = (tau_c(i)*hc*lc*0.5)/2;     %Shear force in skott C
52     Fd(i) = (tau_d(i)*ld*td)*2/2;%Shear force in upper and lower ...
        part of foil
53

```

```

54 %Solving the moment shear center using the summation of moments ...
    from the
55 %shear forces
56 %Different thickness i
57     e_two_skott(i,j) = (Fa(i)*da(j) + Fb(i)*db + Fc(i)*dc)/V;
58     e_one_skott(i,j) = (Fa(i)*da(j) + Fc(i)*dc)/V;
59     e_zero_skott(i,j) = (Fc(i)*dc)/V;
60
61     end
62 end
63 %different distance from origin j
64     e_two_skott1 = e_two_skott(:,1);
65     e_two_skott2 = e_two_skott(:,2);
66     e_two_skott3 = e_two_skott(:,3);
67     e_two_skott4 = e_two_skott(:,4);
68     e_two_skott5 = e_two_skott(:,5);
69
70
71 %Plotting
72 fontsize = 15;
73 plot(ta,e_two_skott1,ta,e_two_skott2,ta,e_two_skott3,ta,e_two_skott4,ta,...
74     e_two_skott5)
75 xlabel('Thickness of skott [mm] ')
76 ylabel('Shear centre [mm]')
77 legend('distance=20mm','distance=30mm','distance=40mm','distance=50mm',...
78     'distance=60mm','distance=70mm','distance=80mm')
79 title('Shear centre for bulkhead design. In millimeter from ...
    leading edge')
80 set(gca,'fontsize', fontsize)

```

D.3 Plot C_p from *XFoil*

```
1 clear all
2 clc
3
4 fid = fopen('cp_1.txt');
5 textData = ...
    textscan(fid, '%n%n%n', 160, 'headerlines', 1, 'delimiter', ',');
6 fid5 = fopen('cp_3.txt');
7 textData5 = ...
    textscan(fid5, '%n%n%n', 160, 'headerlines', 4, 'delimiter', ',');
8 fid2 = fopen('cp_5.txt');
9 textData2 = ...
    textscan(fid2, '%n%n%n', 160, 'headerlines', 4, 'delimiter', ',');
10 fid3 = fopen('cp_7.txt');
11 textData3 = ...
    textscan(fid3, '%n%n%n', 160, 'headerlines', 4, 'delimiter', ',');
12 fid4 = fopen('cp_10.txt');
13 textData4 = ...
    textscan(fid4, '%n%n%n', 160, 'headerlines', 4, 'delimiter', ',');
14
15 %Importing data from txt-file. textscan is reading the file: ...
    (filename,
16 %3 collons with number, 160 lines, ignore headerlines, number of
17 %headerlines, delimiter = comma.
18 x      = textData(:,1);      %x-coordinate
19 y      = textData(:,2);      %y-coordinate
20 Cp     = textData(:,3);      %Pressure coefficient
21
22 x2     = textData2(:,1);     %x-coordinate
23 y2     = textData2(:,2);     %y-coordinate
24 Cp2    = textData2(:,3);     %Pressure coefficient
25
26 x3     = textData3(:,1);     %x-coordinate
27 y3     = textData3(:,2);     %y-coordinate
28 Cp3    = textData3(:,3);     %Pressure coefficient
29
```

```

30 x4      = textData4(:,1);      %x-coordinate
31 y4      = textData4(:,2);      %y-coordinate
32 Cp4     = textData4(:,3);      %Pressure coefficient
33
34 x5      = textData5(:,1);      %x-coordinate
35 y5      = textData5(:,2);      %y-coordinate
36 Cp5     = textData5(:,3);      %Pressure coefficient
37 fclose(fid);
38
39 %Using "cell2mat" to open the cell-array from the textfile
40 x_cell = cell2mat(x);
41 y_cell = cell2mat(y);
42 Cp_cell = cell2mat(Cp);
43 alfa1 = [x_cell,Cp_cell];
44
45 x_cell5 = cell2mat(x5);
46 Cp_cell5 = cell2mat(Cp5);
47 alfa3 = [x_cell5,Cp_cell5];
48
49 x_cell2 = cell2mat(x2);
50 Cp_cell2 = cell2mat(Cp2);
51 alfa5 = [x_cell2,Cp_cell2];
52
53 x_cell3 = cell2mat(x3);
54 Cp_cell3 = cell2mat(Cp3);
55 alfa7 = [x_cell3,Cp_cell3];
56
57 x_cell4 = cell2mat(x4);
58 Cp_cell4 = cell2mat(Cp4);
59 alfa10 = [x_cell4,Cp_cell4];
60
61
62
63 %Finding center of pressure
64 % A1 = polyarea(x_cell,Cp_cell)
65 % [x,y] = centroid(f1);
66 % [n,c] = ecdfhist(Cp_cell,x_cell,10) % returns the histogram ...
    bars using m bins
67

```

```

68 %Finding the location of minimum pressure
69 [M1,I1] = min(Cp_cell);
70 min_x1 = x_cell(I1);
71 [M2,I2] = min(Cp_cell2);
72 min_x2 = x_cell(I2);
73 [M3,I3] = min(Cp_cell3);
74 min_x3 = x_cell(I3);
75 [M4,I4] = min(Cp_cell4);
76 min_x4 = x_cell(I4);
77 [M5,I5] = min(Cp_cell5);
78 min_x5 = x_cell(I5);
79
80 % Finding the mean value of the pressure and the location of the mean
81 % pressure
82 % for i = 1:5
83
84
85 %Plot of the pressure coeff
86 fontsize = 10;
87
88 plot(alfa3,alfa5
89 % ...
    , x_cell5,Cp_cell5,x_cell2,Cp_cell2,x_cell3,Cp_cell3,x_cell4,Cp_cell4)
90 xlabel('x/c')
91 ylabel('Pressure coeff')
92 legend('Alfa=5')
93 % , 'Alfa=3', 'Alfa=5', 'Alfa=7', 'Alfa=10'
94 title('Pressure coeff for NACA0012')
95 set(gca, 'fontsize', fontsize)
96
97
98 median_Cp = median(alfa3)
99 mean_Cp = mean(alfa3)
100 mode_Cp = mode(alfa3)
101
102 x_median = find(mode_Cp)

```

